2017

Development of a digital microarray with interferometric reflectance imaging

BOSTON UNIVERSITY

COLLEGE OF ENGINEERING

Dissertation

DEVELOPMENT OF A DIGITAL MICROARRAY WITH INTERFEROMETRIC REFLECTANCE IMAGING

by

DERIN SEVENLER

B.S., Cornell University, 2011
M.S., Boston University, 2014

Submitted in partial fulfillment of the

requirements for the degree of

Doctor of Philosophy

2017

Approved by

First Reader

M. Selim Ünlü, Ph.D.
Professor of Electrical and Computer Engineering
Professor of Materials Science and Engineering
Professor of Biomedical Engineering

Second Reader

Irving J. Bigio, Ph.D.
Professor of Biomedical Engineering
Professor of Electrical and Computer Engineering
Professor of Physics
Professor of Medicine

Third Reader

Ahmad Khalil, Ph.D.
Assistant Professor of Biomedical Engineering

Fourth Reader

Charles P. DeLisi, Ph.D.
Dean Emeritus, College of Engineering
Metcalf Professor of Science and Engineering

Fifth Reader

Lei Tian, Ph.D.
Assistant Professor of Electrical and Computer Engineering

Myself when young did eagerly frequent
Doctor and Saint, and heard great argument
About it and about: but evermore
Came out by the same door as in I went.

With them the seed of Wisdom did I sow,
And with my own hand wrought to make it grow;
And this was all the Harvest that I reap'd—
"I came like Water, and like Wind I go."

Omar Khayyám (tr. Edward Fitzgerald)

Acknowledgments

First and foremost, I would like to thank Selim. He has shown me the importance of courage and boldness in research, and he has inspired all of my best work. I am grateful for his friendship.

I am indebted to Professors Bennett Goldberg, Mo Khalil, and Charles DeLisi for their mentorship and guidance over the past six years. Their advice has been golden. I am grateful also to Professors Irving Bigio and Lei Tian, whose feedback and insights have improved my work.

This work would have been impossible without my colleagues in the OCN Lab. I owe a deep debt to George Daaboul, who mentored me when I first joined the group. I am continually inspired by his ingenuity, enthusiasm and kindness. Abdulkadir, Ronen, Michael, Oguzhan and Jake have all been my teachers in optics. Likewise I am grateful to Margo, Sunmin, Xirui, Elif, Steve, and Fulya for all they have taught me about biology, biochemistry and experimental design. I also wish to thank David, who has been an invaluable resource for electronic circuit design and wafer processing.

Last but not least, I must thank my family—Korhan, Suzanne, Serra, and Margaret—whose unwavering love and support have meant the world.

DEVELOPMENT OF A DIGITAL MICROARRAY WITH INTERFEROMETRIC REFLECTANCE IMAGING

DERIN SEVENLER

Boston University, College of Engineering, 2017

Major Professor: M. Selim Ünlü, Ph.D.
Professor of Electrical and Computer Engineering,
Professor of Materials Science and Engineering,
Professor of Biomedical Engineering

ABSTRACT

This dissertation describes a new type of molecular assay for nucleic acids and proteins. We call this technique a digital microarray since it is conceptually similar to conventional fluorescence microarrays, yet it performs enumerative ('digital') counting of the number captured molecules. Digital microarrays are approximately 10,000-fold more sensitive than fluorescence microarrays, yet maintain all of the strengths of the platform including low cost and high multiplexing (i.e., many different tests on the same sample simultaneously). Digital microarrays use gold nanorods to label the captured target molecules. Each gold nanorod on the array is individually detected based on its light scattering, with an interferometric microscopy technique called SP-IRIS. Our optimized high-throughput version of SP-IRIS is able to scan a typical array of 500 spots in less than 10 minutes. Digital DNA microarrays may have utility in applications where sequencing is prohibitively expensive or slow. As an example, we describe a digital microarray assay for gene expression markers of bacterial drug resistance.

Contents

List of Tables

List of Figures

List of Abbreviations

AST	.....	Antibiotic susceptibility test
bp	.....	Base pair
ctDNA	.....	Circulating tumor DNA
DNA	.....	Deoxyribonucleic acid
dPCR	.....	Digital Polymerase Chain Reaction
E. coli	.....	*Escherichia coli*
GNR	.....	Gold nanorod
IRIS	.....	Interferometric Reflectance Imaging Sensor
LP	.....	Linear polarizer
mRNA	.....	messenger RNA
NGS	.....	Next generation sequencing
PBS	.....	Phosphate buffered saline
PCR	.....	Polymerase Chain Reaction
qPCR	.....	Quantitative Polymerase Chain Reaction
QWP	.....	Quarter wave plate
RNA	.....	Ribonucleic acid
SNP	.....	Single nucleotide polymorphism
SP-IRIS	.....	Single-Particle Interferometric Reflectance Imaging Sensor
SSC	.....	Saline-sodium citrate

Chapter 1

Introduction

1.1 Overview of dissertation

The primary outcome of this dissertation is the design and implementation of a new type of molecular assay for nucleic acids and proteins. We call this new assay a digital microarray because it is conceptually very similar to a conventional DNA or protein microarray, yet it provides enumerative ('digital') counting of the number of captured molecules. Digital microarrays are about 10,000-fold more sensitive than fluorescence microarrays yet maintain all of the strengths of the platform, including low cost and high multiplexing (i.e., many different tests on the same sample simultaneously). This large improvement in sensitivity means that digital microarrays might be able to perform all of the same tests as fluorescence microarrays, but with much higher precision and dynamic range. There may also be novel applications in medical diagnostics or biological research, where digital microarrays are able to meet performance requirements which could not be met by fluorescence microarrays.

Digital microarrays use gold nanorods to label captured target molecules on the array. A major part of developing this technology was the development of a robust and high throughput nanoparticle detector based on a technique called Single Particle Interferometric Reflectance Imaging Sensing (SP-IRIS). While working on this problem, we developed several concepts that were applicable not just to digital microarrays but also to SP-IRIS measurements more generally. In particular, we developed a quantitative optical model and intuitive picture of SP-IRIS imaging that

was found to be useful in the characterization of biological nanoparticles, such as exosomes and viruses. This work is discussed in Chapter 2.

Chapter 3 describes a method for performing high throughput detection of individual gold nanoparticles with SP-IRIS. Briefly, our high-throughput technique is able to detect all of the nanoparticles on an IRIS microarray approximately 100-fold faster than previous methods. It does so by using a low magnification objective with a much larger field of view. In fact, the scan speed and throughput of our method is now roughly equal to that of commercial fluorescence microarray readers.

Chapters 4 and 5 depart from optical system design and instead focus on the design and implementation of digital microarray assays which were enabled by the new high-throughput optical system. Briefly, Chapter 4 describes the design, implementation and optimization of a rapid and sensitive microarray assay for gene expression analysis. We are developing this assay as part of a rapid test for antibiotic resistance, which detects drug resistance through gene expression biomarkers rather than growth inhibition. Chapter 4 also includes a discussion of the fundamental performance limits imposed by mass transport (diffusion and convection) and reaction kinetics on microarray biosensors.

Finally, Chapter 5 describes three technologies that enabled sensitive kinetic measurements of nanoparticle binding and debinding. These are (a) a disposable microfluidic flow cell compatible with SP-IRIS, (b) a custom software that performs nanoparticle tracking in video data, and (c) a closed loop, programmable temperature controlled stage for thermodynamic studies of nucleic acids. We also show preliminary results in which we measure different melting temperatures for DNA-nanoparticle conjugates that are tethered to the chip by either perfectly-matched duplexes or duplexes with a single base pair mismatch. This approach may eventually have utility in applications which require sensitive detection and discrimination

of rare mutant DNAs, such as in monitoring the response of cancer to a targeted therapy.

Each of these chapters begins with a motivation section, and ends with a summary and discussion of future work. In this Introduction we have included two background sections to provide additional context for the dissertation as a whole. The first describes the various techniques with which nanoparticles (especially biological nanoparticles such as viruses and exosomes) can be detected and characterized with light. This is intended to frame the work described in Chapter 2. The second background section is a very brief survey of modern methods for nucleic acid analysis. This section is used to paint a picture of how digital microarrays may compare, and what niche this technology might fill in biomedical research or clinical diagnostics.

1.2 Optical detection of single nanoparticles

Many biological processes in health, disease, and modern medicine are mediated by nanoparticles 20 nm to 1000 nm in diameter. Research into the structure and function of biological nanoparticles (BNPs) have revealed their multifaceted roles in molecular sorting, homeostasis, cell signaling and various types of disease. Exosomes—a class of extracellular vesicles of size 30-100 nm—carry complex molecular payloads and are thought to have roles in cell-cell signaling, antigen presentation, immune suppression and inflammation (Kourembanas, 2015). Exosomes are also secreted by cancer cells, and are implicated in metastasis, tumor growth and angiogenesis (van der Pol et al., 2012). Unfortunately, optical characterization of exosomes in liquid media has proven extremely difficult due to their very small size and refractive index similarity to water (van der Pol et al., 2013).

Viruses are another broad category of BNP. As the most abundant biological agents on earth, viruses exhibit an enormously diverse range of evolutionary strategies

and morphologies (Lawrence et al., 2009). Sensitive direct detection characterization of viruses is commonly performed with either plaque assays (based on infectivity) or molecular tests, which detect viral genes or capsid proteins. These molecular techniques discard any information about virion shape or size, and may be unable to differentiate infectious virions from *virus-like particles*, which do not contain genetic material but may still elicit immune response (Lichty et al., 2004). Virus morphologies can be highly diverse, and mutations that cause defective morphologies also significantly reduce both replication and infectivity, suggesting a causal link (Lawrence et al., 2009; Berthoux et al., 1999; Clavel and Orenstein, 1990).

There are several different methods for measuring BNP structure. Electron microscopy provides exquisite resolution, and is the gold standard for sample characterization. Attempts to use electron microscopy for diagnostics have not yet been realized due to its high cost, low throughput, complexity, and the requirement for high concentrations of virions (Doane, 1980). Generally, these limitations are shared by other high resolution laboratory techniques such as near-field scanning optical microscopy, atomic force microscopy and surface-enhanced Raman spectroscopy (SERS) (Lange et al., 2001; Kuznetsov et al., 2003; van der Pol et al., 2013). Furthermore, it is difficult to image delicate particles such as exosomes with electron microscopy because they collapse when exposed to vacuum and result in structures which are likely different from native ones (Kourembanas, 2015).

Nanoparticle Tracking Analysis (NTA, Nanosight$^{\text{TM}}$) is an optical technique which determines the size of nanoparticles by measuring both their scattering cross section and diffusion coefficient, as they move about randomly due to Brownian motion (Filipe et al., 2010; Dragovic et al., 2011). NTA is comparatively simple and easy to use, and it can detect particles down to about 100 nm without using any fluorescent labeling. For comparison, flow cytometry cannot detect particles smaller than 200 nm,

which limits its use for viruses and exosomes (van der Pol et al., 2013). NTA requires a high concentration (picomolar) of particles, so it is a favored technique for characterizing nanoparticles during synthesis, or in other laboratory tests. Low sensitivity and lack of multiplexing (to simultaneously test for different types of BNPs) have been the main barriers to medical diagnostic applications.

In contrast to NTA, optical techniques which first capture the particles to a sensor surface have advantages in multiplexing and sensitivity. First, the sensor surface is almost always functionalized with a molecular coating that confers a specific molecular affinity. Preparing hundreds of arrayed regions of varied molecular affinity, in the form of a microarray, is an industry-standard technology that provides this family of sensors with high multiplexing capability. Second, the heterogeneity of the substrate-medium interface can be exploited to amplify the local electromagnetic field and enhance the captured nanoparticle's optical scattering. For example, single viruses can be detected using surface plasmon resonance imaging (Wang et al., 2010). Surface nano-patterning can achieve even higher sensitivity, but in many of those cases the electromagnetic field enhancement is nonuniform, so particle binding does not have the same effect in all places on the sensor. For example, surface plasmon resonance has been utilized to detect the binding of individual exosomes in real time using a gold film patterned with a periodic nanopore array, but since the optical signal from an exosome was a strong function of its precise position with respect to the pore, particle size could not be measured (Im et al., 2014). Micro-ring and whispering-gallery-mode optical resonator sensors share this problem of transduction heterogeneity, as do most extremely high-Q optical detectors in general (Vollmer and Arnold, 2008).

The Single Particle Interferometric Reflectance Imaging Sensor (SP-IRIS) is an optical biosensing technology that combines a flat multilayer dielectric substrate such as thermally-grown oxide on silicon with a reflection microscope to count and clas-

sify single immobilized nanoparticles. SP-IRIS is one of a growing family of optical sensors which can precisely enumerate individual nanoparticles bound to a planar surface, either for characterization of synthetic nanoparticles (Lindfors et al., 2004; van Dijk et al., 2005; van Dijk et al., 2007; Nie and Emory, 1997), label-free enumeration of virus or exosome vesicles from complex media such as blood serum (Wang et al., 2010; Boccara et al., 2016; Kukura et al., 2009), or single molecule detection where synthetic nanoparticles are used as specific labels (Patskovsky and Meunier, 2015). Proof of concept demonstrations have shown that SP-IRIS can be used for the sensitive detection of both viruses and exosomes from complex media such as serum or cerebrospinal fluid (Scherr et al., 2016; Daaboul et al., 2016).

Although it has always been theoretically possible to perform quantitative measurements of BNPs with SP-IRIS, this capability has not been experimentally realized until very recently. Chapter 2 begins with an explanation of the problems with past approaches and describes a new approach that overcomes them.

1.3 A brief survey of nucleic acid analysis techniques

Nucleic acids—DNA and RNA—are the molecular substrates on which genetic information is written. They are central to the growth and replication of all living organisms, and even that of proto-life such as viruses or plasmids. They are very important in modern medical diagnostics; cancer tumors are now regularly genotyped to guide therapy, and genetic analysis is used to track the spread of virulent infectious diseases.

The importance of nucleic acids has motivated continual development of new techniques to measure them. As it has turned out, no single technique has dominated all of the various applications of genetic analysis. Today we have a rather diverse and crowded ecosystem of different techniques, each of which fills a niche based on its

performance. Risking gross oversimplification, we propose that there are qualitatively three properties with which these techniques can be compared: 'Depth', 'Breadth', and 'Cost'. The first two terms have very specific definitions in the context of sequencing, but here we mean something much more general.

1. By 'Depth', we mean the sensitivity, specificity and dynamic range of the assay. Techniques which score highly can precisely quantify a particular sequence of interest, such as reporting the exact number of copies of a particular allele or isoform regardless of what other nucleic acids are present. The 'Depth' of an assay is important for identifying rare mutations within genetically heterogeneous tumors, for example.

2. By 'Breadth', we mean the amount of multiplexing in the assay—how many different genes can be interrogated at once. Genomic and transcriptomic assays powered by next generation sequencing (NGS) provide a complete, bias-free picture of all RNAs and/or DNAs in a sample, and are the gold standard here. 'Breadth' is a requirement in many areas of biology and medical research, such as in genetic susceptibility biomarker discovery studies.

3. By 'cost' we mean not just monetary cost but also complexity, reliability, and assay time. Cost is a primary concern in many medical diagnostic applications, especially for diagnostic screening.

In Figure 1·1, we use these three descriptors as a way to conceptually chart out the 'best in class' techniques that are commonly used today for RNA and DNA analysis. At the far right of the chart are techniques powered by NGS. They are also generally the most expensive. NGS techniques involve performing millions of

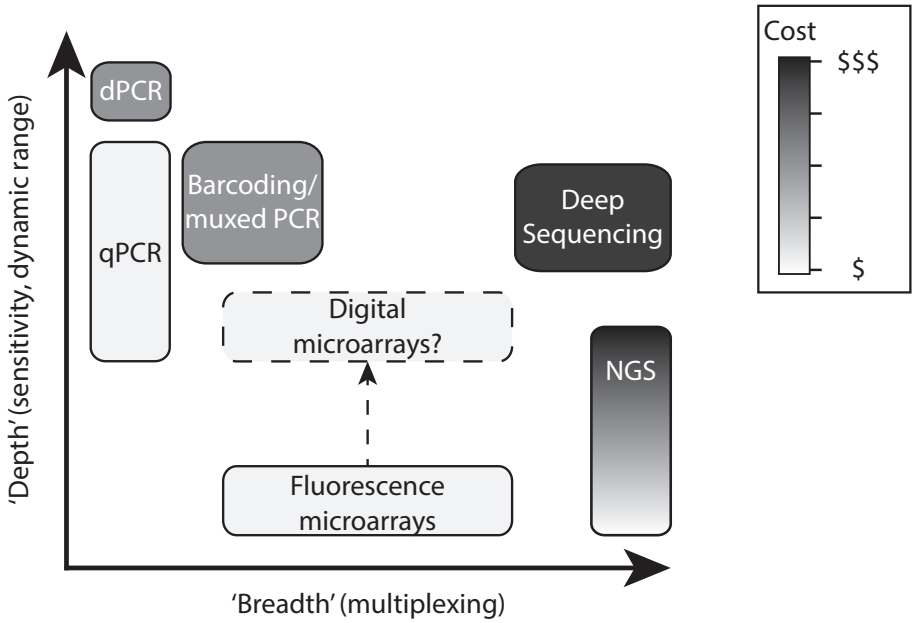

Figure 1·1: A qualitative chart of modern nucleic acid analysis techniques based on their breadth, depth and cost, as defined in text. dPCR, digital PCR; qPCR, quantitative PCR; muxed PCR, multiplexed PCR; NGS, next generation sequencing.

reads, each 50 to 200 base pairs long, and cost $500 to $1,000 per sample. The sensitivity can be pushed extremely far by performing many additional reads on fewer transcripts. These include techniques such as RNA-seq which are meant for measuring the transcriptome with high resolution. On the other hand, the cost of sequencing can be reduced by combining ('pooling') samples, but this also lowers sensitivity and dynamic range. Altogether these techniques remain comparatively complex and are usually handled by a core facility with dedicated staff. The assay typically takes between 2 to 7 days of machine time.

Another family of techniques are those based on polymerase chain reaction. Quantitative PCR (qPCR) involves amplifying a particular target locus by performing sequential rounds of DNA replication, and measuring the number of rounds it takes to reach a particular threshold copy number. Readout is typically using some type of fluorescent reporter such as a hydrolysis probe or DNA intercalating dye, such that

the fluorescence is proportional to the amount of amplicon. qPCR is very simple and affordable compared to sequencing, and extremely sensitive when performed correctly. At the extreme in sensitivity is digital PCR (dPCR), in which the sample volume is divided into thousands or millions of tiny volumes to separate every single DNA fragment into its own droplet. After amplification, a machine counts the number of droplets in which amplification occurred. Digital PCR is perhaps the most sensitive and specific nucleic acid test available—it is able to detect exceedingly rare mutant DNA sequences even if the sample also contains one million-fold more of a different allele (Vogelstein and Kinzler, 1999; Diehl et al., 2006; Baker, 2012; Chen et al., 2013). However, the Achilles' Heel of PCR-based techniques is multiplexing. Since they use fluorescence reporters they are limited by the bandwidth of the optical spectrum in the number of different fluorophores they can use. This sets a cap at about 10 to 15 different simultaneous tests which can be performed.

Microfluidics and microwell plates have been used to overcome this bandwidth cap, by dividing the sample into dozens or hundreds of different volumes and effectively performing a different PCR test in each well (multiplexed PCR, 'muxed PCR'). This effectively trades off some of the 'excess' sensitivity and dynamic range of PCR for greater multiplexing. These processes are moderately more complex and expensive than one-pot qPCR since they require microfluidic liquid handling or microwell plate manipulation, but still provide same-day results.

Another category of technique involve hybridization of target molecules to barcoded sensors, such as fluorescence barcodes (NanoString NCounter®) or barcoded microparticles (AbCam Firefly®) (Choi et al., 2012; Le Goff et al., 2015; Oikonomopoulos et al., 2016). As a whole, these techniques tend to compare similarly to multiplexed PCR, with a similar limit of detection (in the low attomolar range) and the ability to test for up to several hundred different targets. Like digital PCR these techniques

are more expensive than qPCR but can still be run by an independent lab, and take about 1 to 2 days to process a sample.

The final category of technique on our chart is DNA microarrays. A DNA microarray is a highly multiplexed test which utilizes a tiled array of 100 to 16 000 different DNA oligonucleotide probes. Target nucleic acids hybridize to the complementary probe. Fluorescent DNA microarrays use a fluorescent reporter to label the captured target molecules, and the total fluorescence of each microarray spot is measured using a fluorescence scanner. DNA microarrays can be 10x more multiplexed than even multiplexed PCR or barcoding methods, and are very affordable compared to sequencing. However, the sensitivity, specificity and dynamic range of fluorescent arrays are poor by comparison to all of the techniques mentioned previously.

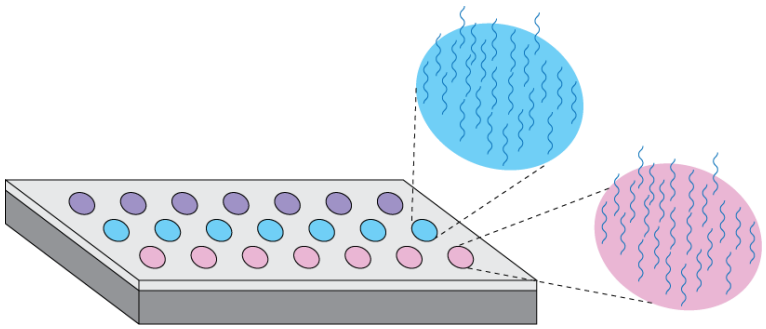

Figure 1·2: A schematic of a DNA microarray, showing multiplexed DNA probe spots. 100 to 10 000 different DNA capture probe spots can be tiled onto a single slide.

Despite this, fluorescent DNA microarrays continue to be widely used for gene expression analysis in settings such as clinical trials where the number of samples is too high to justify sequencing. Actually, the main limitations of microarrays (low sensitivity, high background and low dynamic range) are properties of fluorescence reporting, and are not inherent to the microarray platform. In this dissertation, we describe a DNA microarray reporting technique which uses gold nanoparticles instead of fluorescent molecules, and thereby increases the sensitivity of DNA microarrays by

about 10,000 fold. The use of gold nanoparticles does not increase overall cost, so we believe it will be a favored choice compared to sequencing when assay speed and cost are primary concerns. In Chapter 4 we discuss rapid antibiotic susceptibility testing as one potential application area.

Chapter 2

Quantitative interferometric reflectance imaging of single nanoparticles

2.1 Motivation

Although SP-IRIS has been used in a variety of contexts to detect nanoparticles, attempts to determine particle size and shape have fallen short. Previous studies have shown qualitative correlations between the size of a captured nanoparticle and the corresponding visibility of that particle, and have attempted to build empirical sizing 'rulers' by using particles of known sizes as a metric (Daaboul et al., 2010; Reddington et al., 2013; Daaboul et al., 2014; Daaboul et al., 2016). Unfortunately, these sizing rulers have proven to be inconsistent and inaccurate, for reasons which we explain in the next section.

An alternative method of measuring particle size would be to use a validated optical model to back-calculate the size of a particle, based on its brightness. Recently, quantitative optical simulations using the dipole approximation were developed (Avci et al., 2016; Trueb et al., 2017). We found that we were able to use these simulations to accurately predict the optical signature of particles of a known size, but we were not necessarily able to go the opposite way—that is, to measure the size of an *unknown* particle. This turned out to be connected to the bewildering experimental observation that particles of different sizes did not seem to be in focus at the same image plane.

This observation also made it difficult to know whether the instrument was in

focus. If not every particle was visible in every z-position, which position was best? In early work, a compromise was made: the focus plane was defined as the plane in which the most particles were detectable (Reddington et al., 2013). Predictably however, attempts to use this method to measure particle sizes were still unsuccessful since some particles were only partially 'in focus', and others were clearly being missed entirely.

Later work attempted to overcome this problem by acquiring z-stacks of images, in which multiple frames are acquired while changing the focus position by regular intervals. To detect all the particles, the maximum brightness at each (x, y) position (through the z-stack) was measured, which somewhat reduced the problem of missing particles but did not solve the problem of accurately measuring particle size. Eventually, Jacob Trueb made the breakthrough observation that measuring the difference between the maximum and minimum at each (x, y) position resulted in much more uniform measurements when measuring a monodisperse population of particles (Trueb et al., 2017). At around the same time, Oguzhan Avci made the key observation of simulation results that reducing the illumination to a single plane wave of normal incidence greatly improved the visibility of particles (Avci et al., 2017). These two observations were crucial in the development of the picture we describe next.

2.2 Nanoparticle detection with interferometric reflectance imaging

The IRIS substrate (Figure 2·1a) consists of a thin film of thermally grown oxide on polished silicon. This substrate is imaged with a reflectance microscope (Figure 2·1b), and individual immobilized nanoparticles are visible as diffraction-limited spots.

The IRIS substrate enhances the visibility of immobilized nanoparticles through two synergistic yet highly coupled mechanisms of light interference. The first mech-

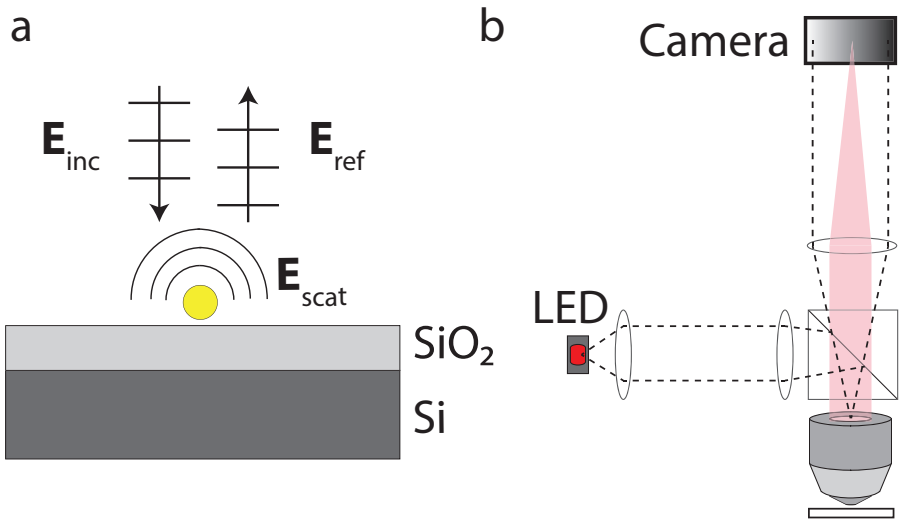

Figure 2·1: (a) A schematic of the IRIS substrate and the light fields described in text; Si, polished silicon; SiO_2, thermal oxide. Incident light ($\mathbf{E}_{inc}$) is both reflected by the substrate ($\mathbf{E}_{ref}$) and scattered by the immobilized nanoparticle ($\mathbf{E}_{scat}$). (b) The SP-IRIS instrument consists of a simple reflectance microscope with illumination provided by an LED.

anism of enhancement is that the substrate reflects much of the forward-scattered light, which then constructively interferes with back-scattered light and increases the total back-scattering as compared to a transmitting substrate such as glass.

The total resulting back-scattered field (denoted $\mathbf{E}_{scat}$) changes with the thickness of the SiO_2 film. In Figure 2·2a-d we have plotted the Poynting vector magnitude (i.e., the radiation pattern) of $\mathbf{E}_{scat}$ for a 100 nm spherical virus ($n = 1.5$) on a range of IRIS substrates with different film thicknesses (a-c) as well as a transparent glass substrate (d). In these radiation plots, the shape of the balloon shows the direction of radiation, and a larger balloon means the radiation is more intense. For all of these cases, the illumination is a linearly polarized plane wave with normal incidence and a wavelength of $\lambda = 530$ nm.

There are several things to note here. First, $\mathbf{E}_{scat}$ is much larger for the SP-IRIS substrates than for the glass substrate, by more than four times—this is the first

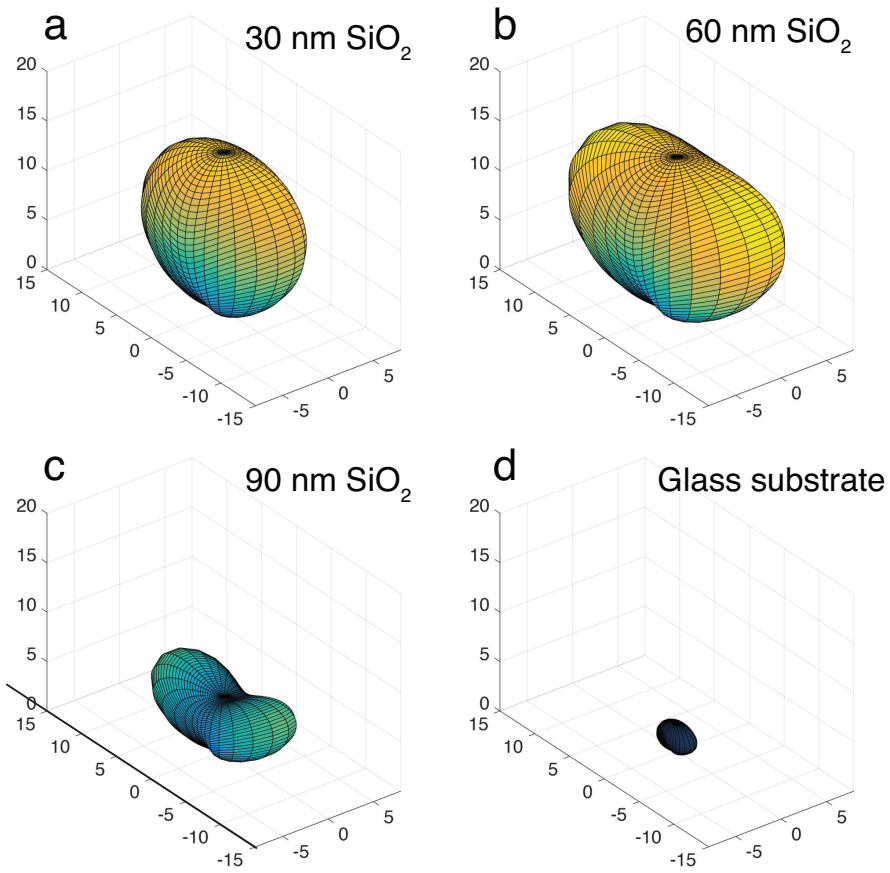

Figure 2·2: 3D simulated plots of the Poynting vector magnitude of $\mathbf{E}_{scat}$ of a 100 nm virus particle ($n = 1.5$) on SP-IRIS substrates with (a-c) range of film thicknesses, compared with (d) a glass substrate (arbitrary units).

'enhancement' we mentioned earlier. Second, the size and shape of the radiation pattern change with the film thickness. This is because the path length difference between the forward- and back-scattered fields depends on the angle of the rays. The path length difference for rays at 45° is not the same for the rays at 0°, for example. Third, note that radiation patterns do not have rotational symmetry about the optical axis (the z-axis, Figure 2·3a). This is because the linearly polarized illumination primarily excites a single dipole mode in the particle, and this dipole does not radiate parallel to its orientation.

The final and perhaps most subtle observation is that the majority of the scattered light propagates away from the optical axis. This is more apparent if we integrate the radiation patterns in Figure 2·2a-c around the optical axis, and plot the distribution of rays with different polar angles (Figure 2·3b). A water immersion microscope objective with a numerical aperture (NA) of 0.9 will collect all rays with a polar angle $\theta < 42.5°$, and half of those rays have a polar angle >28°.

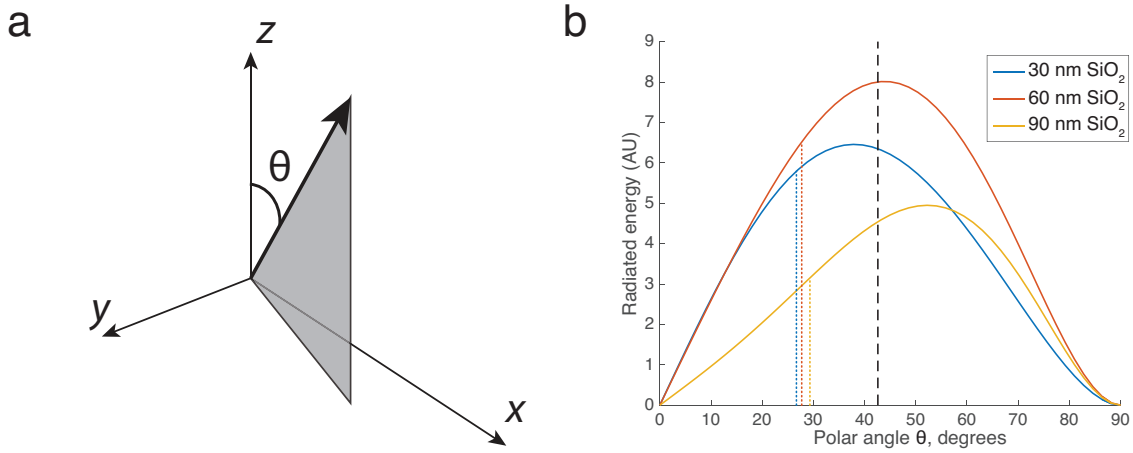

Figure 2·3: (a) Coordinate system showing the polar angle θ for a particular ray of scattered light. (b) Distribution functions of $\mathbf{E}_{scat}$ vs polar angle for the cases shown in Figure 2·2(a-c). The dashed line indicates the maximum collection angle of a 0.9 NA water-immersion objective. Dotted lines indicate the average polar angle of the collected light, for each case.

The second mechanism of enhancement is that the scattered fields are detected interferometrically instead of directly. In interferometric detection, rather than directly detecting the faint scattered light against a dark background, the scattered light is interfered with a reference light beam and the interference pattern is recorded:

$$\begin{aligned} I(\mathbf{r}) &= |\mathbf{E}_{ref}(\mathbf{r}) + \mathbf{E}_{scat}(\mathbf{r})|^2 \\ &= |\mathbf{E}_{ref}|^2 + |\mathbf{E}_{scat}|^2 + 2|\mathbf{E}_{ref}||\mathbf{E}_{scat}|\cos(\phi). \end{aligned} \tag{2.1}$$

Here, ϕ is the difference in phase between the scattered light and the reference light. This method is also called optical homodyning, and allows measurements of the signal's amplitude ($|\mathbf{E}_{scat}|$) instead of intensity ($|\mathbf{E}_{scat}|^2$). In the context of detecting faint light scattering, this has two advantages over direct measurement: one theoretical and one practical. Theoretically, interferometric measurements of light amplitude are useful for detecting small nanoparticles since the scattering intensity of a nanoparticle with diameter D scales with D^6, yet the scattering amplitude scales with D^3 (Lindfors et al., 2004). On the experimental side, interferometric detection avoids some sources of noise associated with measurements of faint light, including camera read noise and stray light. In interferometric detection, the reference can be increased until the mixed intensity $I(\mathbf{r})$ is much larger than these sources of variability (we discuss this in more detail in Chapter 3).

To perform interferometric detection in SP-IRIS, the specular reflection by the substrate $\mathbf{E}_{ref}$ (Figure 2·1) is also imaged onto the camera. Thus, the reflected field acts as the reference. At the camera, light scattered from a nanoparticle forms a diffraction-limited perturbation to the image of the reflected field (Figure 2·4a). The difference between the optical paths traversed by $\mathbf{E}_{scat}$ and $\mathbf{E}_{ref}$ to the sensor is $< 1\,\mu\text{m}$, enabling the use of a partially coherent LED instead of a highly-coherent laser beam.

The final optical setup for SP-IRIS is therefore advantageously simple compared to other interferometric nanoparticle detectors, since removing the requirement for coherent illumination avoids many of the challenges inherent to coherent light imaging such as laser speckle and stray reflections (Mitra and Novotny, 2013; Kukura et al., 2009). However, this simplicity comes at the expense that the path length (i.e., phase) of the reflected field cannot be adjusted independently from that of the scattered field. Rather, it turns out that the phase angle ϕ between the two fields at the image plane is a strong function of the focus position of the microscope objective, provided that the illumination is limited to normal-incidence rays by radically under-filling the back aperture of the objective. This is because a particle illuminated with a plane wave of normal incidence will scatter light mostly with larger polar angles (as described earlier) yet the specularly reflected field only travel in one direction: back along the optical axis ($\theta \approx 0°$). Since the scattered and reflected fields are traveling (mostly) along paths with differing θ, changing the focus position of the objective alters the phase angle (ϕ) between them. Equivalently: within the angular spectrum representation, the plane wave components of the reflected field consists of rays that are mostly along the optical axis ($k_{z:ref} \approx |\mathbf{k}|$), while the majority of the scattered light is in plane wave components which are traveling at a significant polar angle ($k_{z:scat} < |\mathbf{k}|$). Changing the focus position the microscope objective by dz changes the path length of the reflected reference field by $|\mathbf{k}|dz$, and the off-normal scattered fields by less: $k_{z:scat}dz = |\mathbf{k}| \cos\theta dz$, where θ is the polar angle of a particular off-axis ray.

To help elucidate this, consider the intensity at the center of the diffraction-limited image of a nanoparticle on an SP-IRIS substrate (100 nm of SiO_2) as the focus position z is swept across the chip surface (Figure 2·4). We call the resulting curve the 'defocus profile'. If only the scattered light was collected (as in darkfield microscopy) this

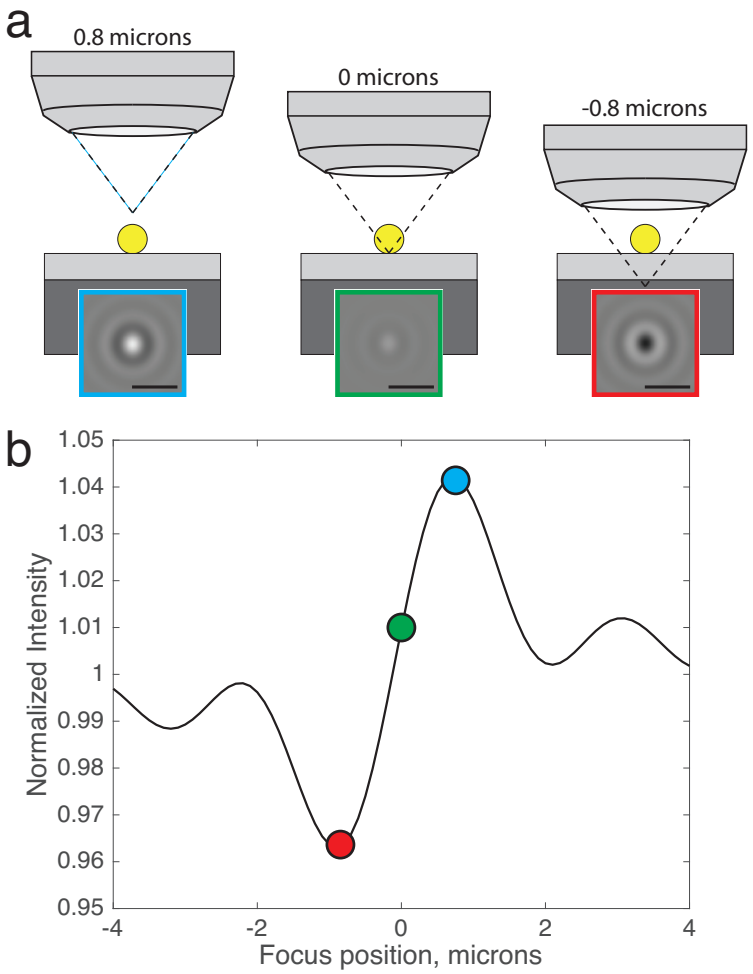

Figure 2·4: (a) Simulated images of a 100 nm virus on an IRIS substrate with the microscope focal plane at three different positions with respect to the substrate top surface (NA = 0.9, scale bars are 1 µm). (b) The 'defocus profile': simulated normalized intensity at the center of the diffraction-limited image is plotted as a function of focus position, with the three focus positions in (a) labeled.

curve would trace out the axial point spread function of the microscope, which would have a maximum of $|\mathbf{E}_{scat}|^2$ when the particle is in focus, and decrease to 0 as the particle moves out of focus. However, when the reflected light is also collected, the background intensity (when out of focus) is not 0 but $|\mathbf{E}_{ref}|^2$, and fringing is observed in the defocus profile (Figure 2·4b). Since the reflected light is much brighter, the scattered fields are detected as a faint perturbation. Here we should define 'normalized intensity' as the ratio of the intensity of the combined scattered and reflected fields with that of the reference field alone, (i.e. when out of focus, or in the absence of a particle):

$$\text{Normalized Intensity} = \frac{|\mathbf{E}_{scat} + \mathbf{E}_{ref}|^2}{|\mathbf{E}_{ref}|^2} \tag{2.2}$$

In this example, the normalized intensity fluctuates between 0.96 (darker than the background) and 1.04 (brighter than the background) along the defocus profile (Figure 2·4b) as the particle moves into and out of focus and the phase angle ϕ is processed.

The defocus profile is a crucial measurement for quantitatively determining $|\mathbf{E}_{scat}|$ since the fringe amplitude can not generally be determined from any single image in the z-stack. Indeed, precisely measuring $|\mathbf{E}_{scat}|$ from the defocus profile is still non-trivial since the axial point spread function effectively acts as a modulating envelope. Depending on the elevation or size of a particle, the defocus profile may have a single large antinode at $z = 0$, or a node at $z = 0$ with two antinodes as in Figure 2·4b, or something in between. This is due to the fact that increasing the size of the particle will increase the elevation of its centroid, and a change the centroid position by as little as $\lambda/20$ will result in a noticeable shift in the position (along the z-axis) of the fringe peaks (Trueb et al., 2017).

In almost all previous work with SP-IRIS, the focus plane at which the highest number of particles were visibly brightest was chosen either by eye or by a custom auto-focus algorithm, and a single image was saved for later analysis. It should now

be clear however that such a process cannot hope to accurately measure $|\mathbf{E}_{scat}|$ for a population of nanoparticles of heterogeneous or otherwise unknown size. As we shall see, the amplitude of the scattered field (read: the amplitude of the fringes in the defocus profile) can be approximately measured by taking the difference between the profile maximum and minimum.

2.3 A quantitative model of interferometric imaging of arbitrary nanoparticles

The problem of numerically simulating the steady-state optical scattering of an arbitrary particle involves finding a self-consistent and time harmonic numerical solution to Maxwell's equations throughout a region of interest with relevant boundary conditions. Beyond special cases where the symmetry of the problem permits an analytical solution via Mie scattering theory, problems in nanoparticle scattering are most often solved via discrete numerical methods such as the boundary element method (BEM) or discrete dipole approximation (Sorgenfrei et al., 2011).

In the case of a particle embedded in a homogeneous and isotropic medium, Maxwell's equations can be simplified to a surface integral equations at the nanoparticle-medium interface (García de Abajo, 2002). BEM simulations therefore only require that the two-dimensional interface be meshed, which makes simulations much faster compared to Finite-Different Time Domain or other volume-element methods. Several implementations of the boundary element method have been published and made freely available for academic use. We used the Magnetic Nanoparticle Boundary Element Method (MNPBEM) toolbox because (a) it was implemented in MATLAB, our preferred language, (b) it included formulation for the scattered far fields of a particle on layered media, as described by Novotny (Novotny and Hecht, 2006), which simplified our implementation, and (c) it provided excellent published documentation and

examples (Hohenester and Trügler, 2012; Waxenegger et al., 2015).

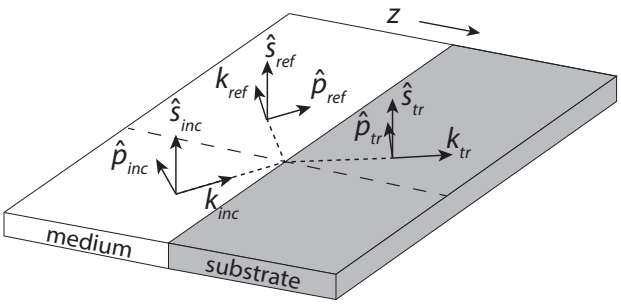

Figure 2·5: Coordinate system used to calculate the reflected field, showing the plane of incidence and coordinate unit vectors (Eqs. 2-6). The IRIS chip is the 'substrate'. Note the direction of the z-axis here. An incident plane wave with $\mathbf{k}_{inc}$ is decomposed into components perpendicular ($\hat{\mathbf{s}}$) and parallel ($\hat{\mathbf{p}}$) to the plane of incidence.

The overall optical simulation essentially consists of three parts. First, we define the system geometry and use the MNPBEM toolbox to calculate the surface charge distributions on the nanoparticle-medium interface in response to a monochrome incident plane wave $\mathbf{E}_{inc}(\mathbf{r})$, and compute from them the resulting far field scattering, $\mathbf{E}_{\infty}$. The scattered far fields are expressed as the complex-valued magnitudes of plane wave components (i.e., far field components of the angular spectrum): $\mathbf{E}_{\infty} = \mathbf{E}_{\infty}(k_x, k_y)$. The unmagnified image formed by the microscope may therefore be obtained simply by evaluating the canonical angular spectrum integral over the collection solid angle of the objective, with the appropriate prefactors (Novotny and Hecht, 2006; Mandel and Wolf, 1995):

$$\mathbf{E}_{scat}(\mathbf{r}) = \frac{\mathrm{i}}{2\pi} \iint\limits_{\theta \leq \theta_{max}} \mathbf{E}_{\infty}\left(k_x, k_y\right) e^{i(k_x x + k_y y + k_z z)} \frac{1}{k_z}\, dk_x\, dk_y \tag{2.3}$$

Second, the reflected field $\mathbf{E}_{ref}(\mathbf{r})$ is calculated. For this, we find the equivalent complex Fresnel reflection coefficients of the thin film structure (r_s and r_p) using a full vector implementation of the matrix transfer method, as described by Saleh (equations not shown) (Saleh and Teich, 2007). The reflected field is then:

$$\mathbf{E}_{ref}(\mathbf{r}) = r_s \left(\mathbf{E}_{inc} \cdot \hat{\mathbf{s}}_{inc}\right) \hat{\mathbf{s}}_{ref} + r_p \left(\mathbf{E}_{inc} \cdot \hat{\mathbf{p}}_{inc}\right) \hat{\mathbf{p}}_{ref} \tag{2.4}$$

Here, $\hat{\mathbf{s}}_{inc}, \hat{\mathbf{p}}_{inc}, \hat{\mathbf{s}}_{ref}$, and $\hat{\mathbf{p}}_{ref}$ are the polarization unit vectors defined as in Figure 2·5, and $\mathbf{k}_{xy}$ is the component of the wave-vector $\mathbf{k}$ in the (x, y) plane:

$$\hat{\mathbf{s}}_{inc} = \hat{\mathbf{z}} \times \frac{\mathbf{k}_{xy}}{|\mathbf{k}_{xy}|} \tag{2.5}$$

$$\hat{\mathbf{p}}_{inc} = \hat{\mathbf{s}}_{inc} \times \frac{\mathbf{k}}{k} \tag{2.6}$$

$$\hat{\mathbf{s}}_{ref} = \hat{\mathbf{s}}_{inc} \tag{2.7}$$

$$\hat{\mathbf{p}}_{ref} = \begin{bmatrix} 1 & 0 & 0 \\ 0 & 1 & 0 \\ 0 & 0 & -1 \end{bmatrix} \cdot \hat{\mathbf{p}}_{inc} \tag{2.8}$$

Third and finally, the resulting image formed at the detector $\mathbf{I}(\mathbf{r})$ is determined by coherently adding the scattered and reflected fields at the image plane position $\mathbf{r}$:

$$I(\mathbf{r}) = |\mathbf{E}_{ref}(\mathbf{r}) + \mathbf{E}_{scat}(\mathbf{r})|^2 \tag{2.9}$$

In many cases, the illumination cannot be approximated by a single plane wave. The illumination profile at the surface is then decomposed into a discrete sum of plane wave components via the angular spectrum representation, and summed incoherently:

$$I_{tot}(\mathbf{r}) = \iint\limits_{\theta_{inc} \leq \theta_{max}} I(k_x, k_y, \mathbf{r})\, dk_x\, dk_y \tag{2.10}$$

In the case of Köhler illumination using an LED, these plane wave components are incoherent since each component corresponds with a different physical position on the diode and therefore an independent, uncorrelated photon emission event. The final image, therefore, consists of the incoherent superposition of the responses caused by each illumination component, where each reflected plane wave is coherent with its

corresponding induced scattered field but no others (Bohren and Huffman, 2008).

2.4 Validation of the model

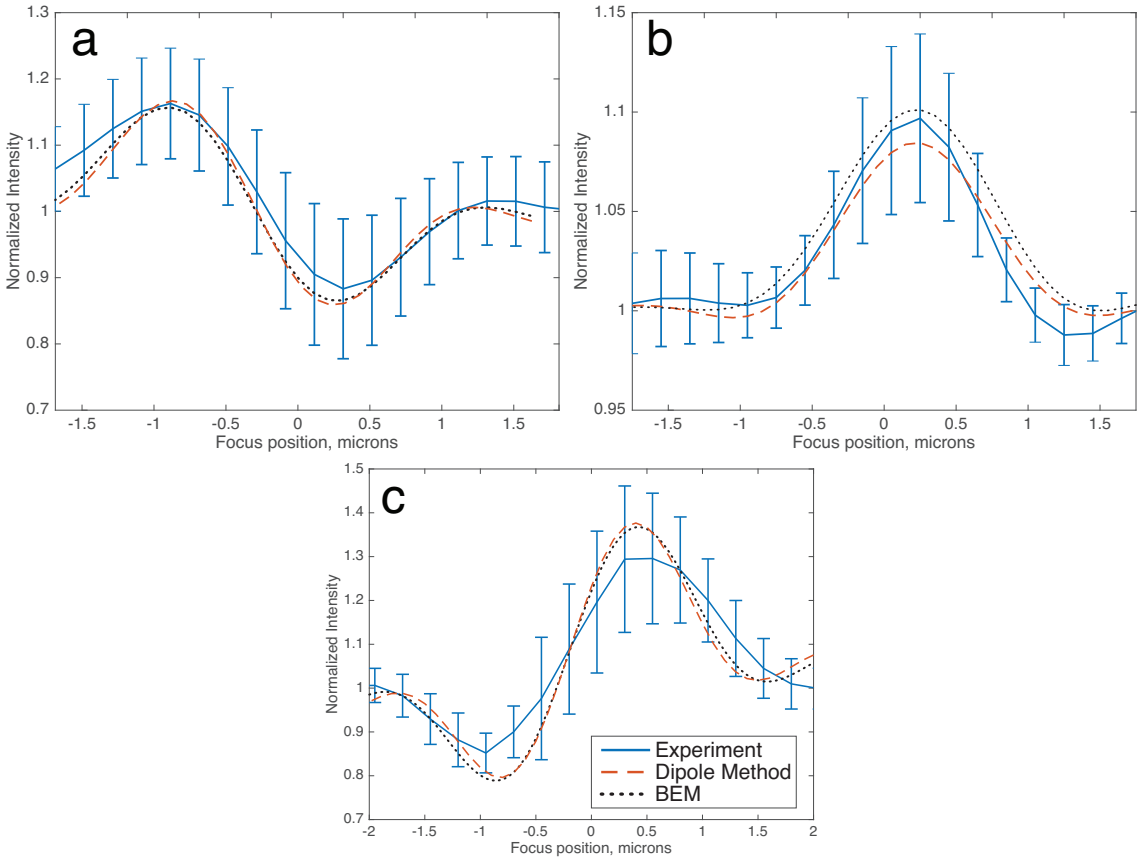

Figure 2·6: Validation of BEM simulations against the dipole approximation method and experimental measurements, in the case of (a) 60 nm gold spheres (34 particles), (b) 100 nm diameter polystyrene (n=1.60) spheres (63 particles), and (c) 145 nm polystyrene spheres (24 particles), showing good agreement amongst all three for the entire range of particle sizes. (NA $= 0.8, \lambda = 525$ nm in (a-b), $\lambda = 630$ nm in (c)).

To validate our model we compared the results of simulations to both experimental measurements and dipole simulations (Avci et al., 2016). 60 nm diameter gold, 100 nm polystyrene (n=1.60) and 145 nm polystyrene spheres were diluted in DI water and spin-coated onto an SP-IRIS substrate with 100 nm oxide film. Note that nanopar-

ticles on the substrate must be sufficiently far apart so that their diffraction-limited images would not overlap (at minimum about 2 µm). Z-stacks of images were taken over a 4 µm range of focus positions in 200 nm increments, resulting in a data-cube $I(x, y, z)$. High-pass spatial filtering followed by thresholding was used to identify the centroid of the diffraction-limited image of each particle, and the normalized intensity of the centroids were measured as a function of focus position to measure experimental defocus profiles. Simulations of the defocus profile of these particles were generated using both the BEM and dipole methods and found to be in agreement with each other as well as with the average experimental curve (Figure 2·6).

We then investigated whether the BEM approach could be used to correctly predict the image of asymmetric particles such as nanorods. 25×71 nm gold nanorods (25-650, Nanopartz, Loveland CO) were spun onto an SP-IRIS substrate using the same method described earlier, resulting in individually immobilized particles with random orientations. To account for the distribution of orientations, a linear polarizer in the illumination path was rotated over the interval $\theta = (0°, 180°)$ in 15° increments (Figure 2·7a-c; note, this is not the polar angle θ from before!). A z-stack was acquired for each position of the polarizer, resulting in a data-hypercube of $I(x, y, z, \theta)$. A sinusoid with form $I(x, y, z_0, \theta) = V \sin(2\pi\theta + H) + 1$ was fit to every image pixel (x, y) in a particular plane $z = z_0$ at which particles were most visible to the eye. Fitted coefficients $H(x, y)$ and $V(x, y)$ were then represented respectively as the Hue (color) and Value (brightness) of an HSV image, in which particles of similar orientation are represented with similar false colors (Figure 2·7d). The average defocus profiles of a nanorod illuminated along its longitudinal axis were found to be in agreement with corresponding BEM simulations (Figure 2·7e).

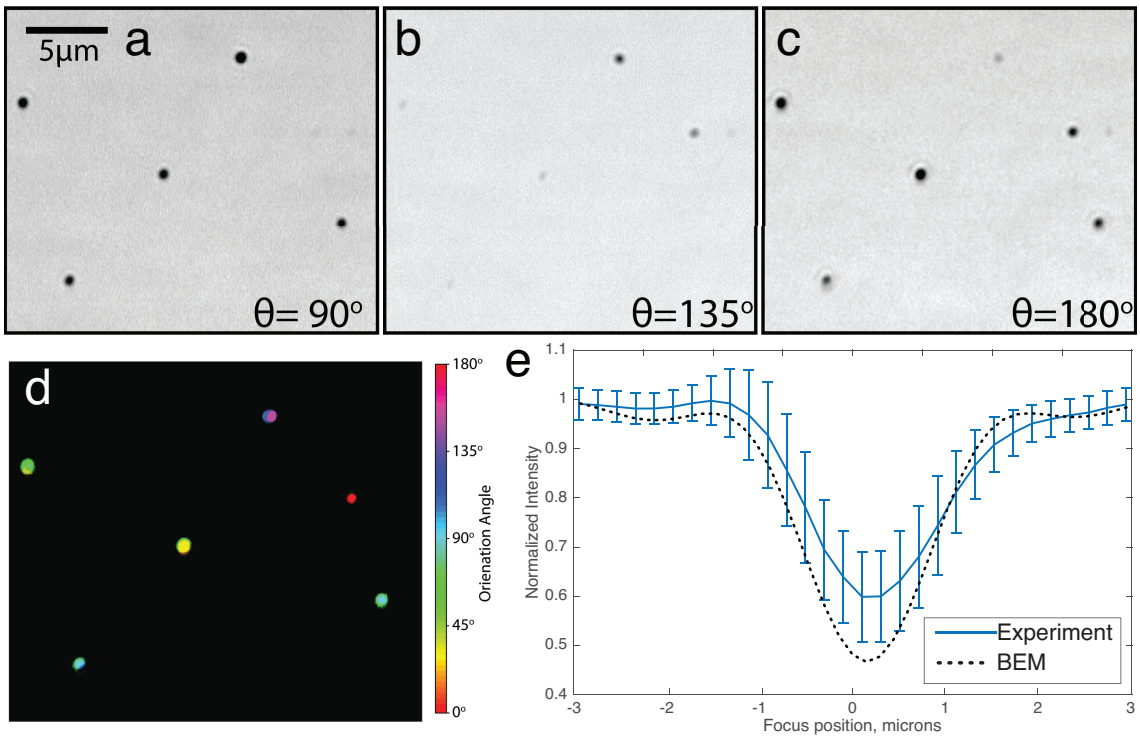

Figure 2·7: Validation of BEM simulations of gold nanorods. (a-c) Cropped slices from the 25 by 71 nm gold nanorod dataset described in text, where θ is the illumination polarization angle. (d) Hue-Saturation-Value representation after fitting a sinusoid to each spatial position pixel as a function of illumination polarization angle. Value (i.e., brightness) indicates the presence of a particle and Hue (i.e., color) indicates particle orientation. (e) Comparison of simulated and measured normalized intensity of a 25 by 71 nm gold nanorod aligned parallel to the illumination polarization direction, as a function of defocus (59 particles, 50x 0.8 NA, $\lambda = 630\,\text{nm}$).

2.5 Design optimization for detection and sizing of biological nanoparticles

Many biological nanoparticles (BNPs) of interest are in the range of 50 and 150 nm in diameter, with a refractive index of about $n = 1.5$ for virus-like particles and as low as $n = 1.38$ for exosome vesicles (Mitra et al., 2012; Van Der Pol et al., 2012; Gardiner et al., 2014). Our objective is to maximize the visibility of this category of BNPs while immersed in water. Specifically, we wish to design an acquisition process that can not only detect but also accurately measure the size of BNPs within the range 50-150 nm.

Towards this end, we simulated the defocus profile of a 100 nm virus ($n = 1.5$) on SP-IRIS substrates with a range of oxide film thicknesses (Figure 2·8). Here, the illumination is modeled as a single plane wave of normal incidence with $\lambda = 530$ nm, and the objective NA is 0.9. As expected, constructive self-interference of forward- and back-scattered light depends strongly on the correct selection of oxide film thickness, and it is periodic with $\lambda/2n$. Rather than selecting the thickness at which the normalized intensity is simply either maximum or minimum, we use the normalized intensity range (NI Range, Figure 2·8b) as the objective function. This parameter is selected as an engineering trade-off; the ideal case would be to perform numerical fitting of the defocus profile at every pixel in the image to accurately measure $|\mathbf{E}_{scat}|$, but this is prohibitively computationally expensive. By comparison, NI Range is an approximation that can be calculated rapidly. Another useful metric is the peak plane separation, which is the distance (in z) between the two focus planes of maximum and minimum NI. The peak plane separation is an approximate measurement of the period, which like NI Range can be measured easily. When the NI Range is optimized, the optimal oxide film thickness turns out to be about 50 nm (Figure 2·8c). When this oxide film thickness is used, the NI Range is a strong

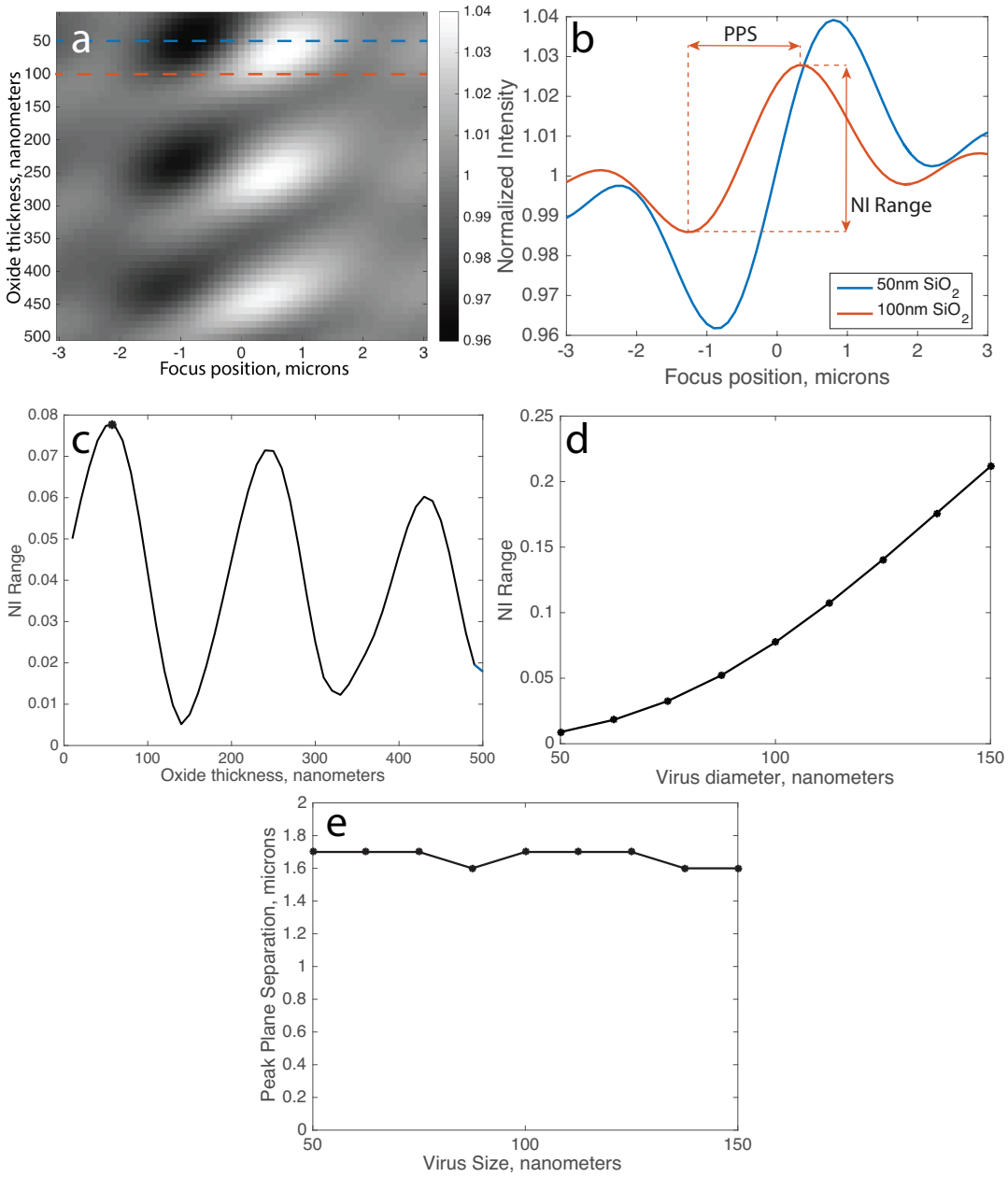

Figure 2·8: (a) Simulations of normalized intensity (at image center) of a 100 nm virus as a function of oxide film thickness and objective focus position. Two slices of this simulation where the film thickness is 50 or 100 nm are indicated by the dotted lines and plotted in (b) as defocus profiles. (c) NI Range for the range of oxide film thicknesses. (d) NI Range and (e) Peak plane separation are simulated for spherical virus between 50 and 150 nm in diameter on a 50 nm oxide film.

monotonic function of particle size (Figure 2·8d). However, the peak plan separation is nearly constant for a wide range of particle sizes, as would be expected (Figure 2·8e).

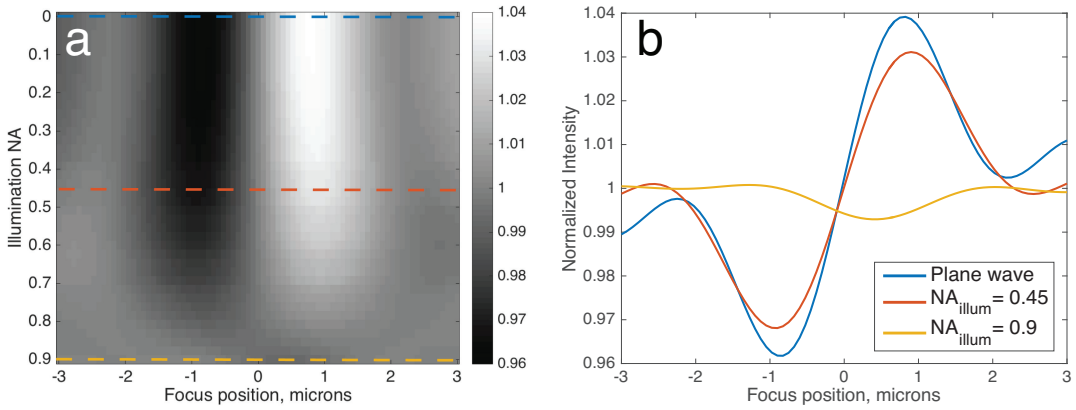

Figure 2·9: (a) Simulations of normalized intensity (at image center) of a 100 nm virus as a function of illumination NA and focus position. (b) The defocus profiles when illumination angles are restricted to a single plane wave (NA = 0), or NA = 0.45 or NA = 0.9.

As mentioned earlier, SP-IRIS uses Köhler illumination to provide approximately flat and uniform illumination over the objective field of view. In Köhler illumination, the illumination source is imaged to the back pupil of the objective using two lenses in a 4-f configuration. However, this poses a challenge since in order to illuminate the surface with approximately plane wave illumination, the source should be focused onto a pinhole spatial filter and this pinhole should be imaged to the objective back pupil. This approach is inefficient from a power perspective since it will discard the vast majority of the source's light (Büttner and Zeitner, 2002). It would be advantageous to know the rate at which fringe visibility decreases with increasing illumination numerical aperture (illumination NA), so that a trade-off may be made. We therefore simulated the the defocus profile of a 100 nm virus on the optimal oxide film thickness of 50 nm, in water, while sweeping the illumination NA from 0 to 0.9 (Figure 2·9a). The collection NA is constant (0.9) for all cases, and the illumination is modeled as having uniform intensity over the chosen solid angle. As expected,

illuminating with the full NA of the objective greatly decreases fringe visibility (Avci et al., 2017). However, we find that an illumination NA as high as 0.45 (i.e., objective fill factor $f_0 \sim 0.5$) may be used while still retaining $\sim 80\%$ of the NI Range signal (Figure 2·9b).

Finally, we considered the impact of using a different film material, instead of thermally grown oxide. Silicon nitride can also be deposited on polished silicon in very flat films, and has a higher refractive index (n=2.0-2.3 depending on the deposition protocol). To investigate the impact of changing the film material, we simulated the defocus profile of a 100 nm virus, as before, on SP-IRIS substrates with a range of nitride film thicknesses where n=2.05 (Figure 2·10).

As expected, the results are qualitatively similar to those with an oxide film. However, the peak NI Range is nearly twice that of optimized oxide (0.14 vs. 0.08). The reason for this improvement is that the refractive index of nitride is closer to the geometric mean of silicon and water, which means it forms an efficient anti-reflection coating when the thickness is an integer multiple of $\lambda/2n$ (Figure 2·10c). The minimization of $|\mathbf{E}_{ref}|$, rather than the maximization of $|\mathbf{E}_{scat}|$, is now the driving factor in increasing particle visibility. Since the scattered fields propagate mainly at high angles, and since the reflectivity is a function of incidence angle, it may therefore be possible to find a configuration in which $|\mathbf{E}_{ref}|$ is attenuated to the minimum required level while $|\mathbf{E}_{scat}|$ is simultaneously large.

2.6 Conclusions

2.6.1 Summary

In this Chapter we have described IRIS as a homodyne interferometer, in which the phase between the scattered (signal) and reflected (reference) light can be modulated by changing the focus position. We showed how the normalized intensity range (NIR)

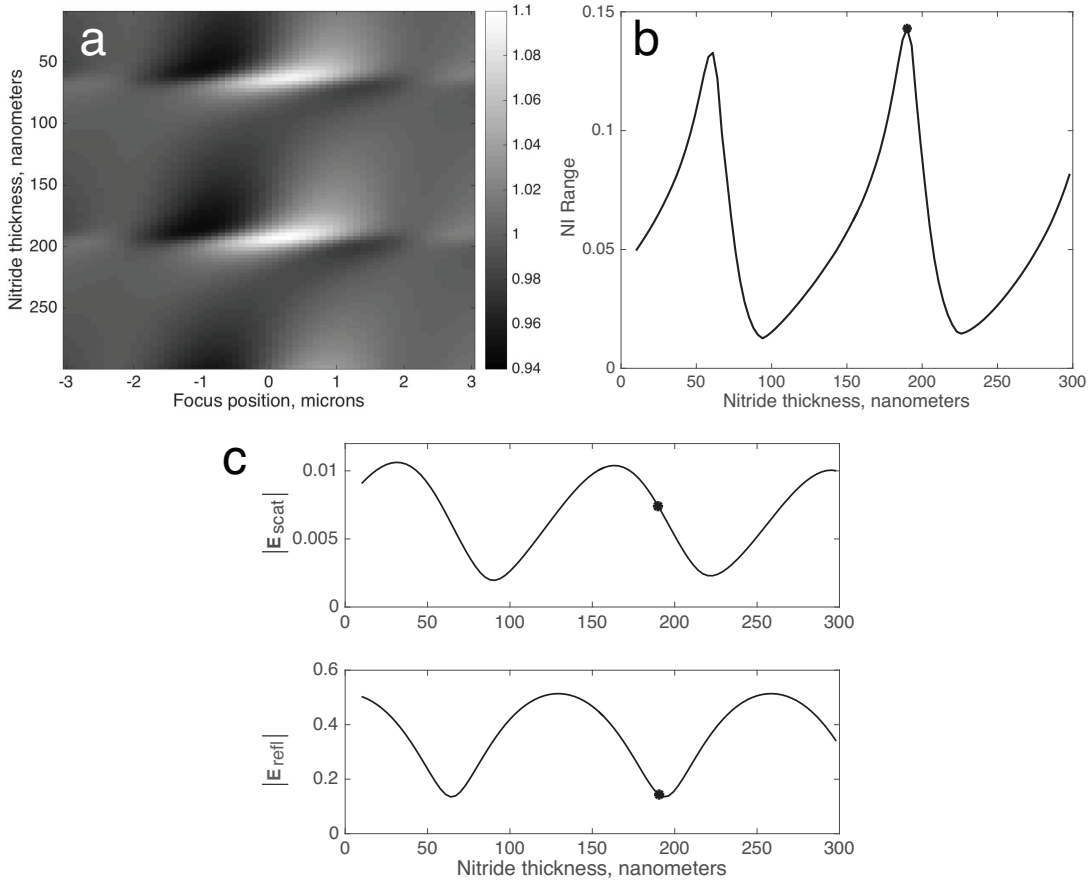

Figure 2·10: (a) Simulated defocus profiles of a 100 nm virus on a range of nitride films (n=2.05). (b) Optimal NI Range is achieved with a film thickness of 190 nm. (c) The field magnitudes $|\mathbf{E}_{scat}|$ (top) and $|\mathbf{E}_{ref}|$ (bottom) are plotted individually, with the optimal nitride thickness indicated.

is a good approximate measurement of the scattered field in almost every case, and that it can be measured by simply taking the maximal difference in intensity through the z-stack at each position in the image.

We also introduced an optical model of SP-IRIS imaging that uses the Boundary Element Method, and as such can be used to accurately simulate the image particles of any arbitrary size or shape. We validated this optical model by comparing it to both experimental results and the results of a different optical model. Finally, we used this model to rapidly optimize the design of the SP-IRIS instrument and chip for performing quantitative imaging of single nanoparticles.

2.6.2 Future work

We have only showed simulation results that suggest nitride substrates may improve visibility. These observations must still be tested experimentally.

Although the picture of SP-IRIS we have described is accurate to our knowledge, the practice of moving the focus position and acquiring z-stacks to measure the normalized intensity range has several shortcomings. Foremost is that the NIR is only an approximate measurement of the scattered field.

One way to overcome this shortcoming would be to use some type of spatial light modulator (SLM) in the imaging path. As described earlier, at the image Fourier plane the reference light is focused to a relatively small region in the center of the optical axis, while the scattered light is distributed. An SLM could be used to only modulate the phase of the center part of the Fourier plane, and thus allow a much more accurate (but not perfect) measurement of the scattered field. Such a device also would remove the need to physically move the objective focus position, which would simplify and speed up acquisition. This would add to the instrument cost and complexity, however.

In this work we discussed an optical model which can simulate the scattering of

arbitrarily shaped particles, and showed how it might be used to measure the size of gold nanorods. We believe the same approach (using a rotating linear polarizer) is ready to be applied to BNPs as well. The aspect ratio of larger bullet-shaped or filamentous virions should be directly measurable. Additional future work may involve combining this simple technique with more advanced reconstruction methods to study more complexly shaped BNPs .

Chapter 3

Design & implementation of a high throughput gold nanorod detector

3.1 Motivation

As described in Section 1.3, microarrays remain useful in applications that require high multiplexing. While multiplexed PCR and barcoding techniques can simultaneously test for tens or hundreds of different RNA or DNA analytes, microarrays allow a single sample to be tested for thousands (or even tens of thousands) of different analytes at once.

SP-IRIS has previously been used to develop a sensitive and multiplexed microarray assay. Monroe and colleagues developed a test for allergy biomarkers with SP-IRIS, which used gold nanoparticles coated with antibodies to label individual captured biomarker proteins (Monroe et al., 2013). The gold nanoparticles within each microarray spot were counted in order to quantify the amount of each analyte. However, this approach had a major shortcoming related to multiplexing.

The instrument required a high numerical aperture (NA) and high magnification objective (at least 50x) to be able to detect the gold nanoparticles. This requirement greatly limits the field of view, such that only a single microarray spot will fit. To scan the array, motorized stages would therefore move the field of view from one spot to the next. Altogether, acquiring the images and moving the stages from position to position would take about one minute per spot. This made it impractical to use arrays

larger than 32 spots, which is 100-fold less than the size of average microarrays. This discrepancy in throughput nixes the primary advantage of the microarray format, and reduces the utility of SP-IRIS compared to conventional approaches.

The throughput could be recovered if particle visibility could be maintained while reducing the instrument magnification. Replacing the 50x objective with a 10x objective, for example, would increase the area of the field of view 25-fold. In fact, the throughput would increase by even more, because much of the field of view is wasted when imaging just a single spot at a time.

Unfortunately, single gold nanoparticles are not typically visible with a 10x, 0.3 NA objective—even with the enhancements we described in Chapter 2. As we shall discuss, this can be overcome by adjusting the amplitude of the reflected reference light.

3.2 The importance of amplitude: selective attenuation of reference light

As discussed in Chapter 2, SP-IRIS is a tightly-coupled interferometric detector where the reference light (i.e., the reflection from the chip surface) and the signal (i.e., light scattered by the particle) follow very similar paths to the detector. It is difficult to adjust the amplitude and phase of the reflected light without affecting the scattered light as well. In Chapter 2 we addressed the part of this problem related to phase. However, we did not address the problem of amplitude.

The visibility of a particle is determined by the relative amplitudes of the signal and reference. Recall from Chapter 2 that the normalized intensity (NI) of a nanoparticle is the ratio of the intensity of the combined scattered and reflected fields with

that of the reference field alone (i.e., the measured value when no particle is present):

$$\text{NIR} = \frac{|\mathbf{E}_{scat} + \mathbf{E}_{ref}|^2}{|\mathbf{E}_{ref}|^2}. \tag{3.1}$$

Note that if the reference is reduced to zero, then the normalized intensity blows up to infinity. One might think that since our goal is to increase the visibility of the particle, we should simply block the reference entirely and be done with it. However, this conclusion misses the importance of different types and sources of noise and variability.

All experimental measurements are made in the presence of certain random and nonrandom sources of variability or noise. One such source of variability in SP-IRIS is shot noise. Shot noise (also called photon noise or Poisson noise) is the variability inherent to all measurements of Poisson processes, such as the number of raindrops that fall into a bucket within 1 second, the number of photons that strike an illuminated detector within 10 ms, or the number of meteorite impacts on the moon within one square mile. These are all Poisson processes in that (a) they consist of discrete, independent occurrences, and (b) the average rate or separation between occurrences is constant.

Light is detected as a steady stream of photons, the arrival of which is a Poisson process. Consider a beam of intensity I striking a detector within a fixed exposure window t_0. On average, the number of photons which strikes the detector will be $n_0 = It_0$. If the measurement is performed multiple times, the number of detected photons will not be the same every time. Rather, one will observe a normal distribution with a mean of n_0 and a standard deviation of $\sigma(n_0) = \sqrt{n_0}$. This variability is the definition of shot noise. The signal to noise ratio (SNR) of any one measurement increases with the number of collected photons, and therefore the intensity and the exposure time

as well:

$$\mathrm{SNR}(t) = \frac{n}{\sqrt{n}} = \sqrt{n} = \sqrt{I}\sqrt{t}. \tag{3.2}$$

Shot noise effects interferometric sensing as well. The calculation for SNR in interferometric imaging is a bit more involved, so we save that discussion for Section 3.4.3. For now, it is enough to say that the SNR can always be improved by collecting more photons, just as in direct detection (Figure 3·1).

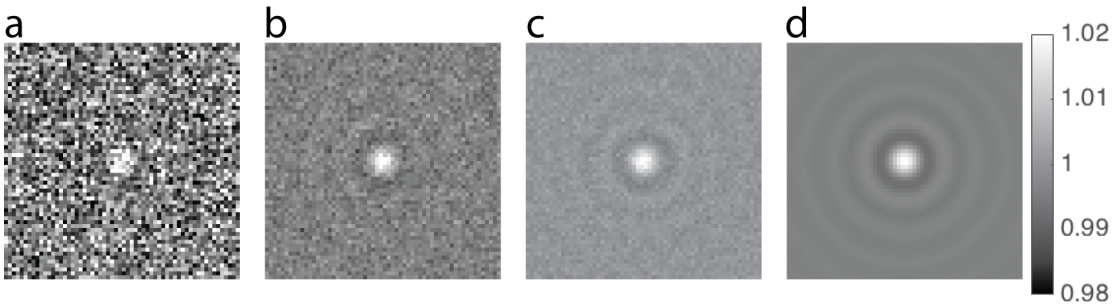

Figure 3·1: Demonstration of the effect of shot noise on image quality in SP-IRIS. Simulated images of normalized intensity of a nanoparticle, after collecting and averaging (a) 1 frame, (b) 16 frames, (c) 32 frames, and (d) infinite frames (i.e., no shot noise). The number of photons per frame is assumed to be 10,000.

A second source of random variability is stray light and camera read noise. These are grouped together because although they have different physical origins, they effect detection in the same way. Stray light includes all photons which reach the detector that did not come from the signal of interest. This includes light from outside the microscope (such as ambient light from the room) but is usually dominated by internal reflections and scattering from optical components of the microscope itself. Camera read noise includes all of the sources of thermal noise in the camera detector and amplifier electronics. Crucially, both of these sources of background have their own shot noise. If they are of similar amplitude to the signal then they will quickly reduce the measurement SNR. As we shall see in Section 3.4.3, stray light sets the limit on how small the reference intensity can be in SP-IRIS.

A third source of variability is the slight spatial variability in the reflectance of the IRIS chip. The SiO_2 film is extremely flat, but not perfectly so. Slight roughness across the chip surface causes slight variations in the reflectivity of the film. This is exacerbated when the chip is coated with capture molecules, since these molecules do not form a perfectly even monolayer. Altogether these effects cause the reflectivity of the surface to change by about 0.5-1% at best.

These background fluctuations set a limit on how visible a particle must be in order to be able to differentiate it from the background. If the normalized intensity of a particle is less than about 0.5-1% it will not be detected, regardless of the other sources of noise. This is the fundamental reason why the nanoparticles cannot be detected with a low NA objective—the reference field stays the same, but the amount of collected scattered light is reduced which lowers the normalized intensity below this threshold.

The visibility of a nanoparticle may be enhanced back again, if the reference light could be partially blocked (i.e. attenuated) without attenuating the scattered light. This requires some way to separate differentiate the scattered and reflected light beams. One method that was pursued was to utilize the fact that the reference beam and scattered beam take different paths from the chip to the detector. A microscope was built with a 4-f system in the collection path and a neutral density mask positioned in the Fourier plane of the image (Avci et al., 2017). The neutral density mask was patterned to mostly attenuate light in the center of the Fourier conjugate image, through which the reference beam travels. This method was able to demonstrate about 2-fold improvement in visibility, and has the advantages of working for any type of nanoparticle. However, it requires precise alignment and provides only modest visibility improvement.

3.3 Approach: Polarized illumination and gold nanorods

For applications where the nanoparticle is a part of the assay itself, the nanoparticle's optical properties may be designed together with the optical system. For these applications we developed a method which provides a much greater improvement in visibility (10-fold vs. 2-fold) than the Fourier masking method. This method utilizes rod-shaped gold nanoparticles (gold nanorods) for their polarization-dependent scattering properties.

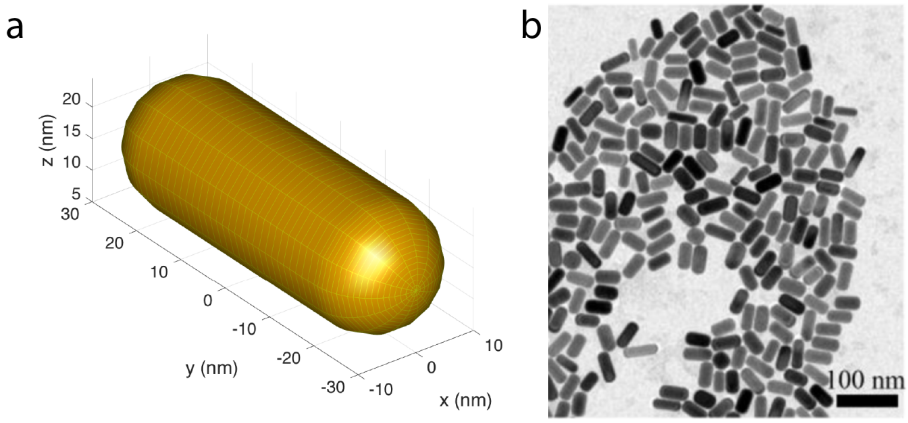

Figure 3·2: (a) Three dimensional mesh of a 25 by 60 nm gold nanorod particle used to simulate far field scattering. The rod is approximated as a cylinder with hemispherical caps on each end. (b) A transmission electron micrograph of a sample of gold nanorods (Li et al., 2016), showing the typical heterogeneity in size and aspect ratio.

Gold nanorods (GNRs, Figure 3·2) have the desirable property that their optical scattering is a strong function of polarization of the illumination. GNRs have two plasmon resonance wavelengths: a primary longitudinal plasmon which only scatters light that is polarized parallel to the longitudinal (major) axis of the rod, and a transverse plasmon which only scatters light polarized along the minor axes. At its longitudinal surface plasmon resonant wavelength, the magnitude of the scattered field may vary by a factor of 25 with the polarization direction of the illumination (Figure 3·3). Since only the longitudinal component of radiation is scattered by

the particle, the polarization state of the scattered light is usually different from the illumination unless the illumination happens to be precisely linearly polarized parallel to the particle.

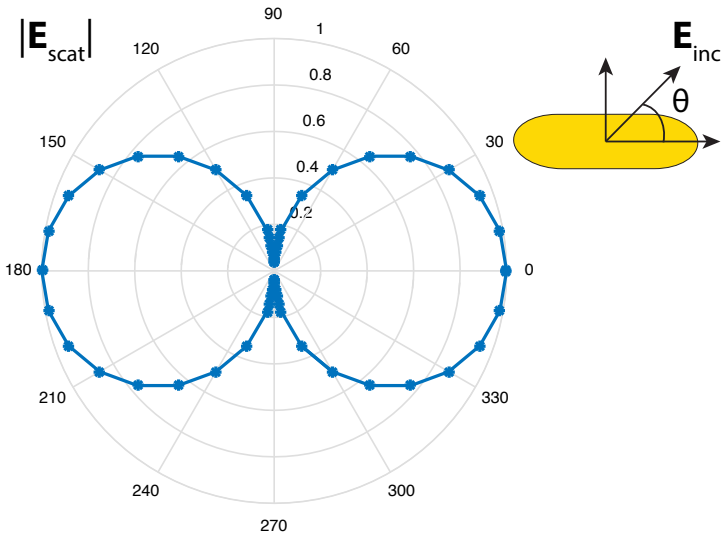

Figure 3·3: The amplitude of the scattered field $|\mathbf{E}_{sca}|$ from a gold nanorod varies with the polarization of the illumination $\mathbf{E}_{inc}$ much like a perfect dipole scatterer. Note that the scattered field is always polarized along the longitudinal axis of the particle, regardless of illumination polarization; essentially only the longitudinal component of the illumination is scattered by the particle. This is simulated data of a 25 by 60 nm nanorod at its longitudinal resonance ($\lambda_{LSPR} = 660$ nm), where $|\mathbf{E}_{sca}|$ is the amplitude of the scattered far field at the detector after being imaged with a 0.3 NA objective. The ratio between $|\mathbf{E}_{sca}(\theta = 0°)|$ (longitudinal excitation) and $|\mathbf{E}_{sca}(\theta = 90°)|$ (transverse excitation) is about 25.

On the other hand, the polarization vector of the reflected light is be the same as the illumination. In the next two sections, we describe two methods which exploit this difference in polarization between the scattered and reflected fields to selectively attenuate the reference light. We then evaluate and compare the performance of both of these designs with both simulations and experiments. Note that for both, the nanorods are assumed to be oriented randomly on the chip surface, as would be

typical in an assay.

3.3.1 Method 1: linear polarized illumination

The first method for enhancing visibility uses linear polarized illumination and a single linear polarizer in the collection path, which is oriented so as to block most of the reflected reference light (Figure 3·4). This configuration is advantageously simple, but has the significant disadvantage that the visibility of nanorods in the resulting image will depend strongly on their orientation. The excitation is of course nonuniform; nanorods oriented with their longitudinal axis parallel to the polarization of the illumination (0°) will scatter light strongly, while GNRs oriented at 90° will scatter very weakly. Furthermore, while nanorods at 0° will scatter strongly, their scattered field will be polarized in the same direction as the reflected reference, and will therefore be strongly attenuated by the second linear polarizer. Nanorods which are oriented at ±45° with respect to the illumination polarization are actually the most visible, since they are still excited relatively strongly (71%) yet their scattering also mostly passes through the collection polarizer (again 71%, Figure 3·5).

3.3.2 Method 2: circular polarized illumination

The second method for enhancing visibility uses circular polarized illumination, and a quarter wave plate and linear polarizer in the collection path that together block the majority of the reference light (Figure 3·6). This configuration requires more thoughtful optical design (as discussed shortly) but remedies the major shortcoming of the first method. With circular polarized illumination the excitation of each nanorod is the same regardless of its surface orientation (Figure 3·7). The scattered light from all nanorods is therefore equal in amplitude, with each field linearly polarized along the longitudinal axis of that particular particle. Since the collection optics are configured to (mostly) block circularly polarized light, they will not entirely block the

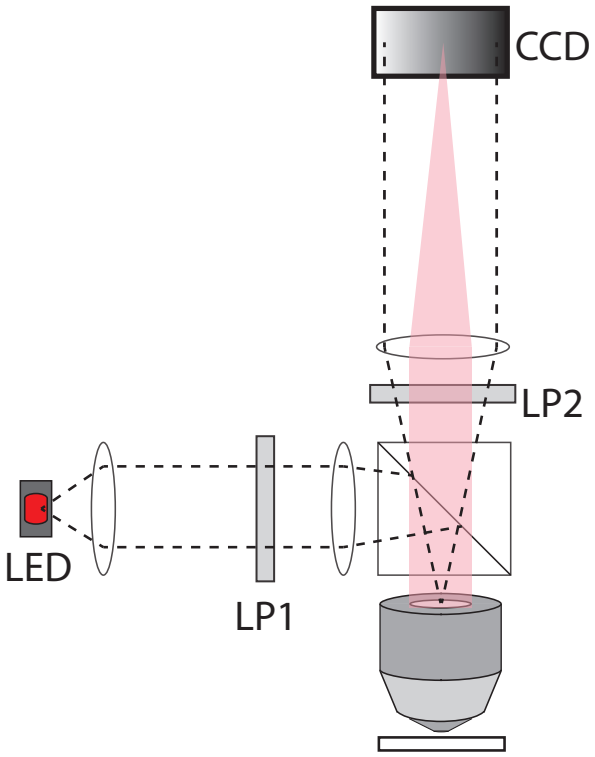

Figure 3·4: Schematic of setup for amplitude control utilizing linear polarized illumination. (LP1, LP2) are linear polarizers. The second linear polarizer is oriented so as to block most of the reflected reference light.

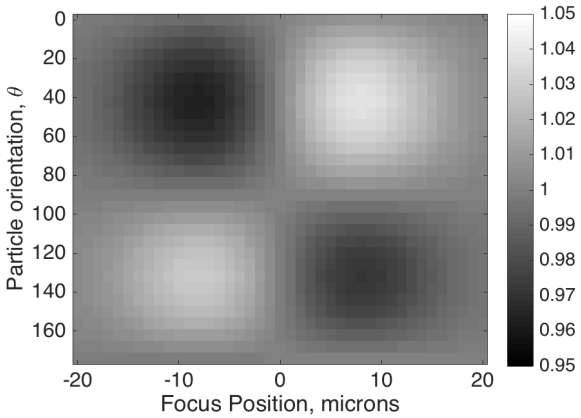

Figure 3·5: Simulations of the normalized intensity of nanorods in the linear polarized scheme at different surface orientations of the particle (y) and different focus positions of the microscope (x). The surface orientation angle θ is the angle between the illumination polarization and the rod longitudinal axis, as shown in Figure 3·3. Nanorods oriented at $\theta = 45°$ and 135° are the most visible while nanorods at 0° and 90° are not visible at all. Simulations are for 25 by 60 nm nanorods imaged with a 0.3 NA objective.

scattered light from any GNRs. Depending on the particle's orientation, the scattered light will be blocked by 29% to 50%. The phase delay imparted by the second quarter wave plate on the scattered field of a particle will depend on that particle's surface orientation, which changes the relative phase of the scattered and reflected fields at the detector. This shifts the fringes that are observed in the defocus profile, which results in the diagonal stripe pattern observed in Figure 3·8. The final result is that while not every nanoparticle will be visible in the same frame of the z-stack, every particle is visible in the final NIR image.

3.4 Results

3.4.1 Method selection

The circular polarization method had a key advantage over the linear polarization method, namely that all GNRs are detectable. The maps of normalized intensity

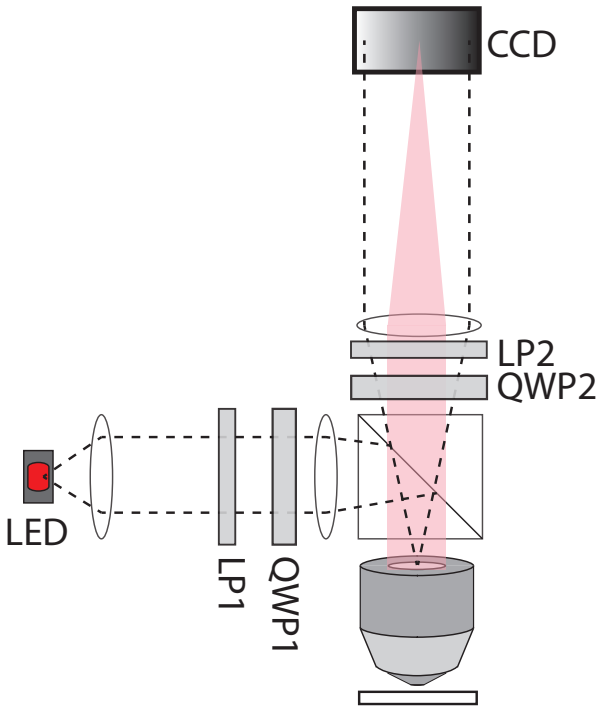

Figure 3·6: Schematic of setup for amplitude control utilizing circular polarized illumination. (LP1, LP2) are linear polarizers and (QWP1, QWP2 are quarter wave plates. LP1 and QWP1 together provide circularly polarized illumination, and LP2 and QWP2 are configured to block most of the reflected light which is also circularly polarized. The incident and reflected light beams are indicated with dotted lines, and the scattered light with red shadow.

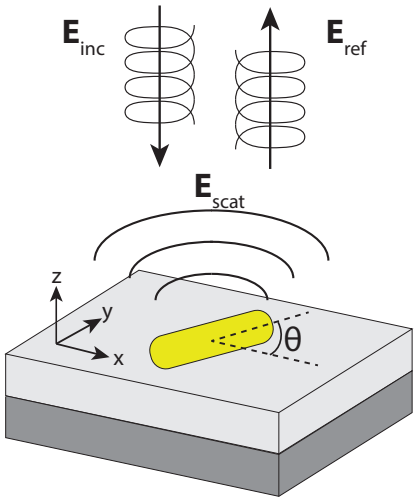

Figure 3·7: Schematic the three light fields in circular polarization enhancement of SP-IRIS. The incident field $\mathbf{E}_{inc}$ is approximately a circularly polarized plane wave, which is reflected by the substrate as a circularly polarized reflected reference field $\mathbf{E}_{ref}$. Light scattered by the particle $\mathbf{E}_{sca}$ is linearly polarized along the longitudinal axis of the nanorod.

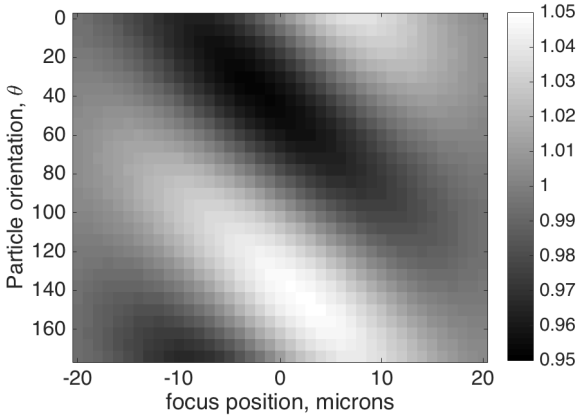

Figure 3·8: Simulations of the normalized intensity of nanorods in the circular polarized scheme at different surface orientations of the particle (y) and different focus positions of the microscope (x). The phase delay imparted by the quarter wave plate on the scattered field changes with particle orientation, causing the diagonal pattern. Simulations are for 25 by 60 nm nanorods imaged with a 0.3 NA objective.

at different focus positions (Figures 3·5 and 3·8) are helpful for understanding what is going on, but they are not suitable for direct comparison. Instead we can plot the normalized intensity range of GNRs at various orientations, as they would be measured using the two techniques (Figure 3·9). This makes it clear that the circular polarization method was indeed superior since it enhanced the visibility of GNRs at all angles, not just those at 45° and 135°.

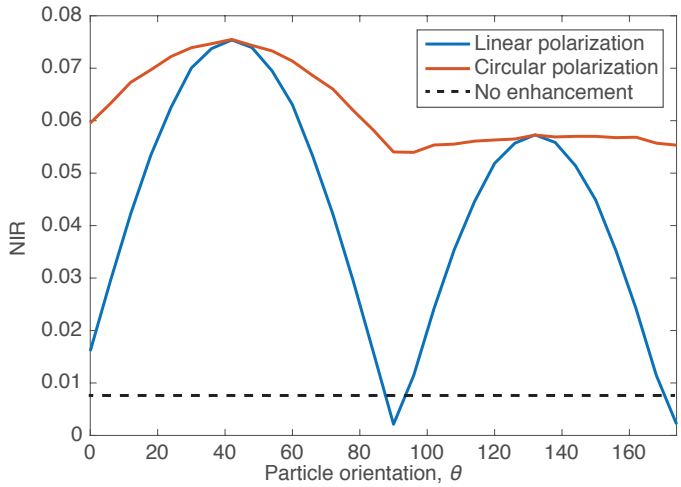

Figure 3·9: The Normalized intensity range (NIR) is simulated for nanorods with different surface orientations imaged with the linear polarization method, circular polarization method, or with no enhancement. The circular method enhances the visibility of nanorods at all orientations, while the linear scheme only enhances GNRs at 45° and 135°. The 'No enhancement' case is simulated as having circularly polarized illumination with no polarization optics in the collection path.

The linear polarization scheme had the practical advantage of being much easier to implement. As mentioned earlier, the circular polarization scheme required more thoughtful optical design. For one thing, it is not trivial to provide circular polarization illumination from an LED source across a large field of view. Since pellicle and plate beam splitters both have very different transmissions for S- and P-polarized beams, a cube beam splitter must be used. Furthermore, note in Figure 3·6 that

polarization optics in the collection path are placed in the 'infinity space' between the objective and tube lens. This is done instead of placing them immediately before the detector for several reasons: it avoids image vignetting, and avoids the problem of any dust/debris particles on the optics from being visible in the image. Unfortunately however, the reflected light beam (dotted lines) is therefore not collimated as it passes through the QWP. The phase retardation of a QWP depends on the light's angle of incidence. The result of this is that the extinction of the reference light near the center of the image will be maximal, but decrease farther from the center. This causes a substantial gradient in the final image which must be dealt with in post-processing. We found that this effect was somewhat reduced by using zero-order quarter wave plates made from a liquid crystal polymer that is designed to have stable performance over a much broader range of angle of incidence.

Altogether, the circular polarization method is certainly superior once implemented correctly. In the next section, we optimize the optical design to maximize the visibility of the nanorods using the circular polarization scheme.

3.4.2 Optimization of wavelength, nanorod and substrate

The GNRs, illumination wavelength and IRIS substrate are all parts of the optical sensor and were optimized together. We first decided to find the optimal illumination wavelength and oxide film thickness for the GNRs that we had on hand (Figure 3·10). We focused on the use case in which the signal would be the dimmest—namely, when the GNRs were immersed in water, as is done during real-time detection.

We had to keep in mind that the NIR still changes somewhat with the particle's surface orientation, even in the circular polarization method (Figure 3·9). Therefore, we used the BEM model to simulate the NIR of nanorods with different surface orientations when imaged by the circular polarization method, while sweeping the oxide thickness (Figure 3·11). As discussed in Chapter 2, the scattered field amplitude

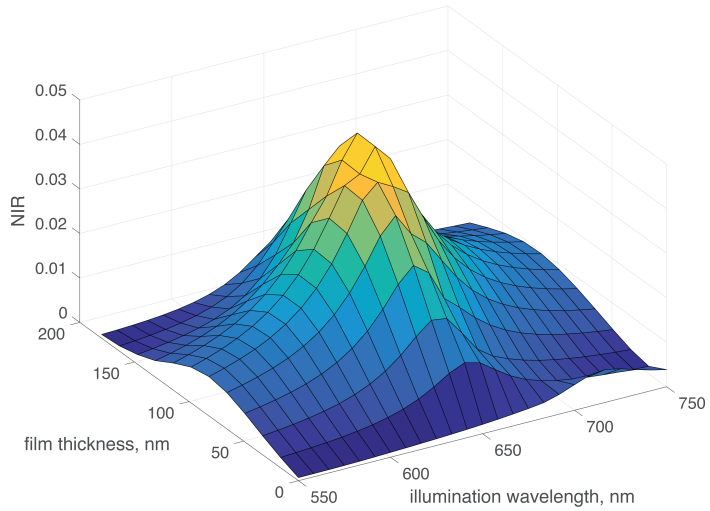

Figure 3·10: Simulations of the NIR of a GNR immersed in water, when the oxide film thickness and illumination wavelength are changed. The LSPR of the rod is at $\lambda_{LSPR} = 660\,\text{nm}$, which is also the optimum illumination wavelength. The optimum oxide thickness is about 110 nm.

is only approximated by the NIR signal measured by IRIS, so the phase of the fringes in the defocus profile are a source of variability here. We wished to ensure that we were using an oxide thickness that maximized the visibility of the *dimmest* GNRs, even if this was at the expense of the brightest ones. We found that 110 nm was optimal for the dimmest GNRs.

To experimentally characterize the performance of the circular polarization method we deposited a sparse sample of 25 nm by 71 nm nanorods ($\lambda_{LSPR} = 650\,\text{nm}$, Nanopartz$^{\text{TM}}$, Loveland CO) onto an IRIS substrate with a 100 nm oxide film by dropping 2 µl of 1 µM nanoparticles onto the chip surface and drying with nitrogen. We then imaged the dry substrate using 10x (0.3 NA), 20x (0.45 NA) and 50x (0.8 NA) microscope objectives. Virtually every nanorod visible under the 50x objective was also visible with the 20x and 10x objectives, with 1.5-fold and 3-fold reduced normalized intensity range, respectively (Figure 3·12). In all cases, the circular polarization setup was

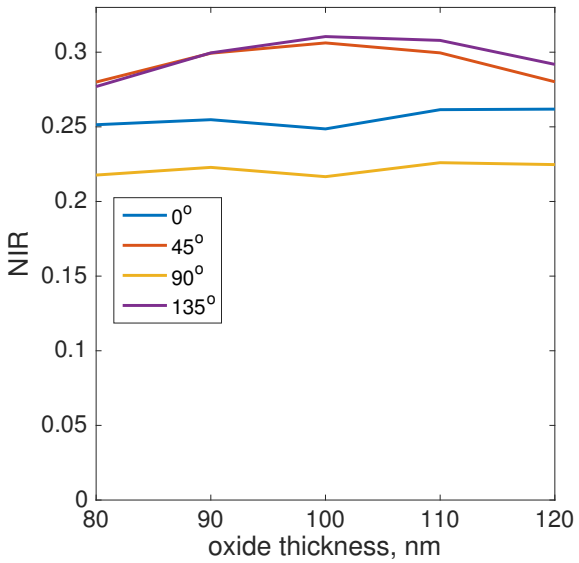

Figure 3·11: Simulations of the normalized intensity range (NIR) signal from nanorods imaged using the circular polarization method, as the oxide thickness is swept from 80 to 120 nm. Although 100 nm maximizes the NIR of the GNRs at 45° and 135°, 110 nm maximizes the NIR of the dimmer rods at 90°, so this was chosen as optimal.

configured to block approximately 99% of the reflected reference light, which provides an approximately 10-fold increase in NIR. Although all the GNRs in the 10x and 20x images were bright enough to detect, they of course have a much larger point spread function which causes nanoparticles which are too close to blur together and become indistinguishable.

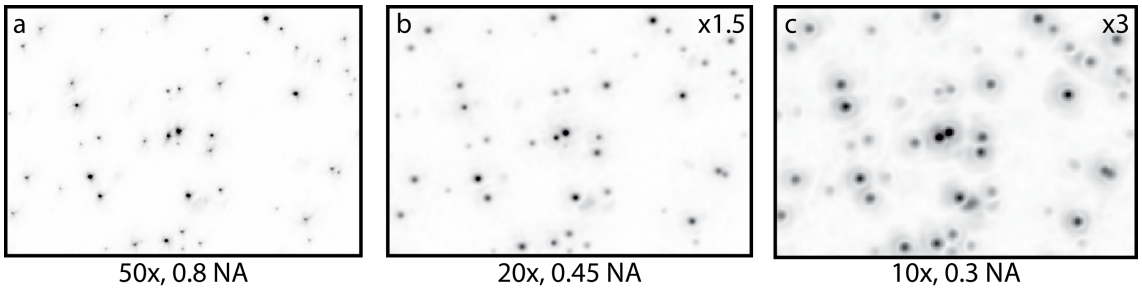

Figure 3·12: Cropped images of the normalized intensity range (NIR) of GNRs imaged with different magnification. All nanorods detectable using the 50x objective are also detectable using the 10x objective, although the point spread function is much larger. The NIR of (b) and (c) have been scaled by 1.5-fold and 3-fold, respectively. These cropped regions are 50 µm wide.

3.4.3 Performance limits of polarization enhanced SP-IRIS

As mentioned earlier, the smallest signal which can be detected using SP-IRIS is limited by surface roughness of the chip, which in practice acts as a normalized intensity cutoff. The polarization methods increase the normalized intensity by reducing the relative amplitude of the reference reflection. Eventually however, if the reference is reduced enough the sensor will be exposed to sources of low-light noise described earlier. The performance limit of polarization enhanced SP-IRIS is defined by these two different sources of variability: noise associated with low-light imaging (when the reference is not high enough), and the background roughness of the sensor (when the reference is too high).

In SP-IRIS, the shot noise of stray light turns out to be the strongest contributor

to low light variability. We experimentally determined that the main source of this stray light was from the beam splitter cube through a series of tests. We knew that the stray light must come from back reflections from the optics (since changing the ambient light had no effect) and the only place those back reflections could take place were in the beam splitter or within the microscope objective. To quantify the stray light, we placed a piece of black felt far away from the focus position to minimize the amount of light coming from the object plane, and acquired images both with and without the objective in place. Since the stray light was also partially circularly polarized, it was also being partially blocked during collection. To observe how it changed with extinction, we swept the linear polarizer in the collection path (LP2, Figure 3·6). We compared the intensity of these images to the intensity observed when imaging an IRIS chip, so we would know what percentage of the total amount of light during imaging could be attributed to stray light (Figure 3·13), and normalized all intensities by the intensity of the reflection when none of the reference is blocked (i.e., no attenuation). The amount of stray light both with and without the objective were about the same (red and green traces, respectively), indicating that the stray light was almost entirely from back reflections in the beam splitter. The two faces of the beam splitter which contribute to back reflections are the face opposite the illumination path and the face closest to the objective (i.e., right and bottom faces in Figure 3·6).

For design reasons discussed in the previous section, it is difficult to reduce these stray light reflections further. This beam splitter already has broadband anti-reflection (BBAR) coatings on all four sides, and it cannot be replaced with a pellicle (pellicles do not have back reflections). The effect of this stray light can be reduced by subtracting the 'dark' image we had measured from every frame acquired by the instrument. However, this is not the end of the story. Even after dark image subtrac-

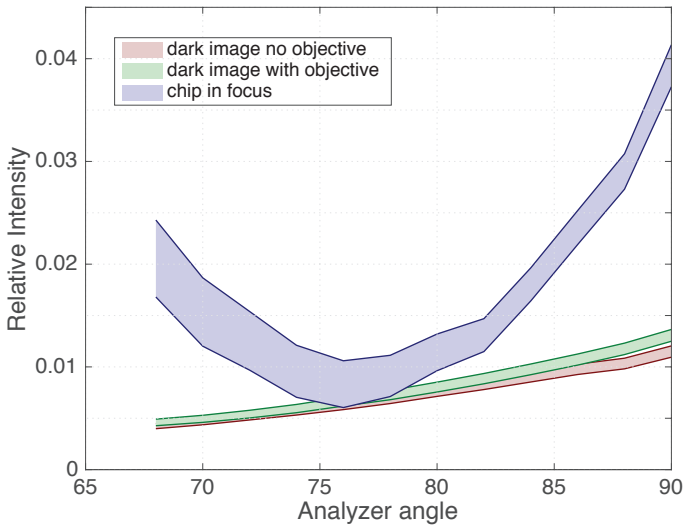

Figure 3·13: Experimental measurement of stray light in the circular polarization scheme. Images were taken at a range of analyzer angles (LP2, Figure 3·7). When a chip is in focus, maximum attenuation of the reference is obtained with the analyzer at about 76°. Dark images were obtained by replacing the chip with a piece of dark felt far from the focus position. Removing the objective did not significantly reduce the intensity, suggesting that most of the stray light was from back-reflections in the beam splitter cube.

tion, the stray light will still set the performance limit because the stray light also has shot noise. This additional shot noise can be a major problem because it increases the number of photons (and time) required to reach the necessary SNR.

To show explicitly how the SNR is effected by the shot noise of stray light, we can derive the formula for SNR for interferometric detection. As we mentioned before, shot noise is a bit more complicated in interferometric detection, because we must make two observations: one of the mixed signal and reference (I_+), and one of the reference alone (I_0):

$$\begin{aligned} I_+ &= \left(|\mathbf{E}_{scat}| + |\mathbf{E}_{ref}|\right)^2 && (3.3)\\ I_0 &= |\mathbf{E}_{ref}|^2 && (3.4)\\ I_s &= I_+ - I_0 = |\mathbf{E}_{scat}|^2 + 2|\mathbf{E}_{scat}||\mathbf{E}_{ref}|\cos(\phi) \approx 2|\mathbf{E}_{scat}||\mathbf{E}_{ref}|. && (3.5)\\ & && (3.6) \end{aligned}$$

Here are taking the phase term ($\cos(\phi)$) to be constant and the scattered intensity ($|\mathbf{E}_{scat}|^2$) to be negligibly small. Since we are making two observations, the total noise is the sum of both sources of shot noise.

$$\sigma_s = \sigma_+ + \sigma_0 = \sqrt{n_+} + \sqrt{n+0} \approx 2\sqrt{n_0} = 2\sqrt{I_0 t}. \quad (3.7)$$

Here n_+ and n_0 are the number of photons we measure within time t of I_+ and I_0, respectively, and t is time. We have again assumed for simplicity that the scattered amplitude is relatively small, so $I_+ \approx I_0$ and $n_+ \approx n_0$.

As an example, consider the SNR of a particle which has a NIR of 0.01 when imaged with SP-IRIS without any enhancement. Recall that the NIR is an approximate measurement of the signal I_s compared to the reference I_0:

$$\text{NIR} = \frac{I_s}{I_0} \approx \frac{2|\mathbf{E}_{scat}|}{|\mathbf{E}_{ref}|}. \quad (3.8)$$

If NIR is 0.01 then $I_s = (\text{NIR})\, I_0 = 0.01 I_0$. The SNR is therefore

$$\begin{aligned} \text{SNR}(t) &= \frac{n_s}{\sigma_s} = \frac{I_s t}{\sigma_s} && (3.9) \\ &\approx \frac{.01\,(I_0 t)}{2\sqrt{I_0 t}} = .005\sqrt{I_0 t}. && (3.10) \end{aligned}$$

This formula highlights a key similarity and a key difference between direct detection and interferometric detection (compare to Eq. 3.2. In both, the SNR increases with time: one can simply wait longer to collect enough photons. In interferometric detection however, there are *lots* of photons—the challenge is in detecting a small difference between two large measurements. As it turns out, however, the SNR from shot noise alone is identical for direct detection and interferometric detection. In Figure 3·14, SNR(t) for this case is plotted as a solid black line.

Now we are ready to consider the effect of some small amount of stray light on the SNR. Let's assume that the stray light has an intensity 1% of the reference reflection (this is similar to the experimentally measured values; Figure 3·13). Since we are good experimentalists we know to subtract the dark frame from the image before performing the measurement, so the signal stays the same as in the previous case ($n_s = I_s t$). However, the total shot noise is increased by the shot noise associated with the stray light, σ_{stray}.

$$\sigma_{stray} = \sqrt{n_{stray}} = \sqrt{0.01 n_0} = 0.1\sqrt{I_0 t}. \quad (3.11)$$

Therefore, the SNR for the system with stray light included is

$$\begin{aligned} \text{SNR}_{100\%}(t) &= \frac{n_s}{\sigma_s + \sigma_{stray}} = \frac{I_s t}{\sigma_s + \sigma_{stray}} && (3.12) \\ &\approx \frac{.01\,(I_0 t)}{2\sqrt{I_0 t} + 0.1\sqrt{I_0 t}} = .00476\sqrt{I_0 t}. && (3.13) \end{aligned}$$

The SNR is very slightly reduced, which makes sense because the amount of stray light is small (1%) compared to the two measurements I_+ and I_0. This is shown visually in Figure 3·14 ('100% Reference').

Now imagine that we are unsatisfied with a NIR of 0.01, since roughness in the images is of a similar magnitude, making these particles difficult to distinguish. We therefore employ an idealized enhancement technique which attenuates the reference light by 90% without attenuating of the scattered light or stray light at all. The new reference intensity is $I_{10\%} = 0.1I_0$. This boosts the NIR of the particles to 0.0316, making them easier to distinguish against the background. However, the stray light has not been attenuated.

$$\begin{aligned} \mathrm{SNR}_{10\%}(t) &= \frac{I_s t}{\sigma_s + \sigma_{stray}} \approx \frac{.0316\,(I_{10\%}t)}{2\sqrt{I_{10\%}t} + 0.1\sqrt{I_0 t}} && (3.14)\\ &= \frac{.0316\,(I_{10\%}t)}{2\sqrt{I_{10\%}t} + 0.1\sqrt{(10I_{10\%})\,t}} && (3.15)\\ &= .0136\sqrt{I_{10\%}t} = 0.0043\sqrt{I_0 t} = 0.90\ \mathrm{SNR}_{100\%}(t) && (3.16) \end{aligned}$$

Note that although the SNR per photon has increased by almost a factor of 3, the SNR per second has actually *decreased* because the reference intensity $I_{10\%}$ (i.e., the rate of photons) is so much smaller. Thus, the actual SNR from a shot noise standpoint is actually worse than without any enhancement at all ('10% Reference', Figure 3·14). This trend continues: if the reference is reduced by 99% in order to achieve a NIR of 0.1, the SNR is reduced by 30% ('1% Reference', Figure 3·14).

$$\begin{aligned} \mathrm{SNR}_{1\%}(t) &\approx \frac{.1\,(I_{1\%}t)}{2\sqrt{I_{1\%}t} + 0.1\sqrt{(100I_{1\%})\,t}} && (3.17)\\ &= .0333\sqrt{I_{1\%}t} = 0.00333\sqrt{I_0 t} = 0.70\ \mathrm{SNR}_{100\%}(t) && (3.18) \end{aligned}$$

The final result is that there are diminishing returns for attenuating the reference by more than is strictly necessary. The reference should only be reduced until the

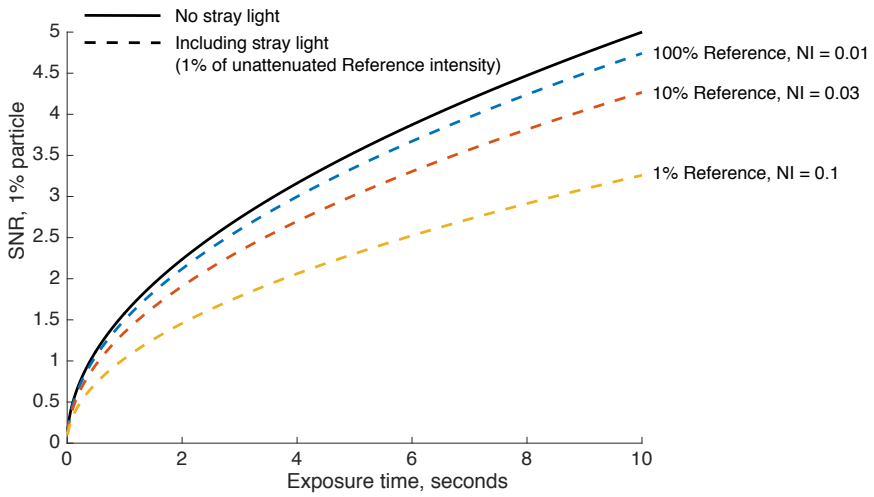

Figure 3·14: Signal to noise ratio (SNR) as a function of time is simulated for a hypothetical particle with varying amounts of reference attenuation, to show the effect of the shot noise of stray light. In the unattenuated case ('100% Reference') the particle has a normalized intensity (NI) of 0.01 (i.e., '1% particle'). Attenuating the reference by 90% ('10% Reference') or 99% ('1% Reference') increases the NI of the particle to 0.03 and 0.1, respectively. However, it also causes the shot noise of the stray light to reduce the SNR.

NIR is large enough that particles are visible against the surface roughness but not more, since the shot noise of stray light will degrade performance at an increasing rate. In practice, we found that 95% attenuation of the reference was sufficient to be able to consistently detect our nanorods nanorods with a 10x, 0.3 NA objective.

3.4.4 An estimate method to correct nanoparticle under-counting

If two or more nanoparticles are very close together on the IRIS chip, SP-IRIS may be able to detect them as a group, but not be able to tell that they are two distinct particles. This distance is defined by the diffraction-limited spatial resolution of the imaging system, and varies between about 300 nm to over 1 µm depending on the objective NA. Considering that nanoparticles are usually <100 nm in diameter, SP-IRIS images of nanoparticles may begin to appear crowded even if the physical surface packing of nanoparticles is sparse. Once there are so many nanoparticles that none can be distinguished, the total 'analog' absorbance or scattering of the spot can be used as the measured signal. But, between this regime and the digital regime is an awkward middle zone where many particles may be individually identified, yet a significant number are also overlapping in the image with their neighbors.

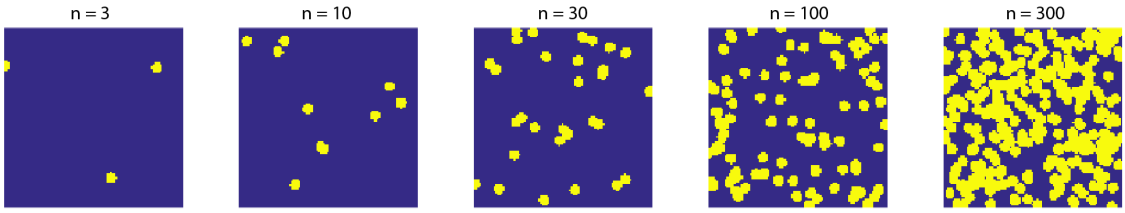

Figure 3·15: A toy model of particle crowding. In each case, n particles are placed in the image with uniform and independent probability, and are imaged as a uniform disk with no noise. Particles with overlapping disks will be detected as a single particle, resulting in false negatives (undetected particles). The total region is 100 x 100 pixels, and particles have a radius of 3 pixels.

This can be easily demonstrated by considering a toy model. Let us simulate

the image of a nanoparticle as a simple disk in a binary image with no noise, where the nanoparticle's image is 1 and the background is 0. As assume that the positions of bound nanoparticles are independent and have equal probability anywhere on the surface. Let us say that any number of particles whose images are touching are indistinguishable, and are detected as just one. As the number of particles increases, the average distance between neighboring particles decreases and the number of 'touching' particles grows, resulting in under-counting (Figure 3·15).

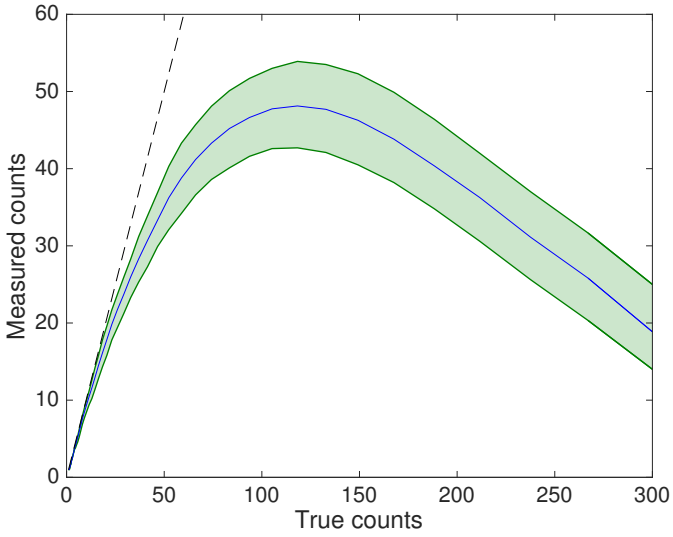

Figure 3·16: Simulation example of how under-counting (false negatives) increases with increasing particle counts. The upper and lower bounds of the shaded region are the 10th and 90th percentile of measured counts (n = 10,000 total simulations).

As the number and density of particles continues to increase until eventually, enough particles will crowd together that the total number of detected particles will actually start to go down (Figure 3·16). The average rate of false positives climbs alarmingly quickly, reaching 10% on average after just 16 particles , and 50% after 100 particles (Figure 3·17).

Particle crowding is more pronounced when a low magnification & low NA objec-

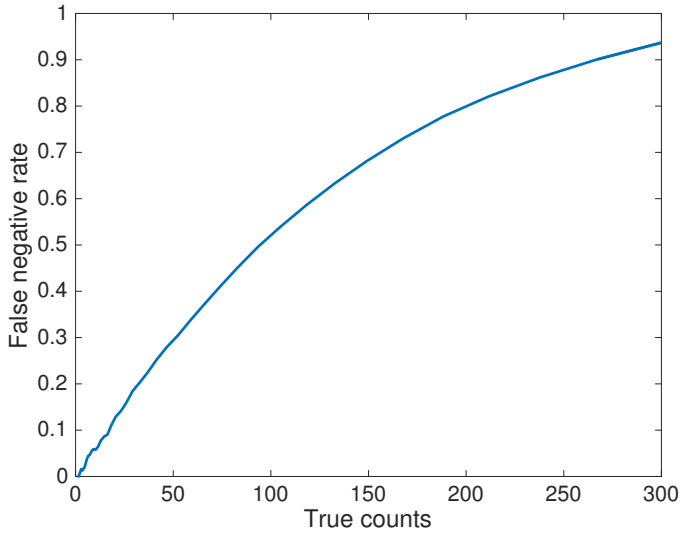

Figure 3·17: The rate of false negatives with increasing true particle counts for the toy model.

tive is used. Relative to the size of the microarray spot image, the diffraction-limited image of each particle fills a much larger area (an area about 6-fold larger, for 0.3 NA vs. 0.8 NA, for example). This of course limits the dynamic range by lowering the maximum number of particles that can be individually detected.

Perhaps one of the simplest ways to correct for this under-counting is to simply measure the discrepancy experimentally, and use it in reverse as a look up table (Figure 3·18). In this toy model, a look up table correction does not significantly reduce the false negative rate when the particles are sparse but is does reduce the average false negative rate for higher counts by about 2 to 3-fold on average (Figure 3·18b).

This method is computationally and conceptually simple, and easy to verify and implement. However, because there is significant variability in the number of measured counts in this simulated example, the corrected results are still often either 20% over- or under-estimations. Although this error rate is a property of the small scale of our model, there is clearly still room for improvement. This method also cannot be used in the regime where adding more particles actually lowers the measured number.

More sophisticated image processing of reducing under-counting such as peak finding, deconvolution and/or morphological opening could have significant utility.

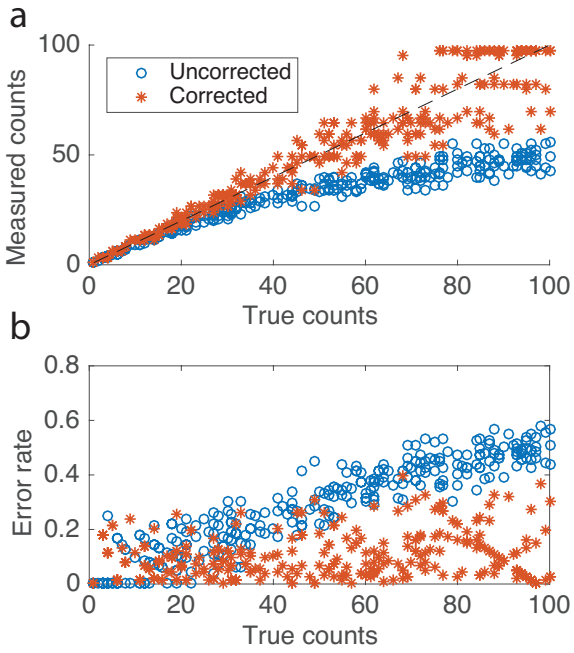

Figure 3·18: (a) Count estimate correction based on a look up table approach, using the same simulated scheme as before. The uncorrected counts are somewhat improved after being remapped based on the average false negative rate measured earlier (Figure 3·16). (b) The error rate is significantly reduced in many cases, especially at higher particle counts. Note that these errors are not just all false negatives but total errors (false negatives and false positives).

3.5 Conclusions

3.5.1 Summary

In this chapter, we have discussed the design and implementation of a high-throughput detector of single GNRs using SP-IRIS, for the purposes of developing the Digital microarray biosensor described in Chapter 4. We described all of the different sources of noise and variability in SP-IRIS, and described how selectively attenuating the reflected light would improve particle visibility and increase throughput. We described

two optical methods that combined plasmonic gold nanorods with polarization optics to accomplish this goal. We critically evaluated two methods with theory and simulations, and optimized the optical design of the superior method (which used circularly polarized light). We also showed how the experimental performance of this method was limited primarily by the shot noise of stray light and the reflectivity variations across the IRIS chip. Finally, we discussed ways to reduce under-counting of particles, which occurs when nanoparticles are so close together that their images begin to overlap.

3.5.2 Future work

Several areas of improvement remain in the domain of accurately counting the number of particles over a wide range of surface densities. First, the problem of accurately estimating the number of nanoparticles as density increases has not really been addressed to our satisfaction. We predict that much more accurate methods to reduce under-counting will help to improve quantification. Second, we have not yet discussed any actual algorithm to quantify the amount of bound nanoparticles when they are far too dense for any counting approach. The circular polarization scheme with the 10x objective saturates at less than 1,000 particles per microarray spot, yet the maximum number of GNRs that could fit within a single 100 µm microarray spot is likely over 2 million. An analog method of measuring total scattering from the spot, such as the simple 'scanometric' methods employed by others (Taton et al., 2000; Alhasan et al., 2012), would therefore have immediate and lasting utility since it would extend the dynamic range by up to an additional three orders of magnitude.

Chapter 4

The digital microarray: design and applications

4.1 Motivation

4.1.1 The shortcomings of the fluorescence microarray

Among all factors that contribute to the recent decline in rate of publications utilizing fluorescence microarrays, the advent of affordable next-generation sequencing (NGS) is surely the foremost. As described in Section 1.3, NGS has revolutionized transcriptomic analysis by enabling the full unbiased exploration of gene expression of a colony or even single cells (Treutlein et al., 2016). It has justifiably become the new gold standard over fluorescence microarrays in biological studies studies where the cost, time and complexity of the assay are secondary to accuracy and sensitivity. Indeed, mediocre sensitivity and dynamic range of fluorescence microarrays continue to be the technology's Achilles' Heel, and has led to a crisis in reproducibility of microarray data (Shi et al., 2006). This standard method of running replicate arrays to reduce measurement variability provides diminishing returns beyond a handful of replicates, so in practice the dynamic range of microarray studies is fixed to a few hundredfold (Wang et al., 2009).

Actually, closer inspection reveals that the underlying principle of the multiplexed microarray itself is ripe for improvement. The problem of limited sensitivity and dynamic range is a property of fluorescence reporting. A theoretically ideal transducer

could quantify the absolute number of immobilized targets with no background, and would be limited only by independent process statistics. Since a typical 100 µm diameter microarray spot each contains about one billion probe oligonucleotides (Ozkumur et al., 2009), this ideal transducer would itself have a dynamic range of about 100 million. By comparison, typical fluorescence scanners have a sensitivity about 10 000-fold lower, and provide only three logs of dynamic range (Figure 4·1). This enormous difference between theoretical limits and current performance leaves a lot of room for improvement.

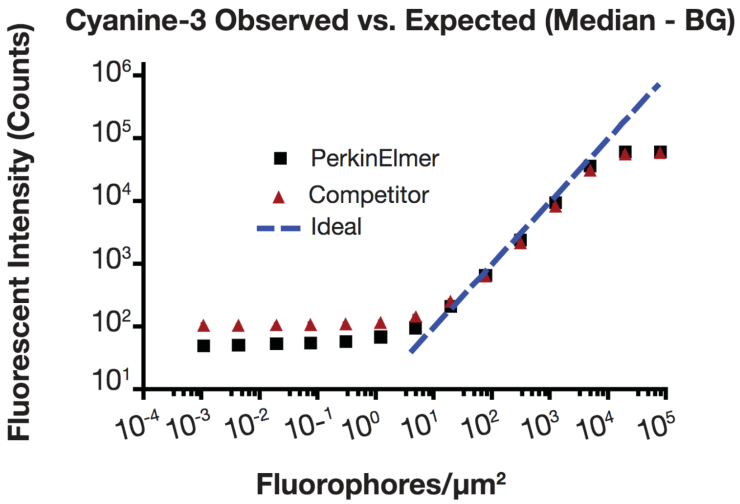

Figure 4·1: Standard calibration response for a PerkinElmer ScanArray G_X PLUS fluorescence reader, compared to an unnamed competitor. Calibration samples containing between 10^{-4} to 10^5 fluorophores per square micron were imaged with both scanners. Both scanners have a detection limit of around 10 fluorophores per square micron and provide about three logs of dynamic range (Risinger and Williams, 2006).

Attempts to enhance the sensitivity of fluorescence microarrays are physically limited by the number and rate of photons that can be collected from each fluorophore. Single fluorophores are routinely detected and localized in scientific research by using strongly focused excitation, high-NA collection, efficient photodetectors and a dark-field or epi-illumination optical configuration. However, when these concepts were

adapted to microarrays to enhance their sensitivity, the resulting systems were all physically limited in scanning speed and throughput by the fluorophore's quantum yield, emission rate and photostability. The application of faster and more stable fluorophores such as semiconductor nanoparticles (i.e. quantum dots) has also been explored, but with similar outcomes (Liang et al., 2005; Li et al., 2011).

4.1.2 The advantage of light scattering

Light scattering is entirely unlike fluorescence in several key aspects—there is no saturated emission rate and no photobleaching. The speed and throughput of techniques for detecting the scattering or absorption of single nanoparticles tend therefore to be limited only by the maximum allowable local heating of the particle due to dissipation of absorbed optical power. The use of nanoparticles as scattering labels on a microarray has been previously explored, either for ensemble ('total scattering') or single-particle measurements, and readout sensitivity is improved by many orders of magnitude in all cases (Monroe et al., 2013; Patskovsky and Meunier, 2015; Alhasan et al., 2012). However, because nanoparticle light scattering is very weak for particles smaller than 100 nm these studies still required either high-magnification microscope objectives to detect individual particles or subsequent 'growth' steps, in which silver is reduced onto nanoparticles in order to increase their size and scattering cross section. This silver deposition is necessary in order to detect a very small number of nanoparticles, but it doesn't provide digital detection of *individual* nanoparticles. Furthermore it does not provide nearly the potential dynamic range of the microarray format because the silver reduction is a nonlinear feed-forward process—the amount of reduction required for 1 femtomolar detection, for example, saturates signals larger than 1 picomolar (Alhasan et al., 2012).

4.1.3 A rapid antimicrobial susceptibility test based on gene expression

In developing the first digital microarray assay, we wished to select an application for which this technology held significant potential. We chose to select a problem of very high national and global importance since the potential impact of a technology depends on the scope of the challenge as well as the technique's suitability. This challenge is the growing crisis of antimicrobial resistance.

For the last few decades, the prevalence of drug-resistant infections have steadily increased while the rate of development of new antimicrobial drugs has drastically slowed (Luepke et al., 2017). Consequently, last-line drugs have been pushed into service with increasing frequency, leading to the proliferation of multi-drug resistant strains especially in hospital settings (Morency-Potvin et al., 2017; Yu et al., 2014). Drug resistant strains have proliferated exponentially in the last three decades, have an are a significant health risk for hospitalized patients (Tong et al., 2015; Dancer, 2014).

For these reasons, doctors are obliged to act quickly in response to infections in hospitalized patients. They are likely to prescribe antibiotics immediately because of the value of early treatment, even if there is a high probability that their 'first guess' will not work. They will often simultaneously perform an antimicrobial susceptibility test (AST), in which the infectious bacteria is isolated and cultured. This culture may then be identified through various means, or tested for its susceptibility to a panel of different antibiotics. The most common method involves incubating the infectious agents with an antibiotic to measure the minimum inhibitory concentration (MIC) that will halt growth. If an antibiotic has a high MIC it is likely that the infection itself is or will quickly become resistant.

Although the inhibition MIC assay is the gold standard method of AST in terms of accuracy, it is too often ineffective since the tests usually take two or more days to

yield a result. In the interim, the patient often either starts to respond to the first line drug (so the test's results are no longer important), or does not, and all the while the infection has been spreading. Modern medicine is still awaiting a feasible rapid or same-day AST, that could provide information for the doctor fast enough to help with the first treatment decision.

Towards this end, a variety of alternative techniques have been investigated. Since the replication rate of the bacteria is the the major limiting factor of assay time, many have looked for markers correlated with growth which may be observed earlier, such as perturbed metabolism, increased oxidative stress or altered gene expression (Lee et al., 2010; Wei Hou et al., 2015). Strain-specific stains have also been investigated (Ho et al., 2012). Barczak and colleagues published compelling evidence that the gene expression response of drug-resistant and -susceptible strains of *Escherichia coli*, *Pseudomonas aeruginosa*, and *Klebsiella pneumoniae* to antibiotic exposure are sufficiently different that they could be used to identify the strains without growth (Barczak et al., 2012). They identified a panel of mRNAs that were consistently either highly up-regulated, highly down-regulated or unchanged in the resistant strain with respect to the susceptible strain, just 30 minutes after the bacteria was challenged with an antibiotic.

This result suggested that a rapid AST could be performed by (a) isolating the bacteria from the infection and then (b) immediately challenging the culture with an antibiotic, followed by (c) quantifying expression of the biomarker mRNAs they had identified. Hou and colleagues were able to show that steps (a) and (b) were feasible even with a very small number of infecting cells (Wei Hou et al., 2015). However, step (c) remained challenging due to the low number of cells (and therefore low mRNA copy numbers).

Hou and colleagues used the Nanostring N-Counter® multiplexed barcode system

to achieve high sensitivity and multiplexing. The N-Counter system is well suited for biological research, but the test is a complex multi-step process which makes it unsuitable for a rapid AST application. Primarily the test is too slow: the test requires an overnight hybridization step and provides the final results on the afternoon of the second day after starting the test.

A rapid AST based on gene expression profiling of a small number of cells requires same-day quantitative detection of tens to hundreds of different transcripts with very high sensitivity. It turns out that this set of requirements matches closely with the specifications of the digital microarray instrument, since it should be able to quantify dozens of different targets at concentrations down to 1 femtomolar, and should be able to provide results in as little as two hours.

4.2 Assay design and optimization

This section focuses on the design and optimization of the mRNA resistance biomarker assay. We break this discussion into three sequential parts: microarray probe design, assay scheme selection and optimization of hybridization conditions.

Before we go any further, let us define three key terms which are used throughout this section to discuss assay performance: sensitivity, specificity, and dynamic range. In this context, sensitivity is defined as the response in the measured signal (in our case, nanoparticle counts) with respect to a change in target concentration. It is analogous to the slope of the standard curve, as in Figure 4·1. Specificity (also called selectivity), on the other hand, is concerned with minimizing the signal when there is no target present (i.e., reducing false positives). Finally, dynamic range is concerned with the range of target concentrations which can be quantifiably measured (i.e., the ratio between the highest concentration that can be detected and the lowest concentration which saturates the sensor).

In each of the following sections, the objective is to maximize sensitivity, specificity and dynamic range. In the first section (DNA probe design) We describe the steps involved in selecting the DNA 'probe molecules' that bind to each target molecule and label it with a gold nanorod (GNR). In the second section (scheme selection) We discuss the effect of the order in which the different assay components are mixed together, which turns out to be very significant. We compare two different schemes using both theory and experiment. In the final section We discuss relatively minor tweaks and optimizations to the assay buffer and surface polymer coating which greatly improved sensitivity and specificity.

4.2.1 DNA probe design

Digital microarrays use the common 'sandwich' assay scheme, which is commonly used in other microarrays, enzyme-linked immunosorbent assays (ELISA) and other formats. The sandwich assay scheme requires two molecules to be carefully selected which will both be able to bind to the target analyte with high affinity *at the same time*. Ideally, if the analyte is present in solution, these two probe molecules will complex with it to form the two bread slices of a molecular 'sandwich', with a single analyte molecule in the middle between them. Once suitable probe molecules have been identified, one of the two probes must be fixed to the sensor substrate. This probe is often called the 'capture' probe because its role is to capture the analyte and immobilize it on the surface. The other probe is usually 'functionalized' by covalently linking it to some type of molecular transducer such as a fluorescent molecule or active enzyme, which can be detected by some sort of instrumentation such as an optical or electrochemical reader (in our case, this reporter will be a gold nanoparticle). This functionalized probe is often called the 'reporter'. When the capture probe, analyte and reporter probe are all present, a number of molecular 'sandwiches' are formed on the substrate. Provided that the capture and reporter probes are in excess

with respect to the target, the number of sandwiches will be proportional to the concentration of the analyte.

If the analyte is a protein then both the capture probe and reporter are often antibodies, specific peptides, or aptamers. If the analyte is a single stranded nucleic acid such as RNA the capture and reporter probes are usually DNA oligonucleotides (oligos) that are synthesized to be complementary to two adjacent loci on the nucleic acid. The location of these probe-complementary sites is an important design consideration for nucleic acid microarrays. For one thing, the nucleic acid sequence of the site must be sufficiently different from all other potential nucleic acids in order to maximize specificity. Furthermore, most mRNAs are thousands of base pairs long and can form secondary structures, so the effective affinity of a given site for the probe sequence may depend on the native conformation of the rest of the molecule. The probes themselves must not have any favored secondary structure such as hairpins since they can reduce the affinity and/or rate of duplex formation.

Another practical consideration is that conjugating DNAs to gold nanoparticles (including gold nanorods) can be a difficult and time consuming process. To reduce the amount of time and reagents spent on performing multiple conjugations we decided to use a 'universal' labeling scheme (Figure 4·2). The nanoparticle is functionalized with a universal label sequence which will bind to a complementary region on every reporter probe. This allows the same stock of conjugated nanoparticles to be used for multiple different nucleic acid assays for different applications.

Capture probe stabilization improves sensitivity

In Figure 4·2, we have included a short 'stabilizer' oligo that is complementary to the 5' end of the capture probe nearest to the substrate. The role of this sequence is to form a region of double stranded DNA (dsDNA) between the surface and the target-complementary 'capture region'. This dsDNA region increases the affinity of

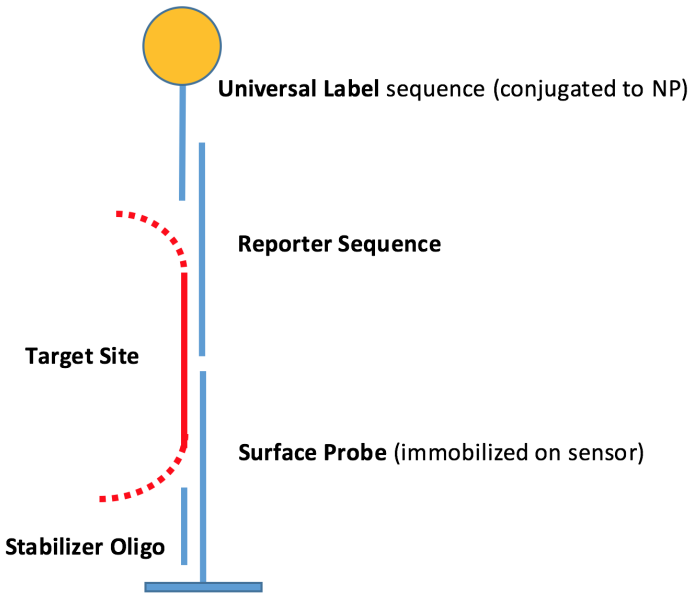

Figure 4·2: Schematic of the probe design for mRNA expression profiling. The capture probe and reporter probe are each complementary to the target sequence at adjacent 25 base pair sites. The 5' end of the capture probe is functionalized with an amino group which covalently bonds to the polymer substrate coating, and is 37 base pairs altogether. The 12 base pairs at the 5' end (closest to the chip surface) form a duplex with a stabilizer sequence.

the capture probe for the target molecule in multiple ways. First, the flexibility of a dsDNA double helix is much less than single stranded DNA: the persistence length of dsDNA is about one hundred times greater than that of ssDNA (45 nm vs 0.4 nm) (Tinland et al., 1997). As we discuss later, duplex formation has a relatively large entropic penalty since both strands lose a large amount of conformational degrees of freedom. An adjacent region of dsDNA 'fixes' one end of the segment and therefore reduces this penalty, thereby increasing the overall free energy of binding and catalyzing duplex formation. Second, the rigid dsDNA segment may have the effect of extending the capture region a bit farther out from the sensor surface and perhaps increase its activity by reducing nonspecific interactions of the capture region with the substrate itself..

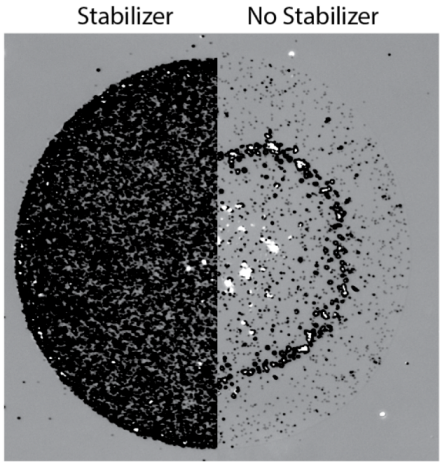

Figure 4·3: The results of an early experiment qualitatively demonstrate the sensitivity improvement afforded by using a stabilizer sequence on the capture probe. This is a composite image showing half each of two microarray spots. Each spot is the same capture probe but on different chips. Both chips were incubated with the same concentration of the target sequence and reporters, but the chip on the left was incubated with 1 µM stabilizer sequences before target incubation, and shows perhaps 50-fold increase in the number of nanoparticles.

In an early test to evaluate the effect of stabilization on sensitivity, we incubated one of two otherwise identical microarray chips with 1 µM stabilizing sequences for

30 minutes before conducting an identical assay with both chips. The chip which had been incubated with stabilizing sequences before the assay had a much higher number of bound nanoparticles (Figure 4·3). Later, experiments reaffirmed that stabilization greatly improves affinity (Figure 4·9).

Probe sequence and target selection for mRNA expression based AST

As mentioned earlier, Barczak and colleagues had identified a panel of mRNAs that are strongly up- or down-regulated in resistant strains of *E. coli* compared with susceptible strains, following antibiotic exposure (Barczak et al., 2012). Based on their work we selected four genes expressed by *E. coli* as the biomarkers for our assay (Table 4.1).

We predicted that a 25 base pair duplex between the target and each the reporter and capture probe would provide sufficient affinity and specificity for the assay based on the design of other similar microarray assays (Galbiati et al., 2013). We searched each of the four transcripts for a specific 50 base pair target site using the online PCR primer design tool Primer3Plus (Untergasser et al., 2007). The recommended primers (i.e., probe sequences) were aligned to the MG1655 *E. coli* strain using the NCBI online BLASTn tool (Madden, 2003). If the probes had no nonspecific matches larger than 10 base pairs, they were inspected for secondary structures using the modeling software UNAfold. Any surface probe which had stable secondary structures at high ionic concentrations (300 Na^+) such as hairpins were rejected.

Based on similar microarray assays, the length of the universal label-reporter duplex was selected to be 18 base pairs long. Candidate sequences were generated randomly, and both senses were aligned with the MG1655 genome as before. To minimize cross reactivity and nonspecific interactions, sequences with more than 5 base pair overlap with the surface probes were rejected as well. A short 5-A spacer was added to the label sequences between the 5' thiol functional group and the reporter-

Gene	Target site
murC	CATACATTTTGTCGGCATTGGTGGT**GCCGGTATGGGCGGTATTGCCGAAG**
recA	GCGTAAAAGAGAAGCTGATCGAGAA**AGCAGGCGCGTGGTACAGCTACAAA**
dinD	TATCCAGACCCGACGGCAGGAGCTT**GCTGACGATGAAGCATTTAAGCAAC**
putP	TAGTATGACCTGGATGATCCTCTGC**CTGGCAGGGGCGGTGGCTGTCGGCT**

Table 4.1: Description of final target sites on *E. coli* mRNA transcripts (ABX, antibiotics). The portion complementary to the reporter probe is underlined, and the portion complementary to the capture probe is bold. Sequences are written 5'-3'.

Gene	Capture probe
murC	/5AmMc6/ GGGAAAAAAGGG**CTTCGGCAATACCGCCCATACCGGC**
recA	/5AmMc6/ GGGAAAAAAGGG**TTTGTAGCTGTACCACGCGCCTGCT**
dinD	/5AmMc6/ GGGAAAAAAGGG**GTTGCTTAAATGCTTCATCGTCAGC**
putP	/5AmMc6/ GGGAAAAAAGGG**AGCCGACAGCCACCGCCCCTGCCAG**

Table 4.2: Capture probe sequences designed for *E. coli* mRNA expression profiling. Sequences are written 5'-3'. All probes have an amino functionalized 5' end. The portion complementary to the target site is bold.

complement site, based on some evidence that longer probes have improved sensitivity for

Preparation of DNA-gold nanorod conjugates

Linking of the universal label oligo to gold nanoparticles is a key step. We developed a custom protocol for gold nanorod conjugation based on the salt aging method (Hill and Mirkin, 2006) and the fast acid methods (Belosludtsev et al., 2001). These methods were developed for conjugating smaller gold spherical nanoparticles, although

Gene	Reporter probe
murC	ACCACCAATGCCGACAAAATGTATG CTGAGTCCGAGGATTGAG
recA	TTCTCGATCAGCTTCTCTTTTACGC CTGAGTCCGAGGATTGAG
dinD	AAGCTCCTGCCGTCGGGTCTGGATA CTGAGTCCGAGGATTGAG
putP	GCAGAGGATCATCCAGGTCATACTA CTGAGTCCGAGGATTGAG

Table 4.3: Reporter probes designed for *E. coli* mRNA expression profiling. Sequences are written 5'-3'. The 25-bp portion complementary to the target site is bold. The 18-bp portion is complementary to the universal label.

Name	Sequence
Stabilizer Oligo	CCCTTTTTCCC
Universal Label	/5ThioMC6-D/ AAAAACTCAATCCTCGGACTCAG

Table 4.4: Accessory oligos designed for expression profiling. The universal label has a thiol functionalized 5' end for conjugation to GNRs, and a 5A spacer.

there are also results of conjugating larger spherical nanoparticles in literature (Hurst et al., 2006). In our experience, we found that both the salt aging method and fast acid had poor yield, resulting in a final volume of conjugated nanorods only 10%-25% of the starting volume. We found that most of the loss was incurred during centrifugation, as nanoparticles would adhere to the side of the plastic disposable micro-centrifuge tubes. The addition of Tween-20 in low amounts (.01% w/v) to the sample immediately before centrifugation consistently improved yield to above 80%.

4.2.2 Assay scheme selection

In the previous section, we assembled all of the molecular pieces for our mRNA AST assay. Hopefully, the probe sequences will form little molecular sandwiches on the sensor with very high sensitivity and specificity for the target. However the performance of the probe molecules is only one aspect in the final performance of the sensor. Even if our molecular probes are biochemically ideal (i.e., they have an infinite association constant and perfect specificity) and our transducer is also ideal (i.e., we perfectly detect every single bound nanoparticle with no variability or noise), the sensitivity and speed of the assay will still be limited by mass transport limits of the different molecular components (including the target molecules themselves). Mass transport processes are those which are responsible for physically moving all of the different molecular components to the sensor surface, so that binding may occur. The two processes which govern molecular motion for digital microarrays are convection and diffusion.

For this reason, the 'order of assembly' of the molecular components of the assay will effect on assay performance. Consider the following two assay schemes (Figure 4·4). In the first scheme, we incubate the sample solution containing the target molecules with the sensor chip for some duration of time. After this the sample solution is washed away, and some number of target molecules remain immobilized by the capture probes. Then, a second incubation is performed with a solution that contains a high concentration of reporter probes and functionalized GNRs. The GNRs will then bind to any target molecules immobilized on the substrate. The excess reporters and GNRs are then washed away, and the chip is dried and imaged. Let us call this scheme the 'heterogeneous' approach (the name will be explained shortly).

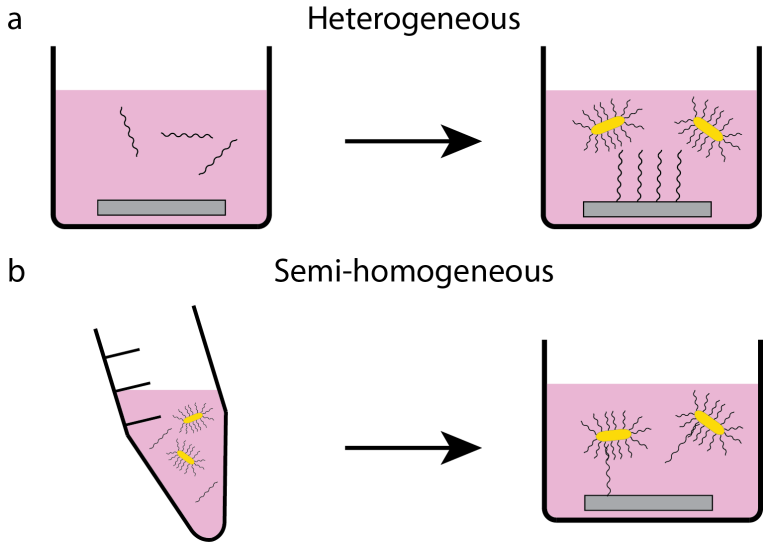

Figure 4·4: Comparison of possible assay schemes. (a) In the heterogeneous scheme, the chip is first incubated with the sample solution, then washed, then incubated with a concentrated solution of GNRs. (b) In the semi-homogeneous scheme, the sample solution is first mixed with a solution containing GNRs and allowed to reach equilibrium. Then, the mixed solution is incubated with the chip.

A second approach would be to first mix a solution of concentrated GNRs with the target solution, and allow them to reach equilibrium. We could prepare the GNRs ahead of time to have the reporters already hybridized. Provided that the

concentration of the GNRs greatly exceeds the total concentration of all targets in solution, at equilibrium we would expect each target nucleic acid to have hybridized to a different GNR. Once this solution has reached equilibrium, it can be incubated with the chip directly. The GNRs alternatively be concentrated via centrifugation and buffer exchange before incubation, if desired. Let us call this second scheme the 'semi-homogeneous' approach.

The names 'heterogeneous' and 'semi-homogeneous' are derived from terminology in chemical catalysis. Heterogeneous catalysis takes place when the substrate and the catalyst have different phases, such as a catalytic converter in a modern car where the substrates are vaporized hydrocarbons in the car exhaust and the catalyst is a solid platinum surface. In heterogeneous reactions, one of the two molecules is responsible making its way to the other, which is relatively immobile. In a homogeneous reaction, both molecules are in the same phase and mixed together. The burden of movement is shared between the two species. Homogeneous reactions tend to be less limited by mass transport. The first assay scheme we introduced consists of two heterogeneous reactions (first between the surface and the target solution, then the surface and the GNRs). In contrast, the second scheme consists of one homogeneous reaction and one heterogeneous reaction, hence the name semi-homogeneous (Figure 4·5).

4.2.3 Convection, diffusion and the mass transport limit

In this section, we discuss the role of diffusion and convection in the performance of a microarray sensor. We are interested in the rate at which target molecules make their way down to the correct microarray spot to be captured. We will focus in this section on what turns out to be the best-case scenario: a semi-homogeneous assay in which the second incubation is performed in a microfluidic flow cell (we describe the design of the flow cell in Chapter 5). As we shall see, convection and diffusion set a theoretical upper limit on sensitivity because the IRIS chip is a solid-phase sensor.

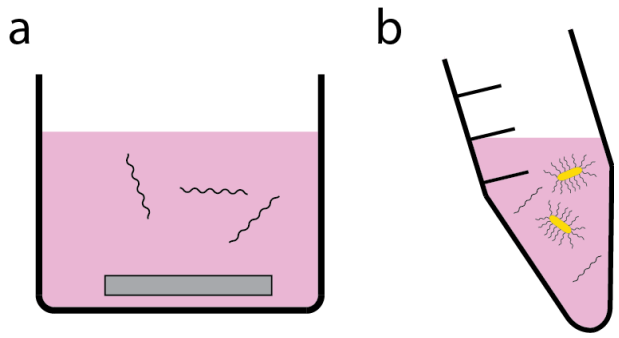

Figure 4·5: Comparison of heterogeneous and homogeneous reactions (a) In a heterogeneous reaction, the target molecule and the capture probe have different physical phases. Here, the target is in solution (liquid phase) while the capture probe is immobilized on the substrate (solid phase). (b) A homogeneous reaction is one in which both the target and reporter probe (the GNR) are mixed together.

Much of the analysis in this section is elegantly discussed by Squires, et al (Squires et al., 2008), which is highly recommended to the interested reader.

Fluids are characterized by constant motion at the molecular scale. Individual molecules within a liquid or gas are not bound to their molecular neighbors (as in a solid) but are free to slide and bounce past one another. All atoms (and molecules) undergo thermal motion and have kinetic energy: this thermal kinetic energy is proportional to the system temperature. Indeed, the temperature of a solution is defined as the average kinetic energy of all constituent molecules. The kinetic energy of any single molecule is not constant in time, since it exchanges energy with other molecules through constant collision. Collisions are very frequent in liquids, so at equilibrium the average temperature of the solution is also the average temperature of each of its constituent molecules.

The diffusion coefficient D of a particular particle (a molecule or nanoparticle) is a measure of the average rate at which that particle will traverse away from its

starting point due to thermal motion. It is defined by the Stokes-Einstein equation:

$$D = \frac{k_B T}{6\pi\nu r} \tag{4.1}$$

where k_B is the Boltzmann Constant, T is temperature, ν is the dynamic viscosity of the medium and r is the particle's hydrodynamic radius. Essentially, the diffusion coefficient is the ratio between a particle's average kinetic energy ($k_B T$) and the drag imposed by the solution on the particle based on its size. For example, a spherical particle with a hydrodynamic radius of $r = 50\,\text{nm}$ at room temperature in water would have a diffusion coefficient of about $D \approx 10\,\mu\text{m}\,\text{s}^{-1}$. This is actually similar to that of single stranded nucleic acids and RNA, have a diffusion coefficient between 1-10 $\mu\text{m}^2\,\text{s}^{-1}$ (for short 20 base pair fragments) and 0.1 $\mu\text{m}^2\,\text{s}^{-1}$ (for longer fragments up to 1,000 base pairs) (Nkodo et al., 2001; Fernandes et al., 2002).

Note that the diffusion coefficient is a thermodynamic property, and therefore describes the statistical, average behavior of this particle and not its precise Newtonian dynamics. A molecule with a higher diffusion coefficient will be statistically more likely to be found at a farther distance from it's starting point within a fixed amount of time. Conversely, one may consider the average time a molecule takes to travel a specified distance. If that distance is L, this diffusive time constant τ_D given by

$$\tau_D = \frac{L^2}{D}. \tag{4.2}$$

In contrast to diffusion, convection is the movement of molecules due to fluid flow. It is not a thermodynamic stochastic process but a deterministic one (albeit chaotic in some cases). The velocity of a particle due to convection is simply the velocity of the fluid at that position, and the convective time (i.e., the time it takes a particle to move a specified distance) is simply the inverse. Consider, for example, laminar flow with volumetric flow rate Q in a square microfluidic chamber with width W and

height H. The average flow velocity in the chamber is $V = Q/WH$. Therefore, the time is takes a typical particle to travel a length of the chamber L (the convective time constant τ_C) is

$$\tau_C = \frac{WHL}{Q}. \tag{4.3}$$

In characterizing the flow chamber, it is useful to compare the time it takes a particle to flow down the chamber (the convective time) with the amount of time it would take a particle to diffuse all the way across the chamber to sensor surface (the diffusive time). If the diffusive time is much longer than the convective time, then the particles are being pushed along by the flow too fast for them to have much time to diffuse to the sensor. The ratio between diffusive time and convective time is a dimensionless number called the Peclet number:

$$Pe = \frac{\tau_D}{\tau_C} \approx \frac{H^2 D}{H^2 W/Q} \approx \frac{Q}{WD}. \tag{4.4}$$

Our flow chamber has a square cross section with a channel width of 800 µm and height of 25 µm. Practically we are limited by our pump to flow rates between $0.1\,\mu\mathrm{l\,min^{-1}}$ to $50\,\mu\mathrm{l\,min^{-1}}$. If we consider the diffusion coefficient of a typical GNR or nucleic acid as $D = 10\,\mu\mathrm{m^2\,s^{-1}}$, the *lowest* Peclet number we would observe in our system is

$$Pe(Q = 0.1\,\mu\mathrm{l\,min^{-1}}) = \frac{0.1\,\mu\mathrm{l\,min^{-1}}}{(25\,\mu\mathrm{m})\,(10\,\mu\mathrm{m^2\,s^{-1}})} \approx 6,700. \tag{4.5}$$

Clearly, the diffusive time is much larger than the convective time, or conversely, diffusion is slow compared to convection. This is only exacerbated if the diffusion coefficient is a bit smaller (which it could likely be), or if the flow rate is increased. In this regime the majority of particles flow right through the channel, following the stream lines and never diffusing close to the surface to bind. Only particles which are within a narrow corridor of the flow adjacent to the sensor have a chance

of getting close enough to the sensor surface to bind. This corridor is called the 'depletion zone', by virtue of the fact that an ideal sensor will bind most of the particles within this region and reduce their local concentration. In this regime, the flux of particles into the sensor depends on previously defined constants as well as the initial concentration of particles (c_0) as well as the length L and width W_s of the sensor (let $L = W_s = 100\,\mu\text{m}$, a typical microarray spot) (Squires et al., 2008):

$$\begin{aligned} J_D\left(c_0\right) &\approx \left(Dc_0W_s\right)\left(6\left(\frac{L}{H}\right)^2 Pe\right)^{1/3} \approx 86\left(10\,\mu\text{m}^2\,\text{s}^{-1}\right)\left(100\,\mu\text{m}\right)c_0 \\ &= \left(5\times 10^{-3}\mu\text{l}\,\text{min}^{-1}\right)c_0. \end{aligned} \tag{4.6}$$

If the starting concentration is $c_0 = 1\,\text{fM} \approx 600\,\text{molecules}/\mu\text{l}$ then the expected flux will be approximately 3 molecules per minute.

We can also use this equation to approximate the ultimate theoretical sensitivity limited only by mass transport kinetics. Let us say we have a nearly ideal sensor with virtually no noise and ideal surface probes with infinite affinity, and only require 10 particles to be captured in order to have 3σ confidence in a positive signal. If we limit our experiment time to 4 hours, the lowest concentration we will be able to detect will be

$$c_{LOD} = \frac{10\text{ molecules}}{240\,\text{min}\times 5\times 10^{-3}\mu\text{l}\,\text{min}^{-1}} = 8\ \frac{\text{molecules}}{\mu\text{l}} \approx 13\,\text{aM}. \tag{4.7}$$

Note that this limit of detection is in the case of an ideal molecule sensor: at this low concentration, less than four particles per hour will even get close enough to the sensor to bind. As we shall see, the sensitivity quickly decreases as the capture efficiency of the sensor decreases from 100%.

This type of calculation gives us a benchmark against which we can compare the performance of our sensor during optimization, and informs our expectations. Note that even if we extend the assay time to 12 hours, our ultimate sensitivity

limit stays at about $4\,\mathrm{aM} = 24,000$ molecules per ml. This does not compare to the most sensitive modern techniques for nucleic acid detection: modern quantitative PCR or droplet-based digital PCR (polymerase chain reaction) assays have a limit of detection 10,000-fold lower (i.e., as low as 1-2 molecule per ml) (Baker, 2012). The fundamental reason for this large discrepancy is that primer hybridization in PCR is a homogeneous reaction: there is no 'depletion zone' since both the target and primers are mixed together. In the next section, we shall discuss how this ultimate sensitivity limit is actually quite optimistic when we consider non-ideal probes with a finite affinity.

Theoretical and experimental comparison of schemes

All else being equal, homogeneous reactions are always faster than heterogeneous ones. Therefore, it is in our interest to replace heterogeneous incubations with homogeneous ones whenever possible. Furthermore, the heterogeneous approach has another issue related to sensitivity with non-ideal probes.

In the heterogeneous scheme, the sample solution are incubated with the chip first, then the chip is incubated with the GNR reporters. In the semi-homogeneous scheme, the GNR reporters are added to the sample solution first, and then the mixture is incubated with the chip. In both schemes, the number of nanoparticles after the second incubation can be counted to determine the signal. However, there is a way to gain additional information when using the semi-homogeneous scheme. Instead of counting the number of nanoparticles at the end of the second incubation, we could count the number of nanoparticles that bind to the chip during the incubation, in real time.

When probe molecules have a finite affinity, there will always be debinding of captured targets. In a canonical Langmuir binding model, the sensor will approach an equilibrium with the solution where the binding rate and debinding rate are equal.

For very low target concentrations (relative to the interaction dissociation constant), the time required to reach equilibrium depends only on the off-rate of the molecules since the sensor will never saturate (Squires et al., 2008). In a recent experiment we observed that, on average, about 2% of immobilized GNRs debound from the surface each minute (this experiment is described in detail in Section 5.2.2; Figure 5·5). From this, we can estimate that the off-rate is approximately 1 hour, since $k_off \approx 1\,\text{min}/.02 \approx 1$ hour.

If we make an endpoint measurement, at low concentrations, we do not gain any additional information from performing an incubation much longer than the off-rate. If we are able to monitor binding in real time, however, a longer experiment is always useful because we will always register more events. Note that for this application to work, it is crucial to be able to not only be able to count but also *distinguish* the GNRs, since at equilibrium the on- and off-rate will be equal by definition. In Chapter 5, we describe a robust nanoparticle tracking software code developed for this purpose.

This extra complexity does not come without some cost (primarily as the instrument and personnel time required for acquisition and analysis), so endpoint measurements are still often useful. Even when endpoint measurements are preferred however, the semi-homogeneous assay is still superior to the heterogeneous approach because of the reaction rates described earlier.

Finally we would like to draw attention to another, practical limitation of endpoint measurements related to accurately counting the nanoparticles without false negatives. All of the best results obtained by our group using the heterogeneous scheme have been obtained using endpoint measurements, and have had a similar form to Figure 4·6. Here, a standard curve is shown for a 10 hour assay (5 hours each of target incubation and GNR incubation) with varying concentrations of the

target and all other variables held constant. When this standard curve is plotted on logarithmic axes, however, the slope is much less than 1 over the entire dynamic range: a 10-fold change in target concentration results in just a 1.5-fold change in particle counts (Figure 4·6b). This puzzling result is not explained by the mass transport limits nor reaction kinetics that we have discussed in this section. However, it is possible that this a discrepancy is instead due to a readout error in nanoparticle counting, where nanoparticles which are too close together result in false negatives. In Section 3.4.4 we discussed this problem of nanoparticle crowding and put forth a mitigation strategy. However, the conclusion remains that the best approach for quantitative measurement remains real time counting.

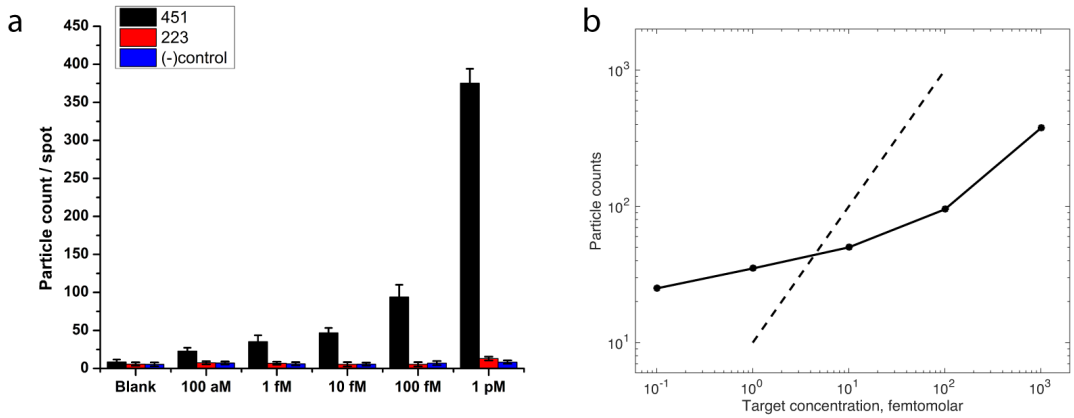

Figure 4·6: (a) Dilution standard curve between 100 aM and 1 pM for a synthetic 40 base pair RNA target (mir451) using the heterogeneous assay scheme. Target incubation and nanoparticle incubation (10 pM) were both each 5 hours long. Capture probe spots for mir223 and a sham negative control are included, and show less than 20 particles per spot on average ($n = 16$ replicate spots on each chip, for each condition). (b) The mean values from (a) are replotted with logarithmic axes. The dotted line indicates a slope of 1, as a guide to the eye.

4.2.4 Optimization of hybridization conditions and buffers

In the previous section, we mentioned briefly that that assay sensitivity depends on not just mass transport but also the affinity of the probes for the target molecule. For nucleic acid probes, this affinity depends on not just the molecules themselves but also several intensive properties of the solution such as temperature, pH and ion concentration.

The effect of temperature, pH and cation concentration on the binding free energy of complementary nucleic acids is widely known (Dirks et al., 2007; Yakovchuk et al., 2006; Malutan and Vilda, 2012; Lytton-Jean and Mirkin, 2005; Xu and Craig, 2005; Binder, 2006; Carlon and Heim, 2006; Randeria et al., 2015; Vainrub and Montgomery Pettitt, 2003). Briefly, the Gibbs free energy of binding between two molecular species depends on the stored potential energy as well as the degrees of freedom (entropy) of the bound complex, compared to the total entropy of the two molecules separately in solution.

Single stranded nucleic acids are characteristically long, flexible polymers with a negatively-charged phosphate backbone. The main enthalpic penalty to duplex formation is electrostatic repulsion between the backbones of the strands, and the main entropic penalty is that the conformational flexibility of the duplex is much less than that of the two separate strands. Decreasing pH (i.e., increasing proton concentration) or increasing cation concentration increase the free energy of binding by screening the electrostatic repulsion between the phosphate backbones. Decreasing temperature also increases the binding free energy, but because it reduces the degree of the entropic penalty (remember that $\Delta G = \Delta U - T\Delta S$). Other molecular species such as surfactants and buffer anions have roles in reducing nonspecific interactions and maintaining solution pH. For example, we have found that sodium dodecyl sulfate (SDS, a surfactant) greatly reduces nonspecific interactions of GNRs with the IRIS

chip surface and improves overall assay specificity.

Our strategy was to optimize the assay hybridization conditions in two phases. First, we maximized sensitivity without regard for nonspecific nucleic acid interaction. Once the sensitivity of the assay was at least approximately close to the mass transport limits, we then focused on ways to improve specificity. The following two subsections discuss each of these two phases of optimization.

Improving sensitivity with increased charge screening

In preliminary experiments, the number of bound nanoparticles was very low compared to what mass transport would predict. This indicated a very low affinity between the surface probe and the target-GNR complex. In one case for example, a heterogeneous assay was performed where a dummy sample solution containing 100 fM target was incubated with the chip for 16 hours, followed by 6 hours of incubation with GNR reporters at 1 pM (Figure 4·7). Only about 50 particles were counted on each of the positive control spots. For comparison, we can estimate from our earlier calculations that at 100 fM, perhaps as many as 300, 000 target molecules had diffused close enough to each spot to be captured.

Clearly, this 10,000-fold discrepancy between experiment and theory provided plenty of room for improvement. We were puzzled, however, since we were following previously published protocols for both the first incubation with the free target molecules, and second incubation with the GNRs (Ozkumur et al., 2010; Hill and Mirkin, 2006).

One slight difference between our scheme and the published protocol was the size of the gold nanoparticles. Hill and colleagues used particles 30 nm in diameter, whereas we were using somewhat larger nanorods 25 nm in diameter and 70 nm long.

As mentioned earlier, electrostatic repulsion between the phosphate backbones of nucleic acids is the main enthalpic barrier to duplex formation. Many groups haveob-

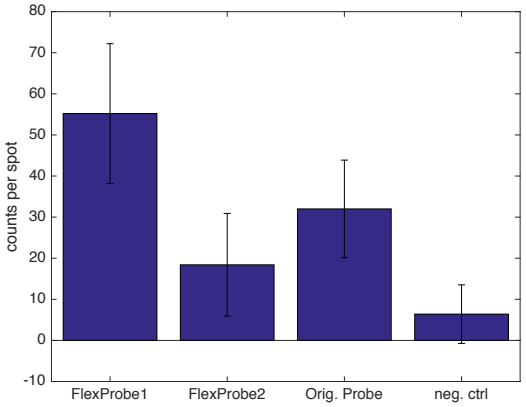

Figure 4·7: An early comparison of capture probes for a nucleic acid assay before optimization. The heterogeneous scheme was used. A solution of 100 fM target was incubated for 16 hours, followed by 6 hours of incubation with GNR reporters. While a positive signal of about 20-50 particles were observed across all of the capture probes except the negative control (right-most), calculations of the mass transport limit suggested that the target capture efficiency was only about .2%.

served that electrostatic repulsion is even more pronounced in DNA microarrays, since the immobilized probes are packed close together on the surface (Peterson et al., 2001; Vainrub and Montgomery Pettitt, 2003; Gong and Levicky, 2008; Malutan and Vilda, 2012). Others have noticed the same effect on DNA-conjugated gold nanoparticles, which are also covered with densely packed DNA oligos (Randeria et al., 2015; Chen et al., 2009). Based on these reports we suspected that this electrostatic repulsion was likely very high in our assay, perhaps even more so since our nanoparticles were somewhat large. We hypothesized that increasing the concentration of ionic sodium would increase the screening of this repulsion and result in higher sensitivity.

To test this we performed two semi-homogeneous assays that were otherwise identical except that the final heterogeneous incubation was performed with either 150 mM ionic sodium (Na^+) or 600 mM Na^+. In both, a 1 hour homogeneous incubation of 10 fM target sequences with 1 pM GNRs at 600 mM Na^+ was performed, after which

the solutions were injected into microfluidic flow chambers containing the IRIS chips. The microfluidic flow chamber allowed the binding of GNRs to the complementary spot to be imaged in real time (more on this approach in Chapter 5), and we observed that the binding rate of GNRs of the sample with 600 mM Na^+ was increased by over 10-fold (Figure 4·8).

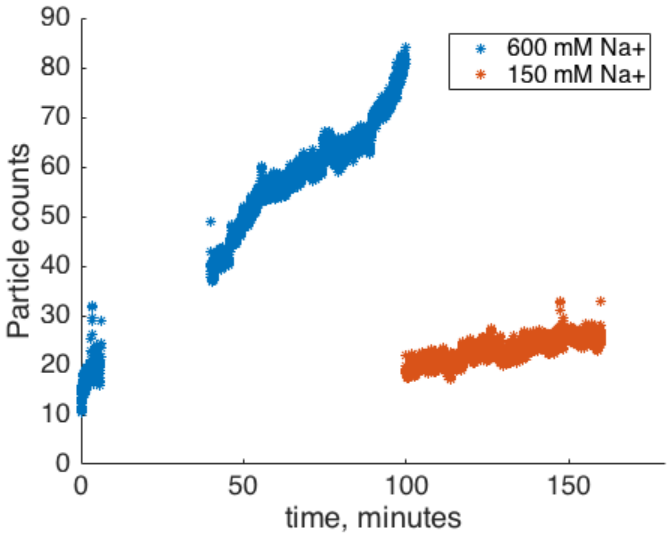

Figure 4·8: Real time counting of gold nanorods in 150 mM vs. 600 mM ionic sodium Na^+. A semi-homogeneous assay with a target concentration of 10 fM was performed otherwise identically. Due to problems with image acquisition a significant amount of data was not saved, yet the gross trend is still clear.

This finding was promising, and motivated a more in-depth follow up study. We were interested to see if 600 mM Na^+ was simply above a threshold, or part of a trend that continued to even higher sodium concentrations. We also wished to reevaluate the impact of the stabilizer sequence. Despite the apparent advantages of stabilization that we showed earlier, the stabilizer would also increase the density of DNAs on the microarray spot and therefore could slightly increase electrostatic repulsion.

We therefore prepared 10 identical IRIS chips with the four capture probes for the AST expression assay described earlier, to test the 5 x 2 matrix of conditions:

150, 300, 450, 600, and 750 mM Na^+, each both with and without stabilizers. The homogeneous incubation was performed identically for all conditions, by incubating 5 pM of the target sequences with 200 pM GNRs, in 600 mM NA^+. This 'master mix' was diluted 10-fold into five solutions of 1x PBS with 0.1% SDS with 150 mM to 750 mM Na^+, resulting in a final target concentration of 500 fM. One chip each with and without stabilizer was incubated with each of the five solutions for 90 minutes. The chips were all washed once in 1x PBS with 0.1% SDS, then twice more in 1x PBS, for 30 seconds each before drying. Finally, each chip was then scanned using SP-IRIS (Figure 4·9).

The target-complement spots had too many nanoparticles to be reliably counted on the 450-750 mM Na^+ samples, so instead we measured the total absorbance of the spots by taking the average difference in intensity within each spot from the local background. This 'analog' measurement approach has not been validated thoroughly, but it gives the correct qualitative picture (e.g, as in Figure 4·3). These results clearly showed that increasing cation concentration greatly increased hybridization efficiency. However, increasing sodium also increased nonspecific binding to the non-complementary control spots by about 2-fold. The stabilizer was observed to strongly increase binding as before, and did not increase nonspecific binding (Figure 4·9).

We also first noted in this experiment that at sodium concentrations at 600 mM and above, a filmy precipitate gradually formed on the surface of the solution over the course of the experiment. The precipitation was faster and more complete with higher sodium concentration, fitting with a standard picture of SDS solubility. When we conducted longer experiments of the same type (e.g., 5 hours) or attempted to use even higher sodium concentrations (e.g., 1 M) we saw nonspecific binding of GNRs to the entire chip surface, indicating that most of the SDS had precipitated. This nonspecific interaction was at least partially reversible—a 5 minute wash with a high

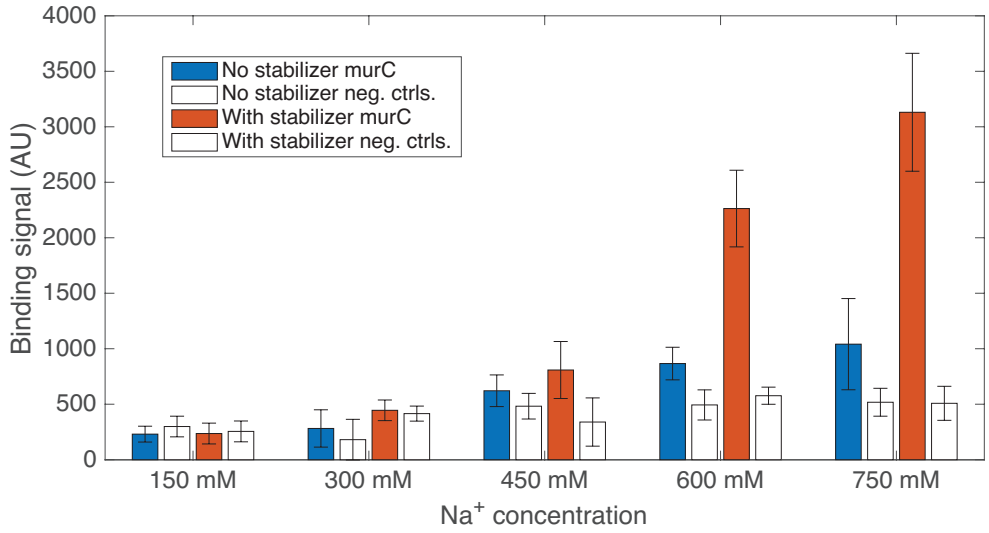

Figure 4·9: Optimization of sensitivity. 500 fM synthetic murC analog targets were detected using the semi-homogeneous scheme. Adding stabilizer sequences and increasing the sodium ion (Na^+) concentration both increased the number of bound GNRs. Increasing Na^+ also slightly increased nonspecific binding

.

concentration of surfactant (1% SDS) would debind most (but not all) of the nonspecific particles from the surface.

Improved specificity with optimized wash buffers

As we have shown, increasing charge screening greatly improves sensitivity. However we also found that it slightly increased nonspecific DNA-DNA interactions, resulting in the number of GNRs on the negative control spots to increase by about 2-fold. We suspected that these nonspecific interactions could be reduced by performing an optimized washing procedure after the incubation. Generally speaking, the wash buffers can have a significant impact on the final result. A single rinse with DI water, for example, is likely to cause rapid disassociation of many of the duplexes and reduce sensitivity. However, a wash with too high of a salt concentration will not cause any of the nonspecific interactions to dissociate.

In earlier work, Hill and colleagues developed a DNA-nanoparticle based microarray which had very low nonspecific binding (Hill and Mirkin, 2006). Their wash procedure involved multiple steps, in which first excess nanoparticles were washed away using 1x PBS with 0.01% SDS and 0.02% Tween-20. They then washed the chip with 500 mM sodium nitrate, followed by a rapid dip in cooled 100 mM sodium nitrate solution (refrigerated 4 °C). We believe that Hill and colleagues performed washes with sodium nitrate because they needed to wash away any trace phosphate ions, since their assay next involved dipping the chip into a solution of ionic silver. The ionic silver reduces onto the gold nanoparticles and enhances their optical scattering, but any phosphate ions would cause precipitation of insoluble silver phosphate. This precipitate would cause significant background signal for their absorbance-based reader, and because DNA spots are very hydrophilic and retain small amounts of water during chip drying.

Nevertheless, we were impressed by their results an decided to try their wash protocol instead, and found that it outperformed our original protocol. We further found that performing multiple wash steps with their first wash buffer (again, 1x PBS with 0.01% SDS and 0.02% Tween-20) further reduced the amount of particles on the negative control spots to 1 or less on average, without reducing the positive control spot signal.

We believe that the wash protocol developed by Hill and colleagues has two essential key features which our previous protocols did not, which contribute to its high performance. First, the wash buffer contains Tween-20 in addition to a much lower concentration of SDS. The reason this is important actually doesn't have to do with DNA-DNA interactions, but simply the practical matter of how the chip washing is performed. The chips are washed by sequentially submersing them in different petri dishes containing the wash buffers. When the chip is withdrawn from a bath, the

sensor surface (which is on the topside of the chip) is drawn into contact with the buffer's air-liquid interface. As a surfactant, SDS spontaneously assembles at this interface. However, SDS also strongly complexes with gold nanoparticles. Therefore, we suspect that the SDS artificially concentrates gold nanoparticles at the air-liquid interface. This is corroborated by our observations that if the second incubation is performed in a small (e.g. 20 µl) droplet that only partially covers chip, many more GNRs bind to the chip near the edges of the droplet than near the middle.

When the chip is removed from the wash buffer, the chip is drawn through a boundary layer where the nanoparticles are relatively concentrated. We observed that a wash buffer with a much lower concentration of SDS and a larger concentration of Tween-20 had fewer nonspecific particles on the spots, and suspect that the addition of excess Tween may reduce this proposed interface effect by displacing the SDS on the air-water interface.

The second key aspect is that the final wash step is performed using a low sodium concentration (100 mM), but at a significantly lower temperature (4 °C). Remember that lowering temperature reduces the entropic contribution to the binding free energy. The reason lowering the salt concentration of the final wash is important is that the spots are hydrophilic, and they retain hydrated as the chip is withdrawn form the buffer. These microdroplets evaporate very quickly, and leave salt crystal residues on the spot (for example, note the white crystals near the center of the 'no stabilizer' spot in Figure 4·3). These crystals can be falsely be detected as GNRs by software, which adds variability and thereby reduces sensitivity. In general, lowering the salt concentration reduces the size and number of salt crystals.

4.3 Software for high throughput chip scanning & image processing

Once the assay is complete, the chip must be scanned by the optical system. If the microarray is larger than one field of view, the microarray must be tiled and the instrument must acquire images at each tile position to the next. Then, the nanoparticles must be counted across the entire array, and finally the nanoparticles within each spot must be counted and the data correlated with the probe conditions. This is a considerable amount of work for each assay, and in the past it was normal to have the operator spend an entire day acquiring gigabytes of images, processing the images to count particles, and then processing the particle counts into the final assay results even for very small arrays of 12 to 24 spots.

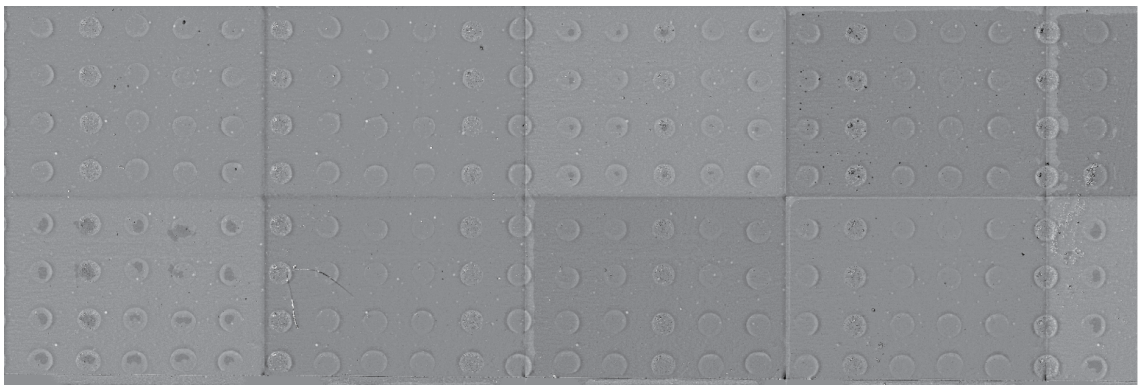

Figure 4·10: An example of the preview image of an 8 x 23 array with a 250 µm pitch acquired using SPANDEX. Image acquisition and processing, including particle detection, took about 8 minutes altogether.

It quickly became clear that the high throughput optical instrument could not be utilized unless the data acquisition, processing and analysis could be similarly accelerated. We therefore developed a suite of software tools that completely automated the instrument, particle detection, and the data analysis steps. This software suite is called the Single Particle Analysis and Detection Experience (SPANDEX), and it is described in detail in Appendix A.

Briefly, SPANDEX includes a fully-automated acquisition system in which the operator needs only to load a chip and set some relevant parameters in order to initiate the scan. An array of 500 spots with a 150 µm pitch (e.g., approximately 3 mm^2 to 4 mm^2) is scanned in less than 10 minutes. The instrument saves a preview image of the entire microarray, and an accompanying particle data file that lists the (x, y) position of every single GNR on the array (Figure 4·10). These two files are very small (<10 megabytes) compared to the amount of raw image data acquired during the scan (often over 50 gigabytes) yet contain all of the relevant information. The operator can then immediately inspect the particle data in an accompanying MATLAB tool, which aids the operator in segmenting the microarray spots using the preview image, so the particles within each spot can be tallied. Statistics or data visualization can then be immediately performed in MATLAB.

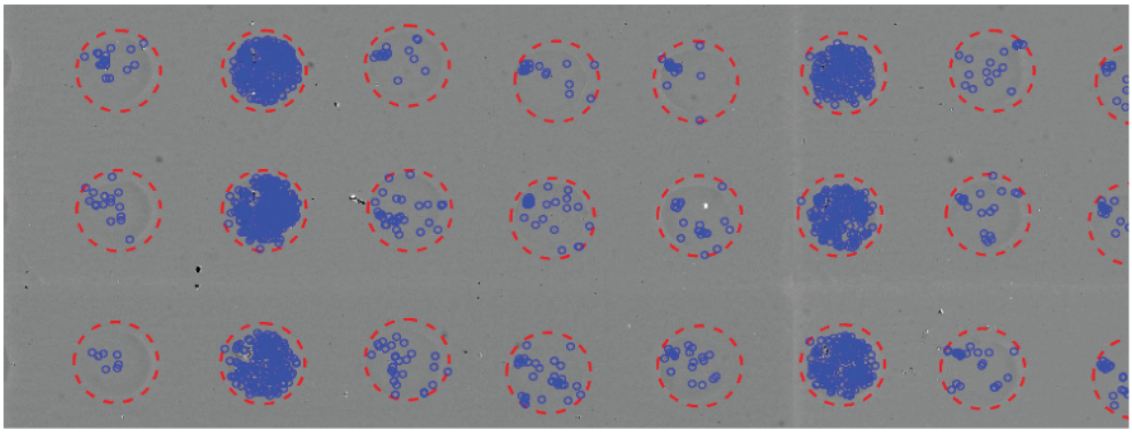

Figure 4·11: An example of particle analysis with SPANDEX. The operator is aided in identifying the microarray spots, and particles within each spot are tallied.

4.4 Conclusions

4.4.1 Summary

In this Chapter, we describe the design, implementation and optimization of a digital microarray assay. We decided to focus our development on an mRNA expression assay that could be used as part of a rapid AST. We designed DNA oligo probes for genes which have been shown to be highly up- or down-regulated in response to antibiotic exposure, and used synthetic DNA oligonucleotides as surrogates for those mRNAs during assay optimization thus far.

Like many other types of assays, digital microarrays are based on a sandwich assay scheme. We described two practical schemes in which the assay could be conducted (heterogeneous vs. semi-homogeneous), and compared their performance both theoretically and experimentally. We also characterized the mass transport limits of our sensor, which gave us a 'best case scenario' to which we could compare our results during assay optimization.

In order to maximize the assay's sensitivity and specificity we adjusted the hybridization buffer based on a thermodynamic picture of DNA-DNA binding. Briefly, we found that using a stabilizer sequence and increasing the concentration of ionic sodium both increased sensitivity by at least 10-fold. We also found that by using optimized washing buffers which either contained different surfactants or were refrigerated, we were able to reduce nonspecific interactions to less than one particle per spot on average.

Finally, we described a suite of software tools that it possible to utilize the high throughput nanoparticle detection technique to its full potential, by automating many of the data acquisition, processing and analysis processes.

4.4.2 Future work

A significant amount of practical work remains in optimizing, characterizing and validating the digital microarray assay for mRNA expression profiling of antibiotic resistance. One very promising area for optimization is modification of the probe sequences. First, the universal label-reporter duplex should probably be lengthened from 18 base pairs to at least 30 base pairs so that it is longer than the target-complementary regions. Literature discussing the affinity of DNA-nanoparticle conjugates also suggests that increasing the length of the spacer on the universal probe from 4 to perhaps 10 nucleotides could improve affinity through increased flexibility (Lytton-Jean and Mirkin, 2005; Jin et al., 2003). Additionally, the effect of increasing the total linker length by increasing the length of the reporter sequence could be investigated. Our optimization work strongly suggested that reducing electrostatic repulsion between the surface and the nanoparticle improved hybridization efficiency and affinity. But, this repulsion is a local phenomenon which decays quadratically with distance. Increasing the length of the reporter sequence could increase the overall length of the tether between the nanoparticle and the surface. However, one must keep in mind that a longer reporter sequence will also result in a physically larger DNA-GNR conjugate, and any benefits from a longer tether may be canceled out by this.

The effect of a larger target site should also be investigated, for example by increasing the target site from 50 to 60 base pairs and increasing the capture probe and reporter region from 25 to 30 base pairs each. This would obviously increase the free energy of binding and improve assay specificity. The only limiting factor in this regard is cost—synthesis of long oligonucleotides (e.g. over 60 bases) becomes expensive since yield begins to drop rapidly. Nevertheless the total per-test cost of the digital microarray system would remain about the same (<\$5) even if the cost

of all probes were increased 10-fold, so this is certainly a viable strategy to assay improvement.

Finally, there are some ways in which the acquisition & analysis software could be improved, mostly in the final analysis. Currently the software does not have any automatic spot detection or segmentation. If the array is printed with a regular pattern it is relatively easy for the user to generate a grid of ROIs, but the user must adjust regions manually if the pattern is erratic or if some spots do not line up with the others. Also, the analysis does not load metadata about the spotted probe conditions: if it did, the operator would be able to generate meaningful plots even faster.

Chapter 5

Techniques for kinetic measurements of nanoparticle binding

5.1 Motivation

5.1.1 The advantages of in-liquid imaging

As described in earlier chapters, SP-IRIS allows the identification and measurement of individual immobilized nanoparticles. There are numerous advantages to performing these measurements while the sensor substrate is still immersed in solution, rather than drying it first. Some applications require samples to be imaged while they are still in water. For example, the morphology of biological nanoparticles like viruses and exosomes may change when they are dried, which can interfere with their measurement. Also, drying the substrate often leaves small salt crystal deposits on the spots, as mentioned in Section 4.2.4. These salt crystals can be falsely detected as nanoparticles and be a source of variability.

Another advantage of in-liquid imaging is that it allows data to be acquired during the assay in 'real time', and not just at the end. For example, the binding and debinding kinetics of nanoparticles are of great interest in many applications since it enables measurements of the molecular affinity between the particle and the surface. Also, when the interaction between the nanoparticle and the surface is weak, real time measurements of particle binding will provide much higher sensitivity than 'endpoint' measurements.

5.1.2 A rare mutation assay using digital microarrays

The problem of rare mutation detection has growing clinical significance in oncology, especially for cancers for which a targeted chemotherapy has been developed. For example, the drug Cetuximab is often prescribed for patients with metastatic colorectal cancer. Cetuximab is an antibody which binds to the epidermal growth factor receptor (EGFR) and effectively inhibits the growth of colorectal cancer tumors. Crucially however, tumor cells which have a mutation in the *KRAS* gene are resistant to Cetuximab and will continue to proliferate. After surgery, the excised tumor is often screened for *KRAS* mutations, and Cetuximab is only prescribed if the tumor is wild type. Even then however, Cetuximab acts as a powerful selective pressure: tumors treated with Cetuximab often have secondary resistance after an initial response. The process by which this resistance is acquired is generally accepted to be through random mutation and genetic heterogeneity within the tumor: the therapy inhibits growth and replication of those tumor cells which do not have a mutant *KRAS* gene, so eventually any tumor cell which has a mutant *KRAS* gene will proliferate and eventually dominate the tumor micro-environment.

Recently, the possibility of using circulating tumor DNA as biomarkers of resistance has been investigated. Circulating cell free DNA is found in small quantities in the bloodstream of all bodies, and circulating tumor DNA (ctDNA) is also detectable in blood (Forshew et al., 2012). Detection of ctDNA is made challenging by the fact that this source of genetic material is very small in both relative and absolute quantities: only a handful of ctDNA fragments may be found in a single blood sample, and there is an overwhelmingly larger amount of cell free DNA from healthy cells in the body.

The most common laboratory technique for detection of extremely rare DNA alleles is digital PCR. As described in the introduction, this technique involves dividing

the sample solution into millions of individual volumes before PCR amplification, enough so that each sample nucleic acid is isolated in a single nano-well or droplet. After amplification and readout, the absolute number of detected DNAs is measured by simply counting the number of droplets with a positive signal (Vogelstein and Kinzler, 1999). Two recent studies used digital PCR to test the blood of patients with metastatic colorectal cancer for ctDNA following Cetuximab therapy, They were able to later detect KRAS–mutant ctDNA in 60% and 38% of the patients in the respective studies, up to 10 months before tumor progression was detectable by imaging (Misale et al., 2012; Diaz Jr et al., 2012). Similar results have been found for other such targeted treatment outcome studies, and largely imply that targeted therapy based on the modal population of clones is often not sufficient, and that more sensitive and comprehensive monitoring is required (Turner and Reis-Filho, 2012).

Digital PCR is used for detecting rare alleles because of its excellent sensitivity, but as an amplification based method it cannot be multiplexed above 10 primers (fewer when looking at the same gene region). This is a major limitation for rare mutation detection in cancer diagnostics because there are often many different mutations to the same loci which will confer resistance (Janku, 2014). For example, Palomba and colleagues recently performed sequencing of 473 colorectal cancer tumors and discovered no less than 13 different substitution mutations in the *KRAS* gene alone, six of them occurring within the same codon (Palomba et al., 2012). Targeted deep sequencing is becoming more popular, but the cost of the test remains relatively high.

In a recent paper, Galbiati and colleagues developed a fluorescence microarray assay for rare mutations that was able to detect rare alleles as low as 1:10,000 relative abundance in a multiplexed manner (Galbiati et al., 2013). This assay was not sensitive—it required an abundant amount of genetic material—but nevertheless demonstrated the utility of the microarray format in this application for testing for

many different possible mutations. We hypothesized that digital microarrays would be a natural substitution since they are much more sensitive.

5.2 Real time imaging and tracking of nanoparticle binding

5.2.1 Flow cell requirements and design

Based on the applications mentioned in Section 5.1.1, we identified the following requirements for the SP-IRIS microfluidic system:

1. The flow cell must have a sufficiently large viewing window to accommodate multiple microarray spots (e.g. at least 1 mm by 1 mm);

2. The total thickness between the substrate and outermost surface of the viewing window must be no more than 300 µm, to accommodate the small working distance of a 0.9 NA objective;

3. The viewing window must be optically flat and aligned to the surface of the chip; and

4. The fluid within the flow cell should be able to be pumped in a controlled manner, and fully exchanged with another solution without drying and during image acquisition.

Due to Requirement 1, the entire microfluidic system needed to be very thin, and the inlet and outlet ports needed be mounted on either the top or underside of the final assembly. Putting the ports on the top or underside each posed different challenges, and both options were pursued. To put the ports on the underside of the chip, two holes needed to be made all the way through the IRIS substrate for the fluid inlet and outlet. We used deep reactive ion etching on wafers which had been patterned with photoresist to expose the desired hole locations. The wafers were then

diced into chips and plastic nozzles were then glued to the underside so tubes could be attached. To complete the channel, No. 1.5 coverglass was adhered to the chip surface using a layer of double sided pressure sensitive adhesive. The geometry of the flow channel was cut into the adhesive with a laser cutter. The final assemblies consisted of three separate parts (the chip, the adhesive and the coverglass) that were irreversibly assembled by hand, one at a time.

In parallel, we pursued another approach that did not require through holes in silicon. Making the holes with deep reactive ion etching was quite time consuming, complicated and difficult—we had needed expert help to develop and run the procedure. We reasoned that a 'top-side' cartridge may be simpler and more affordable. In this scheme, the liquid would be routed onto and across the chip by a multi-layer stack of plastic adhesive films. These films would be cut (again with a laser cutter) and stacked to create a more complex fluid channel as in Figure 5·1. In this case the flow cell is significantly more complex because there are many layers of plastic films supported by a stiff acrylic base. However, all of this additional complexity meant that chips that we currently had could be used in the system immediately, without the need to make any holes. Our group identified a vendor who could make the laminate systems, so it was a natural choice.

5.2.2 Kinetic measurements of nanoparticle binding and debinding

The flow cell enabled real time imaging of the chip during nanoparticle binding which we found greatly improved the sensitivity of our assays. Instead of measuring the number of bound particles at the end of the experiment, the *rate* of nanoparticle binding could be quantitatively measured. For example, in an assay for virus particles, the microfluidic flow cell enabled the detection of a concentration as low as 100 plaque-forming units per ml (Figure 5·2). This assay had a very large dynamic range (over 10,000) since it could also very high concentrations by looking at the *initial* slope of

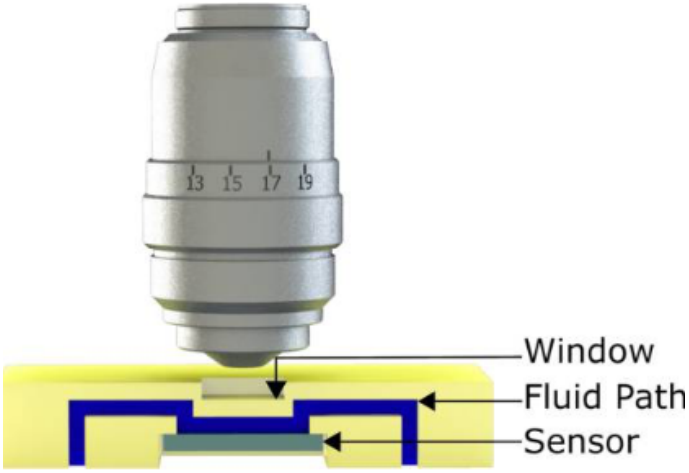

Figure 5·1: Schematic of the multilayer laminate flow cell. We found that the multilayer laminate design was simpler to implement than the silicon through-hole design.

the binding curve, before saturation.

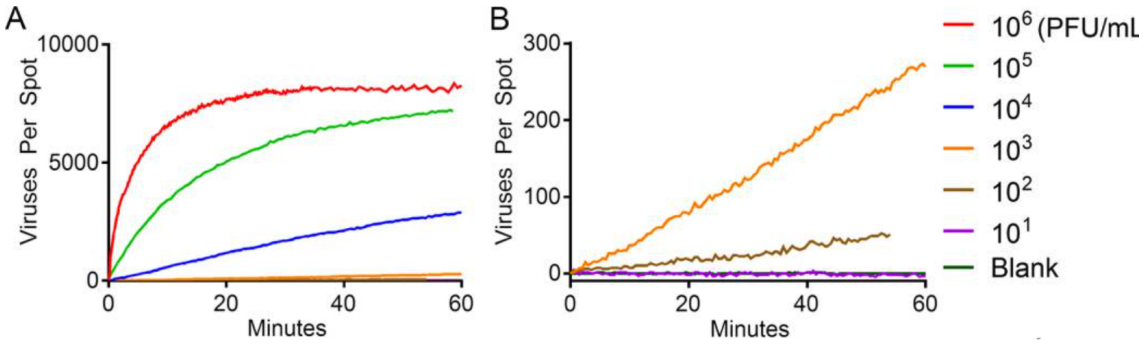

Figure 5·2: Real time data of viruses binding to an antibody spot. The rate at which viruses bind to the spot is initially linear with a slope proportional to the concentration of virus particles.

It is worth noting that these experimental slopes are within one order of magnitude of the diffusion limit imposed by mass transport, which suggests that the affinity of the capture probes (antibodies) for the virus particles was very high. This was corroborated by the observation that the virus particles almost never debound from the surface. A likely explanation is that the viruses may have been binding to more than one antibody given the very high density of antibodies on the spots. The

saturation observed for high concentrations in Figure 5·2 is actually therefore not due to having reached an equilibrium: the microarray has over one million binding sites for viruses, yet apparently saturates at about 8,000. Instead, the saturation is most likely caused by the viruses becoming too crowded on the surface to individually distinguish—compare these curves to the simulations of particle crowding described in Section 3.4.4 (Figure 3·15).

We were also interested in making this measurement using DNA-conjugated gold nanorods (GNRs), to improve the performance of the rapid mRNA assay described in Chapter 4. In an early test, we wished to investigate the effect of flow rate on the binding rate of GNRs. We hypothesized that the binding rate would increase with the cube root of the flow rate, e.g. $J_D \propto Q^{1/3}$, since this was the behavior predicted by the flow regime in Chapter 4 (Squires et al., 2008). We therefore performed a semi-homogeneous assay with a 15 fM target, in which the final incubation was performed in the flow cell. We increased the speed of the flow every 20 minutes, from 0.1 µl min^{-1} to 30 µl min^{-1}.

Unfortunately, we observed somewhat noisier data in these experiments than we had with the virus experiments (Figure 5·3a). More importantly, the binding rate was not nearly as close to the theoretical mass transport limit. Inspection of the raw image data revealed that a significant number of GNRs were in fact debinding from the spot, which lowered the signal.

Another problem was that unlike the optical signal from a virus, the optical signal from a GNR depends on its surface orientation which can changes as the particle undergoes Brownian motion. Sometimes a GNR would momentarily seem to disappear and then reappear in a subsequent image. This increased the variability in the total count from frame to frame. To overcome these problems we developed an algorithm which is able to robustly keep track of individual nanoparticles from frame to frame

in the video, even if it was not in every frame (this algorithm is described in detail in the next section). With this method we were able to obtain much better results (Figure 5·3b). Not only was the variability almost entirely removed, but we could observe that the actual binding rate was about twice as high as the total particle counts would suggest. We could also measure the rate at which GNRs were debinding, as well.

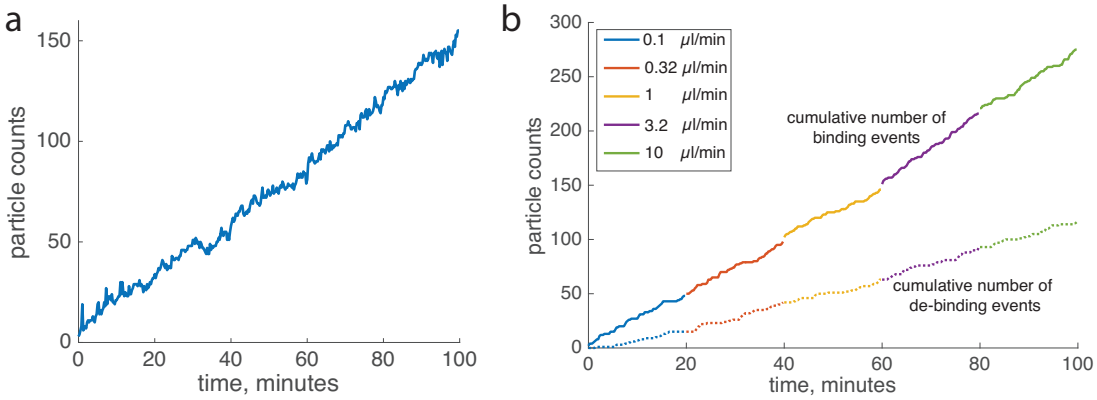

Figure 5·3: Binding of gold nanorods over time at different flow rates. (a) The total number of particles in each frame shows significantly higher noise than the earlier data of virus binding. (b) After applying particle tracking the noise is almost entirely eliminated.

The absolute binding and debinding rates at different flow rates were measured by simply taking the slope of each of the corresponding sections of the curves in the particle tracking results (Figure 5·3b). We observed that the binding rate stayed approximately constant for all flow rates, at about 3 particles per minute (Figure 5·4). This data did not agree with our hypothesis that increasing flow should increase binding - the kinetics model predicted a $100^{1/3} \approx 4.6$ fold increase in binding rate between $0.1\,\mu l\,min^{-1}$ and $10\,\mu l\,min^{-1}$.

The debinding rates shown in Figure 5·4 are not actually meaningful by themselves, because the total number of particles on the spot was changing throughout the experiment. Instead, we needed to measure the relative debinding rate at differ-

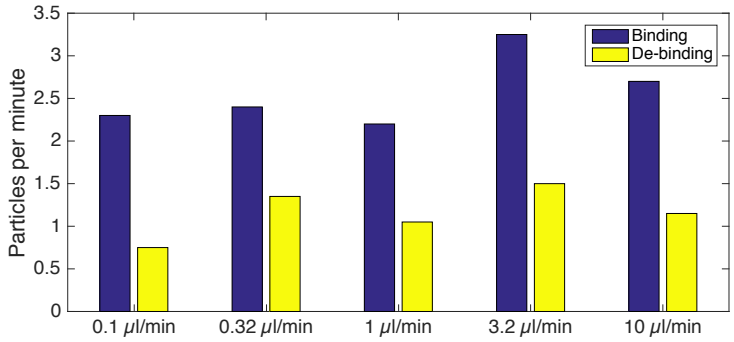

Figure 5·4: The absolute binding and debinding rate of GNRs at different flow rates. The absolute binding and debinding rate are surprisingly consistent.

ent time points by normalizing by the total number of bound particles—this is the canonical disassociation or off rate k_{off} (Figure 5·5). We had hypothesized that the off rate could increase with increasing flow rate since the GNRs may experience a larger shear force from convection, but this was not observed.

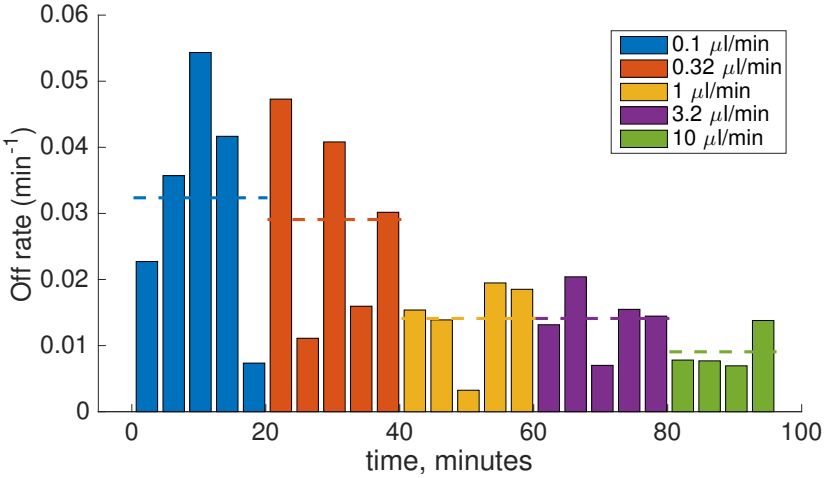

Figure 5·5: The off rate of particles during the course of the flow rate experiment. The off rate decreased from about $0.03\,\mathrm{min}^{-1}$ to $0.01\,\mathrm{min}^{-1}$.

Altogether, these results suggest that more experiments are required to understand the effect of flow rate on binding, because the results did not match our expectations

based on the kinetics model described in Section 4.2.3. The fact that flow rate had no effect at all suggests that something may have been wrong with the apparatus, such as a leak or pump user error, which could have caused the flow rate to actually have remained constant throughout the experiment. Nevertheless, this study demonstrates the effectiveness of the nanoparticle tracking method at reducing variability.

Particle tracking is not always required to obtain useful data using the real time system. The disassociation kinetics of GNRs can be measured without any particle tracking by simply flowing a wash buffer once GNRs have bound to the spot. To demonstrate this, we performed a semi-homogeneous assay of 10 fM targets just as before, but after 1 hour of binding we flowed a solution of 0.2x SSC buffer (30 mM Na^+). We wished to evaluate a wash protocol published by Galbiati and colleagues that was designed to have very high specificity, which utilized this buffer (Galbiati et al., 2013). We observed that most of the GNRs on the target-complementary spot debound within 10 minutes of washing (Figure 5·6).

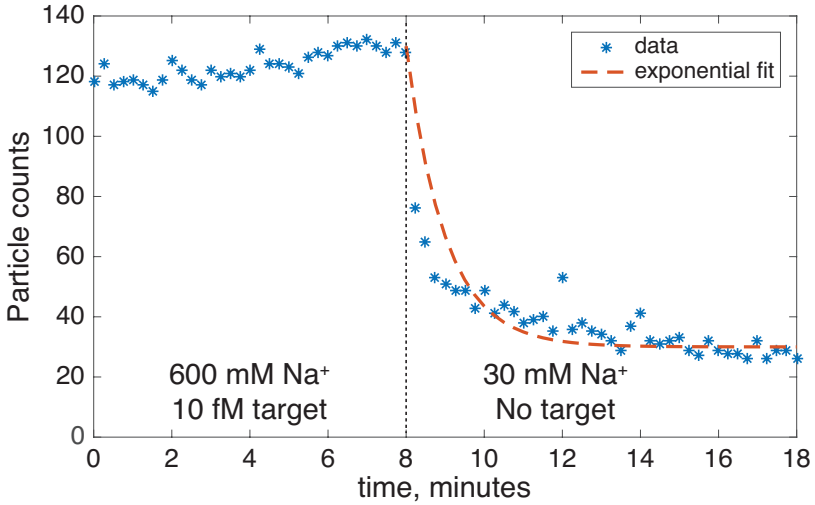

Figure 5·6: Dehybridization of bound GNRs from the target-complementary spot upon introduction of 0.2x SSC buffer (30 mM Na^+). The dehybridization was fit with an exponential decay to measure the off rate.

We can fit standard exponential decay model to the dehybridization curve to quantitatively measure the off rate:

$$N(t) \propto Ae^{-(t)/\tau_d} + B \tag{5.1}$$

where $N(t)$ is the total number of particles on the spot, A and B are scaling constants and τ_d is the characteristic debinding time scale, which was found to be $\tau_d = 103$ seconds. The off rate in this case is simply $k_{off} \equiv \tau_d^{-1} \approx 0.01\,\mathrm{s}^{-1}$.

5.2.3 Tracking of nanoparticles in video data

The video data that can be obtained using the microfluidic flow cell contains a wealth of information beyond simply the total number of nanoparticles detected in each frame. Visual inspection of the video data reveals, for example, that in some cases nanoparticles may depart the surface after being immobilized for some time. The debinding of particles is 'invisible' in the analyses described earlier, and can have a significant impact on assay performance when the molecular affinity between the particle and surface is weak.

For example, consider a simple Langmuir model in which the solution contains a concentration of target nanoparticles such that one nanoparticle binds to the sensor surface about every 10 minutes, and any particular immobilized nanoparticle has a 20% chance of debinding within a one hour window. During the beginning of the assay, the total number of bound nanoparticles will increase approximately linearly (with Poisson noise), as particles bind every 10 minutes or so. However, the rate of increase of the total number of immobilized particles will begin to slow after about 2 hours and the total number will asymptotically approach 30, at which the binding and debinding rates are equal. If however the debinding of particles was also measured, the number of new interactions could continue to be monitored even at equilibrium

(Figure 5·7).

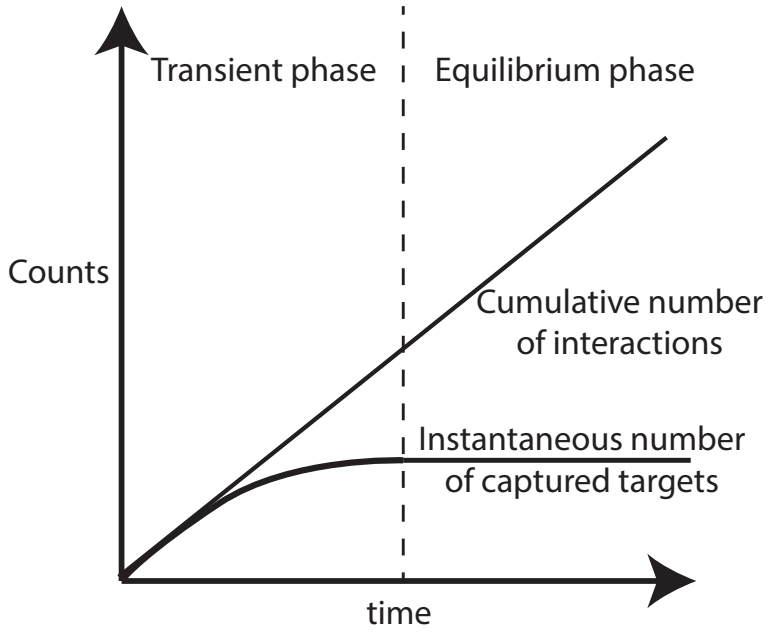

Figure 5·7: Schematic of the advantage of particle tracking. Even when Langmuir equilibrium is reached and the total number of nanoparticles remains constant, new interactions will continue to be detectable.

To measure particle debinding, the positions of particles in successive images may be compared. If a video frame at time t_n shows a particle in a particular position, but that particle is no longer present in the succeeding frame at t_{n+1}, then that particle has likely debound from the surface. This process of *matching* the particles in one frame to the next can be logically extended to the entire video, in which each and every particle is *tracked* from the frame in which it binds to the frame in which it debinds, or the end of the video.

Particle tracking has significant utility also for reducing noise. For example, nanoparticles that pass near the substrate (but are not immobilized) can still be detected transiently in single images. These 'floaters' are a source of noise and add variability to the total number of nanoparticles in each frame, but with particle tracking they can be ignored (Figure 5·8a). Another source of variability is that the particle

detection software is not perfect, and an immobilized particle may have some small probability of being missed entirely in one frame, but detected in most others.

Solutions to the technical problem of accurately tracking multiple particles with high spatial resolution have been thoroughly investigated and developed by others, for example in the form of particle tracking velocimetry (PTV) which is used in experimental fluid dynamics to measure stream lines. To meet all of the specific requirements of this application, we developed a custom multi-step algorithm. The algorithm has the following steps: 1. particle detection, 2. frame-to-frame matching, 3. particle tracking, 4. gap stitching, and 5. filtering.

In step 1 (particle detection), particles in each video frame $1, 2, \ldots, n, \ldots, N$ are detected and their positions (x_i, y_i) recorded in *position lists*. In step 2 (frame-to-frame matching), the position lists of each pair of adjacent frames are compared for matches. First, the displacement vector from each particle in frame n to its nearest neighbor in $n+1$ is measured. The displacement vectors of all the particles that are in both images tend to be very similar, even if the microscope has slightly shifted between the frames, which makes this approach robust to instrument vibration and remove the need for prior image registration. Plotting all displacement vectors reveals a dense 'cloud' corresponding to matches, with several outliers corresponding to unmatched particles. To intelligently select the we use an efficient clustering algorithm (the mean shift clustering algorithm) with a low bandwidth (i.e., requiring cluster members to be very close) and select the largest cluster as those indicating matches. This operation provides a 'match list' on each pair of frames. This procedure is performed $N - 1$ times on each pair of adjacent frames, in preparation for the next step (Figure 5·8).

In step 3 (particle tracking), the list of $N - 1$ match lists are combined so as to track particles through the entire video. For example, if particle #11 in frame 1 is matched with particle #14 in frame 2, which is in turn matched with particle #9 in

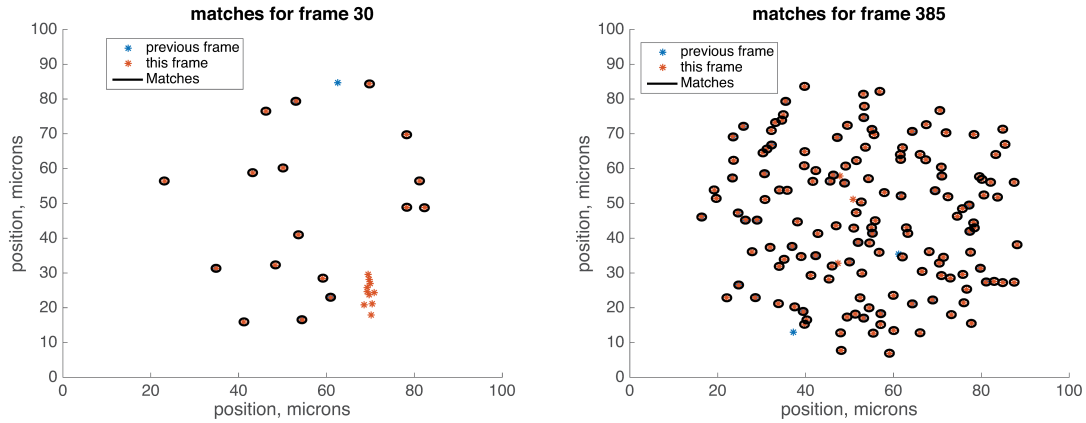

Figure 5·8: Two examples of particle matching results with (a) a relatively low number of particles and (b) a case with higher density. In the bottom-right corner of (a), a number of particles were detected close together in a line, in this frame but not the previous frame. This is most often observed when a particle floats by the surface without being immobilized, and is a source of variability.

frame 3, then the particle is tracked through frames 1-3. The result of this operation is a list of all particles in the entire experiment, with the corresponding frames in which it was found (e.g., 1-3) and its spatial coordinates in each frame (e.g., (x_1, y_1) through (x_3, y_3)).

Consider that if a particle is missed by the particle detection software in even just a single intermediate frame, it will appear to be two different particles after step 3, where a second particle will appear to bind immediately after a prior one debinds, in exactly the same position. In step 4 (gap stitching) these discrepancies are identified and repaired. An acceptable maximum gap length (e.g. 2 frames) must be provided. In the list generated in step 3, if any particle appears to have bound in just the same position as one which has just debound, these two particle list entries are combined or 'stitched' together.

The final step 6 (filtering) simply entails removing any particles from the list which are detected in only one frame. This greatly reduces the variability introduced by transient unbound particles, as described earlier.

5.3 Discrimination of DNA mismatches with digital melting analysis

The well-known phenomenon of RNA or DNA melting—whereby a double helix is destabilized and separates into two single strands above a threshold temperature—is a ubiquitous technique for controlling the hybridization state of nucleic acids. DNA melting is observed because the flexibility and conformational degrees of freedom (i.e. entropy) of the two single stranded nucleic acids contributes an energetic penalty to hybridization. This penalty increases with increasing solution temperature (recall that $\Delta G = \Delta H - T\Delta S$). The 'melting temperature' of a solution of double-stranded DNAs is defined as the temperature at which half of the DNA duplexes are double-stranded, and half are single-stranded at equilibrium. Below the melting temperature, the majority of the DNA will form duplexes, and above this temperature most will be single stranded.

The melting temperature of a duplex is a characteristic of the two nucleic acid sequences. The length of the double helix, the base pairs and even, to some extent, the order of the bases will effect the melting temperature because these properties change the total amount of hydrogen bonding in the duplex. 'Mismatched' duplexes —in which the two sequences are not reverse complementary—can be detected by measuring the DNA melting temperature. Mismatched duplexes have a measurably lower melting temperature than perfectly-matched sequences.

One important application of this concept in biotechnology is for identifying the presence of point mutations such as single-nucleotide polymorphisms (SNP, pronounced 'snip'). A SNP is a particular type of DNA mutation in which a single nucleotide is replaced with another. This can occur erroneously during DNA replication, for example, and can lead to a variety of different conditions and diseases including some types of cancer.

In any case, SNPs may be detected using a relatively simple technique called High Resolution Melt Analysis (HRMA) (Reed et al., 2007). In HRMA, the sample DNA is amplified and mixed with primers complementary to the target locus, as well as a dye which becomes more active when it has intercalated into double stranded DNA (Wittwer et al., 2003). The fluorescence of the sample is monitored as the temperature of the sample is slowly increased, to measure the melting curve. As mentioned earlier, melting curve and melting temperature for mismatched strands are slightly lower, which allows them to be detected (Figure 5·9).

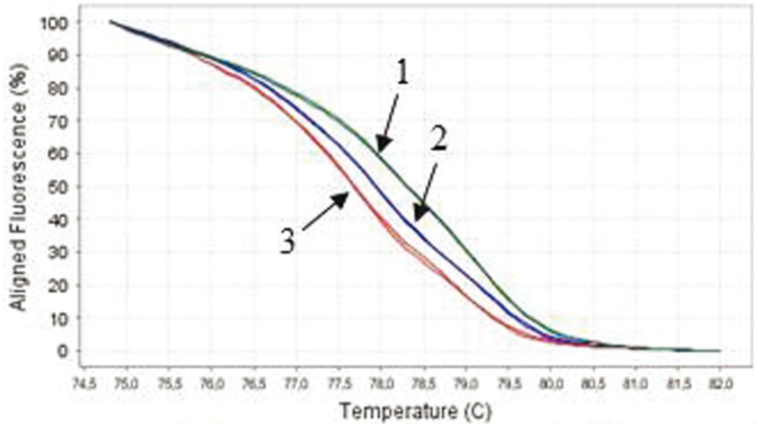

Figure 5·9: Examples of melting curves measured with HRMA, adapted from (Galbiati et al., 2013). The presence of a single mismatch slightly lowers the melting temperature (by up to 1.5 °C in this case). (1) Homozygous wild type (no mismatch), (2) heterozygous (50% mismatches), (3) homozygous mutant (100% mismatched).

5.3.1 A programmable and closed loop temperature control stage

HRMA has been applied to multiplexed sensors before, but not ones with the sensitivity of SP-IRIS (Wong and Melosh, 2010). We wished to apply the principle of HRMA to digital microarrays. While previous methods were able to identify the overall allele status of the whole sample, a digital microarray would be able to identify if even a small fraction of the total number of DNAs had mutations since the

sensitivity is much higher. To be able to perform 'digital melting analysis' we built a programmable, closed loop temperature control stage.

It was decided very early in the process that closed-loop control was an essential requirement. Since dehybridization is a kinetic process, control of the heating rate as well as the temperature set point were important. We were interested in pseudo-equilibrium conditions, so we needed to be able to very slowly increase the temperature over the course of hours at a rate of perhaps 1 °C per minute.

This meant however that a temperature control chamber that enclosed the entire microscope would not be accurate or precise enough for our application. This is because the microscope stage is built from aluminum and is relatively large (at least 200 g). Both aluminum and silicon are good thermal conductors, so the entire stage would have to be heated and then cooled, so reaching equilibrium would take place on the timescale of hours. Therefore, we decided to build a very small thermal stage that would fit in between the existing microscope stage and the chip. This 'thermal stage' would need to include a heat source and thermometer in a compact package. We decided to use a resistance thermometer to measure temperature due to their relative accuracy compared to thermocouples, and a thermoelectric (TE) element as the heater due to their rapid response and ability to perform active cooling as well as heating. The final assembly was built by gluing these two parts to a small milled aluminum part, which holds everything in place. The second prototype used a modified aluminum part had a set of drilled holes for holding the chip in place with partial vacuum (Figure 5·10).

We used an affordable PID temperature/process controller that supported serial communication with a computer (Omega Engineering model number CNiC16D-52), a single power MOSFET and a bench-top DC power supply to power the device (Figure 5·11 and Figure 5·12). The gate voltage of the MOSFET is set by the PID

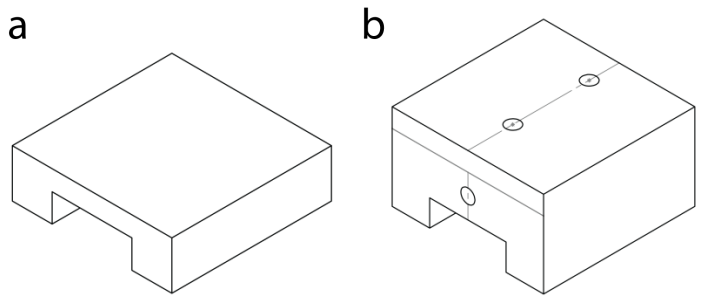

Figure 5·10: Drawings of the (a) first and (b) second versions of the milled aluminum thermal stage. The second version is slightly taller to incorporate internal vents for a vacuum chuck, which provides additional force to secure the chip.

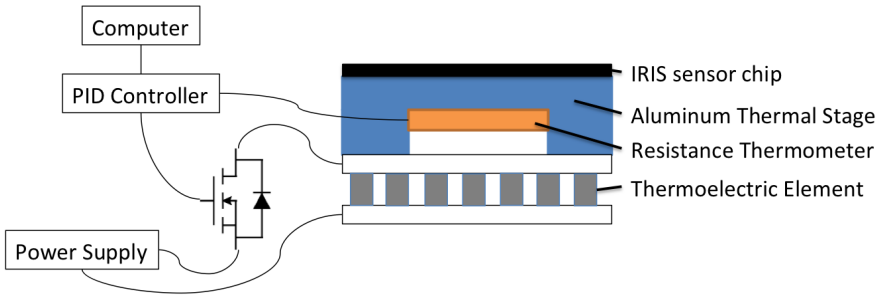

Figure 5·11: Schematic of the closed loop thermal control stage. The IRIS chip is placed on an aluminum thermal stage, which is heated from below by a TE element. The temperature of the stage is measured with an RTD thermometer, and the air gap between the TE element and the thermal stage is filled with thermal paste in the final design. The TE element receives current from a power supply, which is regulated by a power MOSFET that is gated by a PID controller. The controller communicates with a desktop computer, which can save the temperature history and update the set point.

controller. The maximum sustained current that the system can provide to the TE element is 10 A. The PID settings of the controller were calibrated to have a response time of about 5 seconds and an RMS variability <1 °C. We also wrote a LabVIEW virtual instrument to program the set point (e.g. perform a steady temperature ramp) and record the system temperature (Figure 5·13)

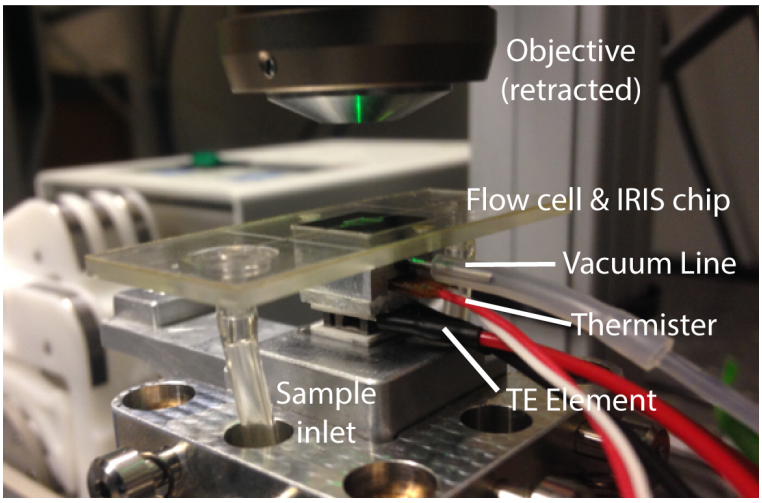

Figure 5·12: Photograph of the thermal stage, with various components labeled. The entire assembly including the TE element, chip and flow cell is about 1 cm tall.

Although the thermal stage was designed in such a way as to minimize the distance between the thermometer and the chip surface, it was very important for us to understand whether the measured temperature was an accurate reflection of the temperature of the chip (and the fluid) when the sample was under flow. Furthermore, we were interested in knowing if some upstream portion of the flow channel would not be usable because the fluid in that region had not yet reached the set temperature, and if this was the case, whether it could be mitigated by using a lower flow rate. To investigate these aspects we performed a series of non-isothermal flow simulations using COMSOL. The geometries of the thermal stage, the sensor chip and the microfluidic cartridge were generated using SolidWorks (Figure 5·14). Equi-

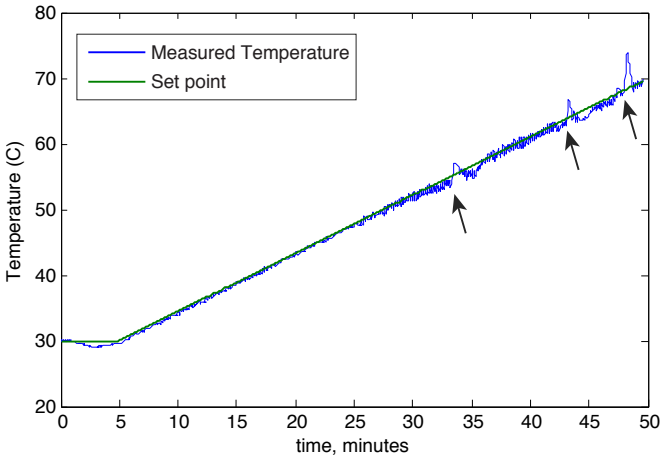

Figure 5·13: Example temperature data during a ramp from 30 °C to 70 °C over a 45 minute period. Arrows indicate times when the flow was momentarily stopped, and then re-started after one minute—suddenly stopping flow reduces the convective cooling of the chip and causes the temperature to overshoot, before settling.

librium as well as transient simulations were performed at the relatively high flow rate of 15 µl min^{-1}. The thermal boundary conditions applied to the stage are shown in Figure 5·15. Equilibrium simulations suggested that the temperature of the IRIS chip would be within 1 °C even at relatively high flow rates and high temperatures.

The results of the model indicated that even at high flow rates and high temperatures the temperature difference between the fluid channel and the RTD probe would be smaller than the temperature resolution of the probe, which is about 0.4 °C. We also simulated the transient behavior of the system, to see if the RTD would heat up before the IRIS chip. The results suggested that even during rapid heating (e.g., from 25 °C to 60 °C over three minutes) the temperature of the IRIS chip would stay about equal to that of the RTD element, which meant that the measured temperature would remain an accurate reflection of the true temperature of the chip (Figure 5·16).

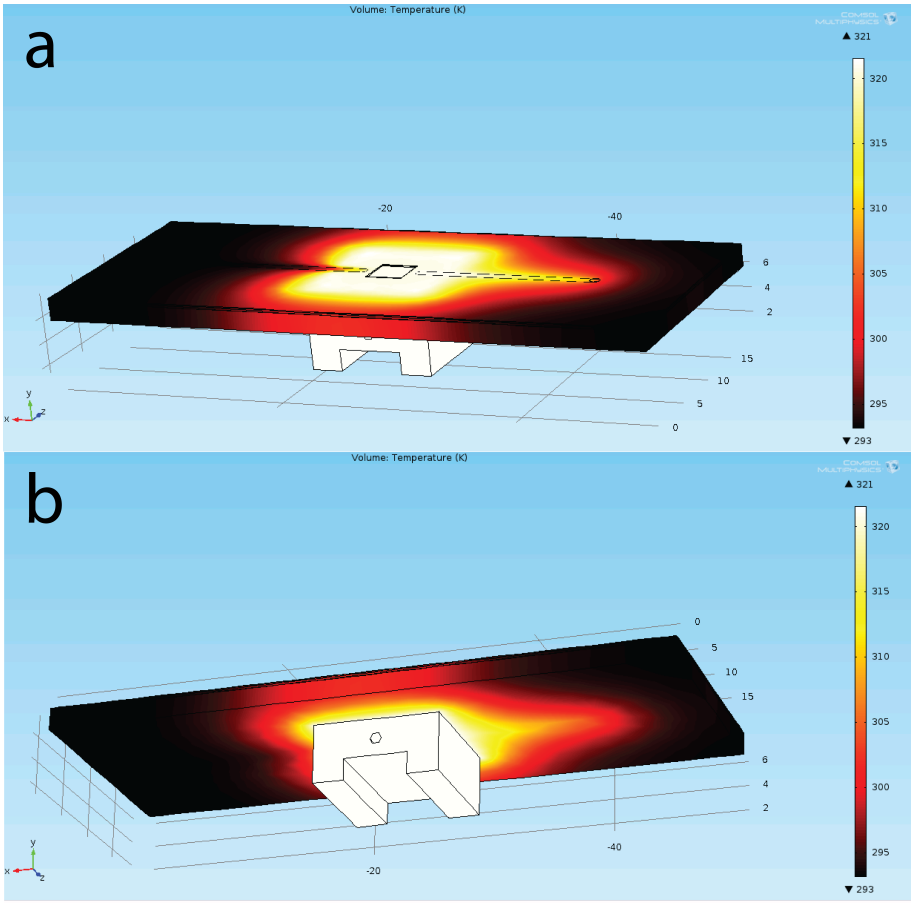

Figure 5·14: Overview of the multiphysics COMSOL model equilibrium solution, viewed (a) from above and (b) below. The entire geometry and material properties of the thermal stage, IRIS chip and microfluidic flow cell were accurately drawn using SolidWorks – even the internal holes for the vacuum line. The temperature at equilibrium is indicated by the heat map. The thermal stage is the hottest part of the system, while the edges of the flow cell are at about room temperature. The effect of convective cooling by the sample fluid is visible—it cools its surroundings before contacting the sensor chip (on the left), and heats them afterwards (on the right).

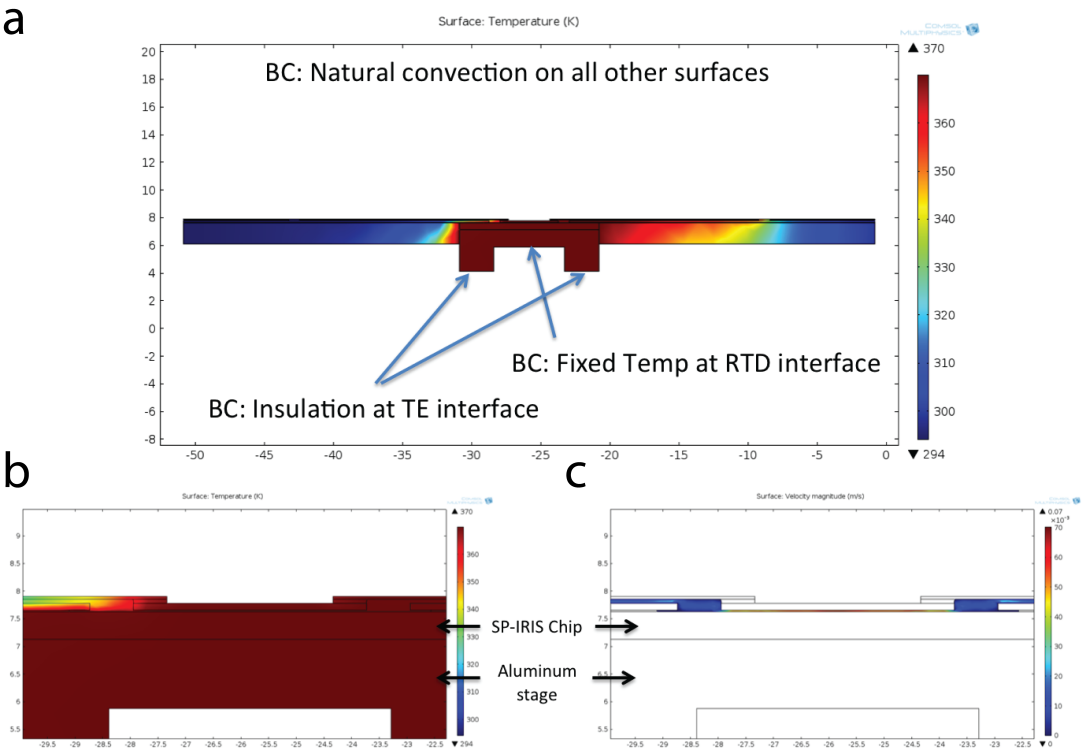

Figure 5·15: (a) Thermal boundary conditions used in the COMSOL model. (b) Equilibrium simulation results show that the sample fluid reaches approximately the same temperature as the IRIS chip almost instantly, even at relatively high temperatures and high flow rates. (c) A map of flow speeds shows the relative smallness of the liquid volume when it is contacting the chip (25 µm tall).

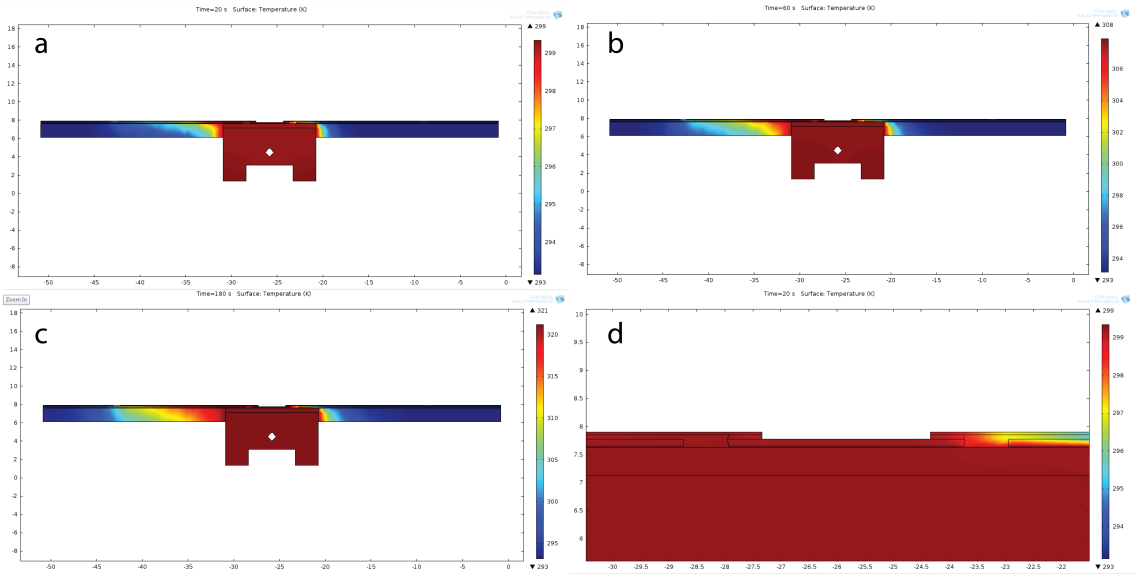

Figure 5·16: Transient simulations of the thermal stage during rapid heating, after (a) 20 seconds, (b) 60 seconds, and (c) 180 seconds. (d) A zoomed-in look at the chip at 20 seconds, showing that the fluid, IRIS chip and thermal stage are all at the same temperature even during rapid heating. Note that the scale of the thermal map increases over time: at 20 seconds $T_{max} = 299\,^{\circ}\mathrm{C}$, at 60 seconds $T_{max} = 308\,^{\circ}\mathrm{C}$ and at 180 seconds $T_{max} = 321\,^{\circ}\mathrm{C}$.

5.3.2 Mutation detection using digital melting analysis

To test the efficacy of this system at discriminating DNA mutations in a sample, we spotted two capture probes on an IRIS chip: one that was the reverse complement to the target ('perfect match'), and one that had a single base difference ('SNP mismatch'). We hybridized DNA-conjugated gold nanoparticles to the chip in a heterogeneous assay at room temperature, and then introduced a wash buffer. The temperature gradually increased at a rate of $1\,^{\circ}\mathrm{C\,min^{-1}}$ until the nanoparticles debound from the surface (Figure 5·17). The melting temperature of the nanoparticles from the perfect match spot was about 47 °C, and about 40 °C from the SNP mismatch spot.

This 7 °C difference between the melting temperatures is much larger than what is typically observed in HRMA—compare this to a 1.5 °C difference as in Figure 5·9. However, this assay was performed with the target sequence in excess, so it is likely that most nanoparticles had more than one double-stranded DNA link to the surface. The cooperative behavior of having multiple interactions greatly enhances their stability. This effect has been previously reported in the context of DNA-conjugated nanoparticles forming multiple duplexes with each other (Randeria et al., 2015; Xu and Craig, 2005). However, none of these studies investigated the single-linker case. This remains our objective for future work.

One challenge with this apparatus was the formation of bubbles in the flow cell. These bubbles disrupted imaging and could cause nanoparticles to be stripped from the spots if a bubble across them. We observed that the bubbles generally were not flowing through the solution but instead were nucleating on the chip surface, so we believed that they were likely caused by outgassing as the sample was heated by the chip. We found that most of the bubbles could be eliminated through sufficient outgassing, by simultaneously subjecting to vacuum and sonication for 5 minutes.

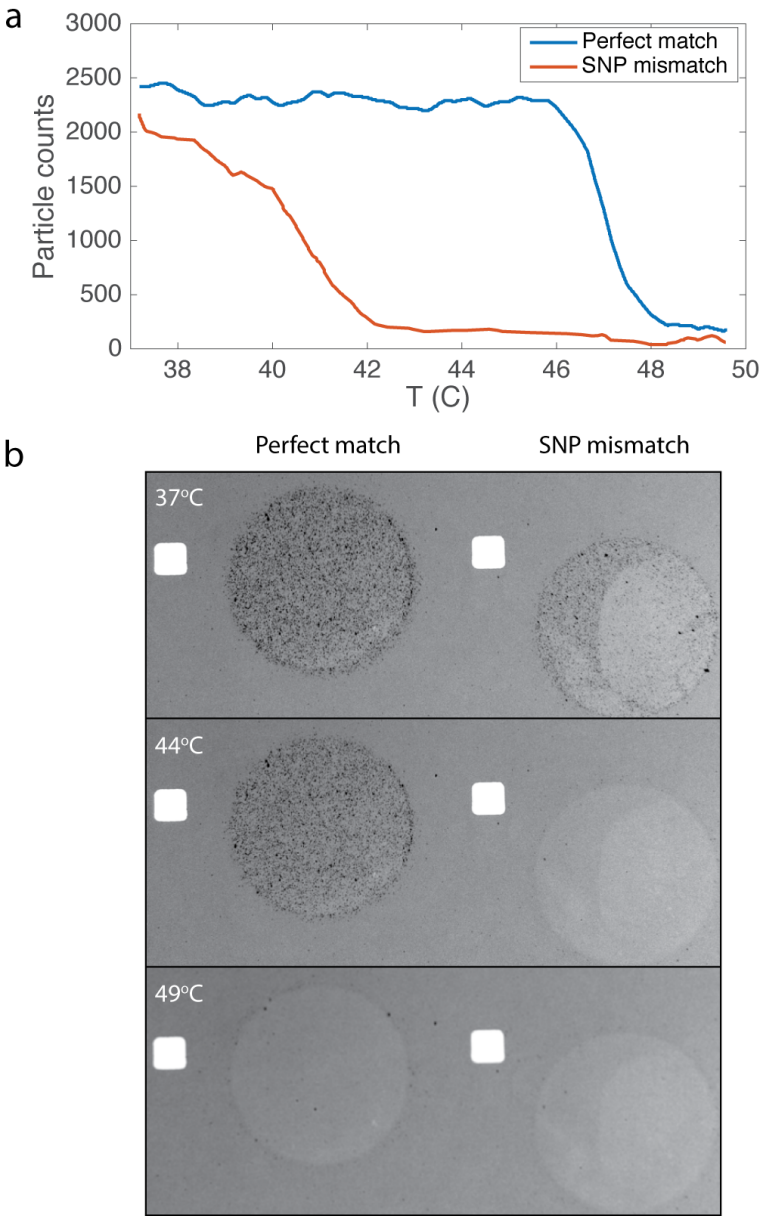

Figure 5·17: Demonstration of SNP mutation discrimination through melting analysis. (a) The melting curves of perfect match and single mismatch DNA-gold nanoparticle conjugates. (b) Example raw data images, at three temperatures. The perfect match spot is on the left, and the mis-match spot is on the right.

5.4 Conclusions

5.4.1 Summary

Kinetic, in-liquid measurements of nanoparticle binding have numerous advantages over endpoint measurements—they have lower variability and higher sensitivity, and they allow in-liquid imaging of delicate biological nanoparticles. We developed three technologies related to kinetic measurements of nanoparticle binding: a microfluidic flow cell, a closed loop thermal stage, and a robust algorithm for particle tracking.

The microfluidic flow cell was a necessary component to performing kinetics measurements, and it enabled sensitive real time measurements of virus binding. The viruses bound to the surface with very high affinity, and almost never debound after being captured. We hypothesized that this high affinity was the result of multiple antibodies binding cooperatively to each virus. When we performed similar experiments with gold nanoparticle-labeled DNA targets, on the other hand, we observed particle debinding. This debinding reduces sensitivity and increases resolution, since the sensor can quickly reach a reaction-limited equilibrium if the target is at a low concentration. We developed an algorithm to overcome this, which tracked particles through the video data and was able to identify when particles bound and debound from the surface. In addition to eliminating nearly all of the variability in the data, this algorithm significantly increased assay sensitivity. Furthermore, it allows the particle off rate to be measured simultaneously. We also showed that we could measure the off rate the usual way, by measuring the exponential decay in bound particles after introducing a wash buffer.

Finally, we described a thermal stage that was capable of providing closed loop and programmable temperature control. The thermal design required care since thermal gradients always exist even at equilibrium, and direct measurement of the sample temperature was impractical. We performed multiphysics simulations to thoroughly

evaluate the performance our design, and found that the IRIS chip and fluid sample would quickly reach about the same temperature as the measured temperature in our design even at relatively high flow rates. We showed proof of concept results in which we used the thermal stage to identify the allele status of a DNA sample by simultaneously measuring the melting curve on perfect match and SNP mismatch spots.

5.4.2 Future work

There are a number of applications for which the techniques described in this chapter are ready to be evaluated. One of them is kinetic measurements of digital microarrays for protein targets, rather than nucleic acids. As discussed in the previous chapter, digital microarrays for protein targets may have utility in biomedical research and clinical diagnostics. One potential challenge with protein microarrays is the lower affinity of antibody-antigen binding as compared to DNA-DNA hybridization. However as we have shown in this Chapter, this shortcoming may be somewhat mitigated by combining kinetic measurement and particle tracking.

We are also very interested in the continued study of the binding kinetics and thermodynamics of DNA-conjugated nanoparticles. Using the system developed here, a thorough investigation of the melting curve of DNA-nanoparticle conjugates can and should be conducted. In the work described here, we have only really demonstrated the technique's proof of concept. First, melting curves should be measured of DNA-nanoparticle conjugates tethered by only a single DNA-DNA interaction, such as in the digital microarray assays described in Chapter 4. Then, melting curves for perfect-matched and mismatched duplexes should be measured while varying duplex length, salt concentration, flow rate and the size of the particle itself, with the objective of maximizing the difference in the melting temperature between the two. This last variable is particularly interesting for assay design, since we are not aware of any

published literature of the effect of nanoparticle size on binding affinity of a single DNA-DNA linker (others have published regarding the case of multiple linkers, to the effect that larger particles have a flatter interface and therefore are able to form more links—but this is not the case in which we are interested). Finally, the prospect of using this platform to identify *rare* mutations should be investigated, using the optimal conditions identified during testing.

Chapter 6

Conclusion

6.1 Summary of dissertation

In this dissertation, we described the design and implementation of a digital microarray, which has several key advantages in sensitivity and dynamic range when compared to fluorescence microarrays. It is our hope that digital microarrays could eventually be of great utility in biomedical research and/or clinical diagnostics.

Chapter 2 described a quantitative approach to performing SP-IRIS imaging. We described how SP-IRIS may be used to approximately measure the scattered field of an unknown nanoparticle, and thereby calculate its size and aspect ratio. This approach will be helpful for characterizing biological nanoparticles such as viruses and exosomes with SP-IRIS in future applications.

This work also laid the groundwork for the development of a high throughput, polarization enhanced version of SP-IRIS described in Chapter 3. To our knowledge, it is fastest method yet developed for enumerating individual nanoparticles over a very large (square centimeter scale) area. The high-throughput nanoparticle detector is the enabling technology for digital microarrays since it provides single molecule detection without any penalty in multiplexing.

Chapter 4 describes the development of a digital microarray assay for nucleic acids, specifically mRNA biomarkers of antibiotic resistance. We described and justified the design of the probes, the assay and the various optimized hybridization and wash buffers, and compared the performance of the assay to the performance limits imposed

by mass transport and reaction kinetics.

Chapter 5 discusses three technologies which we developed to perform kinetic measurements of nanoparticle binding: a microfluidic flow cell, a nanoparticle tracking software and a temperature control stage. We showed how the first two technologies can drastically improve the sensitivity of real time assays, especially when the target molecule only binds weakly to the capture probe. We also showed preliminary results of 'digital melting analysis', in which we measured the melting curve of perfectly matched and SNP mismatched duplexes.

A final contribution of this dissertation which we wish to highlight is the implementation of a fast and accurate software model of nanoparticle imaging with SP-IRIS, described in Chapter 2. Our method utilizes a state-of-the-art implementation of the boundary element method (MNPBEM) to solve for the scattered far fields of nano-structures of arbitrary size, shape and material properties. Altogether, this software model of SP-IRIS the most comprehensive and accurate one our group has ever developed. It's also much faster and easier to use than previous modeling software, and we hope those interested in optical design and nanoparticle imaging will find it useful in their studies and future work.

6.2 Future directions

At the end of Chapter 4 we listed some steps that may be taken towards improving the assay even further, including sequence redesign and the development of a method for more accurate particle counting. However, these really only mark the end of the design phase and the beginning of the testing and qualification phase. Initially the limit of detection, dynamic range and specificity must be quantitatively measured. Specificity must be rigorously evaluated in a highly multiplexed context (i.e., hundreds of different probes). Later, the performance of the array must be benchmarked against

gold standard methods such as fluorescence arrays and quantitative PCR for low concentrations. Finally, protocols for raw sample preparation must be identified, tested and optimized.

The story is similar for the kinetic and thermodynamic measurement techniques described in Chapter 5. The nanoparticle tracking method is a relatively recent development. We have so far only really showed proof of concept of measuring DNA-nanoparticle conjugate affinity. Much more data should be acquired, especially of the kinetics and melting temperatures in solutions of different ionic concentration, in order to assemble a more complete thermodynamic picture. The ability to sense many different types of rare mutant alleles against a background of wild type sequences would be enormously valuable in cancer therapy monitoring, as we discussed in Section 5.1.2.

Finally, digital microarrays may very likely have utility for assaying molecules other than nucleic acids. Compared to nucleic acid assays, protein assays encompass a very wide range of potential diagnostic applications from infectious disease to allergies to cancer. We are currently evaluating the utility of digital microarrays as part of a diagnostic assay for hepatitis, that is based around protein biomarkers. The newness of digital microarrays suggests that we have probably not yet discovered its niche application, so we continue to keep an open mind.

Appendix A

The Single Particle Analysis and Detection (SPANDEX) software suite

A.1 Overview

The Single Particle Analysis and Detection Experience (SPANDEX) is an integrated suite of software tools that control the SP-IRIS instrument, analyze SP-IRIS image data and extract useful information from the results.

We were motivated to develop SPANDEX by the development of the high-throughput nanoparticle detection method described in Chapter 3. Previous software developed by our group was built with the assumption that each spot would always be imaged individually, with a high-magnification objective. It also assumed that all of the image data would be saved, and that the user would be able to tweak the particle detection software parameters for each image on a case by case basis. However, the new high throughput technique dozens of spots now fit within a single field of view, and 50 gigabytes of images were being acquired for each chip. This called for a new strategy.

SPANDEX has three components, which each consist a section of this appendix. Section A.2 describes the acquisition process. Section A.3 describes an analysis utility that converts acquisition results into useful information about a particular microarray study. Finally, Section A.4 describes two ImageJ plugins that perform particle detection and are used during the acquisition

A.2 Acquisition work flow

The first step of acquisition is simply taking images of the chip. Instead of saving these images, however, the images are immediately analyzed to find all of the particles and the position and properties of all particles is saved instead. This reduces the amount of saved data from gigabytes to kilobytes. Acquisition involves controlling the microscope itself (the cameras, stages and illumination) and also involves performing image processing. We decided to use the open-source microscope control tool Micro-manager (Edelstein et al., 2001). We developed the SPANDEX acquisition tool by augmenting Micro-Manager with custom hardware drivers, automation scripts, and image processing/particle detection plugins.

Once the incubation and wash steps of the assay are completed, the dry chip is loaded onto the microscope stage by hand with tweezers. Ensuring that the chip is correctly oriented and facing the operator is helpful but not required. The operator then moves the microscope (x, y, z) stage to the 'start' position, at which the top-left corner of the chip sensor area is visible and in focus on the Micro-manager Live Preview window. Next, the operator runs the *SPANDEX Endpoint Area Scan* script, and uses the input dialog to set various parameters such as the image save directory and scan area, and also the type of particle of interest (i.e., gold nanorod vs. biological nanoparticle). The script then instructs the operator to manually set the polarization optics to their appropriate settings based on this information. When this is completed the scan begins.

During the scan procedure, the total scan area is subdivided into a grid of tiles, each the size of the microscope field of view. First, the planarity of the chip is determined by performing an auto-focus algorithm in four corners of the chip. The nominal plane of focus of each tile is calculated through linear interpolation (Figure A·1)

The acquisition script performs three steps at each tile position. First, it acquires

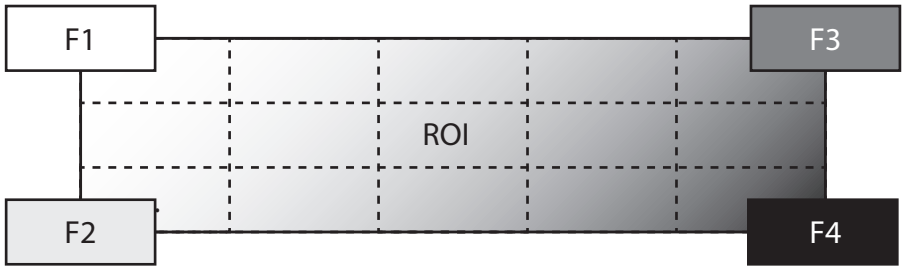

Figure A·1: Schematic of tiled acquisition. If the region of interest (ROI) is larger than a single field of view, it subdivided into a grid of tiles. The focus position of each tile is determined by first focusing in the four corners F1–F4, then interpolating. The gradient across the ROI is meant to visually suggest that the substrate is slightly tilted.

a z-stack of images by taking between 11 and 21 frames across a fixed intervals. To reduce shot noise, the microscope may actually acquire between 1 and 64 frames at each z position. Typically, about 120 frames are acquired for each tile during this step in about 20 seconds, but scans for very dim particles such as exosomes can take as long as 2 minutes.

Next, the particles in the image are detected using the ImageJ plugin described in Section A.4. The particle detection parameters are automatically selected based on the type of particle selected earlier by the operator. This step usually takes between 10-20 seconds (the time increases approximately linearly with the number of frames in the z-stack).

Finally, the information about the detected particles is combined with the information about particles in other tiles into a single global coordinate system. The tiles do not overlap, and we ignore small differences between the (x, y) stage set position and the actual position of the stages (this is typically less than 10 µm).

When acquisition is complete, the global map of particle positions is saved in a particle data file, with the (x, y) position of each particle written to a different line of the file as comma separated values.

As a visual aid for later analysis, the acquisition script actually does one additional step. Images are acquired at each tile position and combined to form a large overall 'preview' image (e.g., Figure 4·10. The particle data file and the preview image are saved together in the file path selected by the operator, and are ready for further analysis.

A.3 Particle counting utility

By themselves, the particle data file and preview image saved during acquisition do not provide useful information about the actual assay: the number of particles within each spot must be determined. SPANDEX includes a particle counting utility in MATLAB which segments each spot in the preview image and counts all the particles within each spot.

The utility first prompts the user to load the preview image and the particle data file, as well as some parameters about the microarray such as the number of spots and the distance between them (Figure A·2).

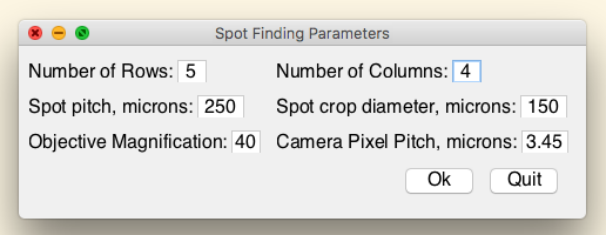

Figure A·2: The operator prompt for the MATLAB particle counting utility.

The utility uses this information to naively guess the location of the spot boundaries. The size, shape and position of each spot boundary can be adjusted manually (Figure A·3).

Once the spot boundaries have been adjusted the particles within each region are tallied (Figure A·4). These results are then immediately available for further

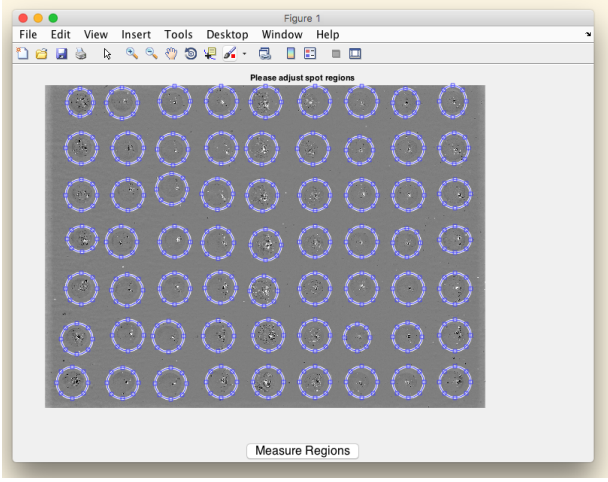

Figure A·3: Selection of spot regions. The original spot regions are placed on the grid using the parameters from the prompt in Figure A·2, but can be individually moved and resized by the operator during this step.

statistical analysis or data visualization with MATLAB (Figure A·5).

A.4 Particle detection plugin

In Chapter 2 we introduced the concept of the *Normalized Intensity Range* (NIR) as an approximate measurement of the amplitude of the scattered field of a given particle. Essentially, the NIR is measured by simply taking the difference between the maximum and minimum value of each (x, y) pixel position in the z-stack. A threshold is then be applied to the resulting NIR image, to identify any regions in the image where the NIR is greater than a cutoff value. Provided that particles are far enough apart on the surface that their images do not overlap, then the number of blobs after the thresholding operation is the number of particles in the image.

This minimal implementation is not robust to various sources of variability. Illumination gradients and shot noise degrade the quality of the measurement, and particle crowding and debris in the image cause false negatives and false positives. Table A.1 briefly summarizes the various strategies used to improve the accuracy and

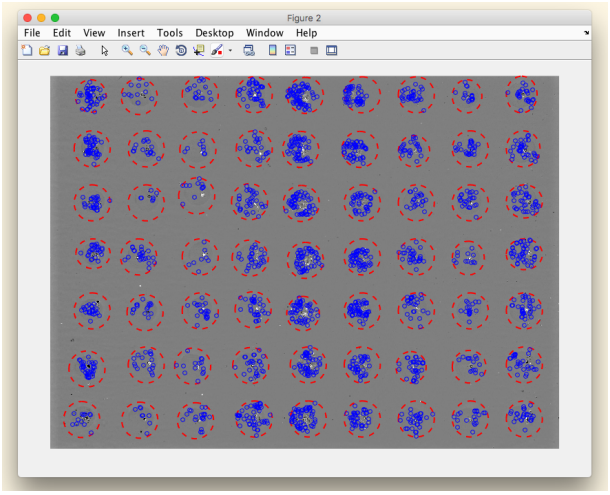

Figure A·4: Particle counting within spot regions. Spot regions defined in the previous step are indicated by red dashed lines, and particles within each region are plotted with small blue circles.

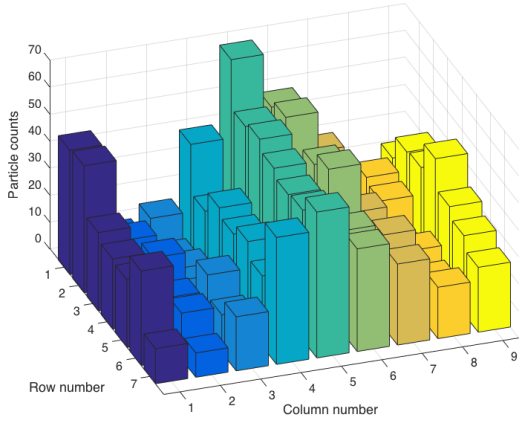

Figure A·5: Example visualization of results. In this case spots in each column are replicates, and are colored accordingly.

Variability Type	Strategy
Illumination gradient	Median image normalization
Shot noise	Gaussian convolution (smoothing)
Particle crowding (false negatives)	Weiner deconvolution and morphological operations
Debris (false positives)	Morphological operations, filtering blob size & shape

Table A.1: A summary of the different types of noise and variability in particle detection, and the strategies used to mitigate them.

robustness of the particle detection plugin.

References

Alhasan, A. H., Kim, D. Y., Daniel, W. L., Watson, E., Meeks, J. J., Thaxton, C. S., and Mirkin, C. A. (2012). Scanometric microrna array profiling of prostate cancer markers using spherical nucleic acid-gold nanoparticle conjugates. *Analytical Chemistry*, 84(9):4153–4160.

Avci, O., Adato, R., Ozkumur, A. Y., and Ünlü, M. S. (2016). Physical modeling of interference enhanced imaging and characterization of single nanoparticles. *Optics Express*, 24(6):6094.

Avci, O., Campana, M. I., Yurdakul, C., and Ünlü, M. S. (2017). Pupil function engineering for enhanced nanoparticle visibility in wide-field interferometric microscopy. *Optica*, 4(2):247–254.

Baker, M. (2012). Digital pcr hits its stride. *Nature Methods*, 9(6):541–544.

Barczak, A. K., Gomez, J. E., Kaufmann, B. B., Hinson, E. R., Cosimi, L., Borowsky, M. L., Onderdonk, A. B., Stanley, S. A., Kaur, D., Bryant, K. F., Knipe, D. M., Sloutsky, A., and Hung, D. T. (2012). Rna signatures allow rapid identification of pathogens and antibiotic susceptibilities. *Proceedings of the National Academy of Sciences*, 109(16):6217–6222.

Belosludtsev, Y., Belosludtsev, I., Iverson, B., Lemeshko, S., Wiese, R., Hogan, M., and Powdrill, T. (2001). Nearly instantaneous, cation-independent, high selectivity nucleic acid hybridization to dna microarrays. *Biochemical and Biophysical Research Communications*, 282(5):1263–1267.

Berthoux, L., Pèchoux, C., and Darlix, J.-L. (1999). Multiple effects of an anti-human immunodeficiency virus nucleocapsid inhibitor on virus morphology and replication. *Journal of Virology*, 73(12):10000–10009.

Binder, H. (2006). Thermodynamics of competitive surface adsorption on dna microarrays. *Journal of Physics: Condensed Matter*, 18(18):S491.

Boccara, M., Fedala, Y., Bryan, C. V., Bailly-Bechet, M., Bowler, C., and Boccara, A. C. (2016). Full-field interferometry for counting and differentiating aquatic biotic nanoparticles: from laboratory to tara oceans. *Biomedical Optics Express*, 7(9):3736–3746.

Bohren, C. F. and Huffman, D. R. (2008). *Absorption and Scattering of Light by Small Particles*. John Wiley & Sons.

Büttner, A. and Zeitner, U. D. (2002). Wave optical analysis of light-emitting diode beam shaping using microlens arrays. *Optical Engineering*, 41(10):2393–2401.

Carlon, E. and Heim, T. (2006). Thermodynamics of rna/dna hybridization in high-density oligonucleotide microarrays. *Physica A: Statistical Mechanics and its Applications*, 362(2):433–449.

Chen, C., Wang, W., Ge, J., and Zhao, X. S. (2009). Kinetics and thermodynamics of dna hybridization on gold nanoparticles. *Nucleic Acids Research*, 37(11):3756–3765.

Chen, W. W., Balaj, L., Liau, L. M., Samuels, M. L., Kotsopoulos, S. K., Maguire, C. A., LoGuidice, L., Soto, H., Garrett, M., Zhu, L. D., Sivaraman, S., Chen, C., Wong, E. T., Carter, B. S., Hochberg, F. H., Breakefield, X. O., and Skog, J. (2013). Beaming and droplet digital pcr analysis of mutant idh1 mrna in glioma patient serum and cerebrospinal fluid extracellular vesicles. *Molecular Therapy - Nucleic Acids*, 2(7):e109.

Choi, N. W., Kim, J., Chapin, S. C., Duong, T., Donohue, E., Pandey, P., Broom, W., Hill, W. A., and Doyle, P. S. (2012). Multiplexed detection of mrna using porosity-tuned hydrogel microparticles. *Analytical Chemistry*, 84(21):9370–9378.

Clavel, F. and Orenstein, J. M. (1990). A mutant of human immunodeficiency virus with reduced rna packaging and abnormal particle morphology. *Journal of Virology*, 64(10):5230–5234.

Daaboul, G. G., Gagni, P., Benussi, L., Bettotti, P., Ciani, M., Cretich, M., Freedman, D. S., Ghidoni, R., Ozkumur, A. Y., Piotto, C., Prosperi, D., Santini, B., Ünlü, M. S., and Chiari, M. (2016). Digital detection of exosomes by interferometric imaging. *Scientific Reports*, 6:37246.

Daaboul, G. G., Lopez, C. A., Chinnala, J., Goldberg, B. B., Connor, J. H., and Ünlü, M. S. (2014). Digital sensing and sizing of vesicular stomatitis virus pseudotypes in complex media: A model for ebola and marburg detection. *ACS Nano*, 8(6):6047–6055.

Daaboul, G. G., Yurt, A., Zhang, X., Hwang, G. M., Goldberg, B. B., and Ünlü, M. S. (2010). High-throughput detection and sizing of individual low-index nanoparticles and viruses for pathogen identification. *Nano Letters*, 10(11):4727–4731.

Dancer, S. J. (2014). Controlling hospital-acquired infection: Focus on the role of the environment and new technologies for decontamination. *Clinical Microbiology Reviews*, 27(4):665–690.

Diaz Jr, L. A., Williams, R. T., Wu, J., Kinde, I., Hecht, J. R., Berlin, J., Allen, B., Bozic, I., Reiter, J. G., Nowak, M. A., Kinzler, K. W., Oliner, K. S., and Vogelstein, B. (2012). The molecular evolution of acquired resistance to targeted egfr blockade in colorectal cancers. *Nature*, 486(7404):537–540.

Diehl, F., Li, M., He, Y., Kinzler, K. W., Vogelstein, B., and Dressman, D. (2006). Beaming: single-molecule pcr on microparticles in water-in-oil emulsions. *Nature Methods*, 3(7):551–559.

Dirks, R., Bois, J., Schaeffer, J., Winfree, E., and Pierce, N. (2007). Thermodynamic analysis of interacting nucleic acid strands. *SIAM Review*, 49(1):65–88.

Doane, F. W. (1980). Virus morphology as an aid for rapid diagnosis. *The Yale Journal of Biology and Medicine*, 53(1):19–25.

Dragovic, R. A., Gardiner, C., Brooks, A. S., Tannetta, D. S., Ferguson, D. J. P., Hole, P., Carr, B., Redman, C. W. G., Harris, A. L., Dobson, P. J., Harrison, P., and Sargent, I. L. (2011). Sizing and phenotyping of cellular vesicles using nanoparticle tracking analysis. *Nanomedicine: Nanotechnology, Biology and Medicine*, 7(6):780–788.

Edelstein, A., Amodaj, N., Hoover, K., Vale, R., and Stuurman, N. (2001). Computer control of microscopes using manager. In *Current Protocols in Molecular Biology*. John Wiley & Sons, Inc.

Fernandes, M. X., Ortega, A., Lo Martinez, M. C., and de la Torre, J. G. (2002). Calculation of hydrodynamic properties of small nucleic acids from their atomic structure. *Nucleic Acids Research*, 30(8):1782–1788.

Filipe, V., Hawe, A., and Jiskoot, W. (2010). Critical evaluation of nanoparticle tracking analysis (nta) by nanosight for the measurement of nanoparticles and protein aggregates. *Pharmaceutical Research*, 27(5):796–810.

Forshew, T., Murtaza, M., Parkinson, C., Gale, D., Tsui, D. W. Y., Kaper, F., Dawson, S.-J., Piskorz, A. M., Jimenez-Linan, M., Bentley, D., Hadfield, J., May, A. P., Caldas, C., Brenton, J. D., and Rosenfeld, N. (2012). Noninvasive identification and monitoring of cancer mutations by targeted deep sequencing of plasma dna. *Science Translational Medicine*, 4(136):136ra68–136ra68.

Galbiati, S., Damin, F., Pinzani, P., Mancini, I., Vinci, S., Chiari, M., Orlando, C., Cremonesi, L., and Ferrari, M. (2013). A new microarray substrate for ultrasensitive genotyping of kras and braf gene variants in colorectal cancer. *PLoS ONE*, 8(3):e59939.

García de Abajo, F. J. (2002). Retarded field calculation of electron energy loss in inhomogeneous dielectrics. *Physical Review B*, 65(11).

Gardiner, C., Shaw, M., Hole, P., Smith, J., Tannetta, D., Redman, C. W., and Sargent, I. L. (2014). Measurement of refractive index by nanoparticle tracking analysis reveals heterogeneity in extracellular vesicles. *Journal of Extracellular Vesicles*, 3.

Gong, P. and Levicky, R. (2008). Dna surface hybridization regimes. *Proceedings of the National Academy of Sciences*, 105(14):5301–5306.

Hill, H. D. and Mirkin, C. A. (2006). The bio-barcode assay for the detection of protein and nucleic acid targets using dtt-induced ligand exchange. *Nature Protocols*, 1(1):324–336.

Ho, J. Y., Cira, N. J., Crooks, J. A., Baeza, J., and Weibel, D. B. (2012). Rapid identification of eskape bacterial strains using an autonomous microfluidic device. *PLOS ONE*, 7(7):e41245.

Hohenester, U. and Trügler, A. (2012). Mnpbem - a matlab toolbox for the simulation of plasmonic nanoparticles. *Computer Physics Communications*, 183(2):370–381.

Hurst, S. J., Lytton-Jean, A. K. R., and Mirkin, C. A. (2006). Maximizing dna loading on a range of gold nanoparticle sizes. *Analytical Chemistry*, 78(24):8313–8318.

Im, H., Shao, H., Park, Y. I., Peterson, V. M., Castro, C. M., Weissleder, R., and Lee, H. (2014). Label-free detection and molecular profiling of exosomes with a nano-plasmonic sensor. *Nature biotechnology*, 32(5):490–495.

Janku, F. (2014). Tumor heterogeneity in the clinic: is it a real problem? *Therapeutic Advances in Medical Oncology*, 6(2):43–51.

Jin, R., Wu, G., Li, Z., Mirkin, C. A., and Schatz, G. C. (2003). What controls the melting properties of dna-linked gold nanoparticle assemblies? *Journal of the American Chemical Society*, 125(6):1643–1654.

Kourembanas, S. (2015). Exosomes: Vehicles of intercellular signaling, biomarkers, and vectors of cell therapy. *Annual Review of Physiology*, 77(1):13–27.

Kukura, P., Ewers, H., Müller, C., Renn, A., Helenius, A., and Sandoghdar, V. (2009). High-speed nanoscopic tracking of the position and orientation of a single virus. *Nature Methods*, 6(12):923–927.

Kuznetsov, Y. G., Victoria, J. G., Robinson, W. E., and McPherson, A. (2003). Atomic force microscopy investigation of human immunodeficiency virus (hiv) and hiv-infected lymphocytes. *Journal of Virology*, 77(22):11896–11909.

Lange, F. d., Cambi, A., Huijbens, R., Bakker, B. d., Rensen, W., Garcia-Parajo, M., Hulst, N. v., and Figdor, C. G. (2001). Cell biology beyond the diffraction limit: near-field scanning optical microscopy. *Journal of Cell Science*, 114(23):4153–4160.

Lawrence, C. M., Menon, S., Eilers, B. J., Bothner, B., Khayat, R., Douglas, T., and Young, M. J. (2009). Structural and functional studies of archaeal viruses. *The Journal of Biological Chemistry*, 284(19):12599–12603.

Le Goff, G. C., Srinivas, R. L., Hill, W. A., and Doyle, P. S. (2015). Hydrogel microparticles for biosensing. *European Polymer Journal*, 72:386–412.

Lee, H. H., Molla, M. N., Cantor, C. R., and Collins, J. J. (2010). Bacterial charity work leads to population-wide resistance. *Nature*, 467(7311):82–85.

Li, G., Zhu, L., Wu, Z., He, Y., Tan, H., and Sun, S. (2016). Digital concentration readout of dna by absolute quantification of optically countable gold nanorods. *Analytical Chemistry*, 88(22):10994–11000.

Li, L., Qu, X., Sun, J., Yang, M., Song, B., Shao, Q., Zhang, X., and Jin, W. (2011). Single-molecule-counting protein microarray assay with nanoliter samples and its application in the dynamic protein expression of living cells. *Biosensors and Bioelectronics*, 26(8):3688–3691.

Liang, R.-Q., Li, W., Li, Y., Tan, C.-y., Li, J.-X., Jin, Y.-X., and Ruan, K.-C. (2005). An oligonucleotide microarray for microrna expression analysis based on labeling rna with quantum dot and nanogold probe. *Nucleic Acids Research*, 33(2):e17–e17.

Lichty, B. D., Power, A. T., Stojdl, D. F., and Bell, J. C. (2004). Vesicular stomatitis virus: re-inventing the bullet. *Trends in Molecular Medicine*, 10(5):210–216.

Lindfors, K., Kalkbrenner, T., Stoller, P., and Sandoghdar, V. (2004). Detection and spectroscopy of gold nanoparticles using supercontinuum white light confocal microscopy. *Physical Review Letters*, 93(3):037401.

Luepke, K. H., Suda, K. J., Boucher, H., Russo, R. L., Bonney, M. W., Hunt, T. D., and Mohr, J. F. (2017). Past, present, and future of antibacterial economics: Increasing bacterial resistance, limited antibiotic pipeline, and societal implications. *Pharmacotherapy: The Journal of Human Pharmacology and Drug Therapy*, 37(1):71–84.

Lytton-Jean, A. K. R. and Mirkin, C. A. (2005). A thermodynamic investigation into the binding properties of dna functionalized gold nanoparticle probes and molecular fluorophore probes. *Journal of the American Chemical Society*, 127(37):12754–12755.

Madden, T. (2003). *The BLAST Sequence Analysis Tool*. National Center for Biotechnology Information (US).

Malutan, R. and Vilda, P. G. (2012). Thermodynamics of microarray hybridization. In *Thermodynamics - Fundamentals and Its Application in Science*. InTech Open Access Publisher.

Mandel, L. and Wolf, E. (1995). *Optical Coherence and Quantum Optics*. Cambridge University Press.

Misale, S., Yaeger, R., Hobor, S., Scala, E., Janakiraman, M., Liska, D., Valtorta, E., Schiavo, R., Buscarino, M., Siravegna, G., Bencardino, K., Cercek, A., Chen, C.-T., Veronese, S., Zanon, C., Sartore-Bianchi, A., Gambacorta, M., Gallicchio, M., Vakiani, E., Boscaro, V., Medico, E., Weiser, M., Siena, S., Di Nicolantonio, F., Solit, D., and Bardelli, A. (2012). Emergence of kras mutations and acquired resistance to anti-egfr therapy in colorectal cancer. *Nature*, 486(7404):532–536.

Mitra, A., Ignatovich, F., and Novotny, L. (2012). Real-time optical detection of single human and bacterial viruses based on dark-field interferometry. *Biosensors and Bioelectronics*, 31(1):499–504.

Mitra, A. and Novotny, L. (2013). Real-time optical detection of single nanoparticles and viruses using heterodyne interferometry. In Bartolo, B. D. and Collins, J., editors, *Nano-Optics for Enhancing Light-Matter Interactions on a Molecular Scale*, NATO Science for Peace and Security Series B: Physics and Biophysics, pages 3–22. Springer Netherlands.

Monroe, M. R., Daaboul, G. G., Tuysuzoglu, A., Lopez, C. A., Little, F. F., and Ünlü, M. S. (2013). Single nanoparticle detection for multiplexed protein diagnostics with attomolar sensitivity in serum and unprocessed whole blood. *Analytical Chemistry*, 85(7):3698–3706.

Morency-Potvin, P., Schwartz, D. N., and Weinstein, R. A. (2017). Antimicrobial stewardship: How the microbiology laboratory can right the ship. *Clinical Microbiology Reviews*, 30(1):381–407.

Nie, S. and Emory, S. R. (1997). Probing single molecules and single nanoparticles by surface-enhanced raman scattering. *Science*, 275(5303):1102–1106.

Nkodo, A. E., Garnier, J. M., Tinland, B., Ren, H., Desruisseaux, C., McCormick, L. C., Drouin, G., and Slater, G. W. (2001). Diffusion coefficient of dna molecules during free solution electrophoresis. *Electrophoresis*, 22(12):2424–2432.

Novotny, L. and Hecht, B. (2006). *Principles of nano-optics*. Cambridge University Press, Cambridge.

Oikonomopoulos, A., Polytarchou, C., Joshi, S., Hommes, D. W., and Iliopoulos, D. (2016). Identification of circulating microrna signatures in crohns disease using the nanostring ncounter technology:. *Inflammatory Bowel Diseases*, 22(9):2063–2069.

Ozkumur, E., Ahn, S., Yalcin, A., Lopez, C. A., Cevik, E., Irani, R. J., DeLisi, C., Chiari, M., and Ünlü, M. S. (2010). Label-free microarray imaging for direct detection of dna hybridization and single-nucleotide mismatches. *Biosensors and Bioelectronics*, 25(7):1789–1795.

Ozkumur, E., Yalcin, A., Cretich, M., Lopez, C. A., Bergstein, D. A., Goldberg, B. B., Chiari, M., and Ünlü, M. S. (2009). Quantification of dna and protein adsorption by optical phase shift. *Biosensors and Bioelectronics*, 25(1):167–172.

Palomba, G., Colombino, M., Contu, A., Massidda, B., Baldino, G., Pazzola, A., Ionta, M., Capelli, F., Trova, V., Sedda, T., Sanna, G., Tanda, F., Budroni, M., Palmieri, G., and Cossu, A. (2012). Prevalence of kras, braf, and pik3ca somatic mutations in patients with colorectal carcinoma may vary in the same population: clues from sardinia. *Journal of Translational Medicine*, 10:178.

Patskovsky, S. and Meunier, M. (2015). Reflected light microspectroscopy for single-nanoparticle biosensing. *Journal of Biomedical Optics*, 20(9):097001–097001.

Peterson, A. W., Heaton, R. J., and Georgiadis, R. M. (2001). The effect of surface probe density on dna hybridization. *Nucleic Acids Research*, 29(24):5163–5168.

Randeria, P. S., Jones, M. R., Kohlstedt, K. L., Banga, R. J., Olvera de la Cruz, M., Schatz, G. C., and Mirkin, C. A. (2015). What controls the hybridization thermodynamics of spherical nucleic acids? *Journal of the American Chemical Society*, 137(10):3486–3489.

Reddington, A., Trueb, J., Freedman, D., Tuysuzoglu, A., Daaboul, G., Lopez, C., Karl, W., Connor, J., Fawcett, H., and Ünlü, M. (2013). An interferometric reflectance imaging sensor for point of care viral diagnostics. *IEEE Transactions on Biomedical Engineering*, 60(12):3276–3283.

Reed, G. H., Kent, J. O., and Wittwer, C. T. (2007). High-resolution dna melting analysis for simple and efficient molecular diagnostics. *Pharmacogenomics*, 8(6):597–608.

Risinger, A. and Williams, C. (2006). Scanarray gx plus/proscanarray competitive performance analysis using a commercial test slide. Application note, Perkin Elmer, Boston, MA.

Saleh, B. E. A. and Teich, M. C. (2007). *Fundamentals of photonics*. Wiley series in pure and applied optics. Wiley Interscience, Hoboken, N.J, 2nd ed edition.

Scherr, S. M., Daaboul, G. G., Trueb, J., Sevenler, D., Fawcett, H., Goldberg, B., Connor, J. H., and Ünlü, M. S. (2016). Real-time capture and visualization of individual viruses in complex media. *ACS Nano*, 10(2):2827–2833.

Shi, L., Reid, L. H., Jones, W. D., Shippy, R., Warrington, J. A., Baker, S. C., Collins, P. J., Longueville, F. d., Kawasaki, E. S., Lee, K. Y., Luo, Y., Sun, Y. A., Willey, J. C., Setterquist, R. A., Fischer, G. M., Tong, W., Dragan, Y. P., Dix, D. J., Frueh, F. W., Goodsaid, F. M., Herman, D., Jensen, R. V., Johnson, C. D., Lobenhofer, E. K., Puri, R. K., Scherf, U., Thierry-Mieg, J., Wang, C., Wilson, M., Wolber, P. K., Zhang, L., Amur, S., Bao, W., Barbacioru, C. C., Lucas, A. B., Bertholet, V., Boysen, C., Bromley, B., Brown, D., Brunner, A., Canales, R., Cao, X. M., Cebula, T. A., Chen, J. J., Cheng, J., Chu, T.-M., Chudin, E., Corson, J., Corton, J. C., Croner, L. J., Davies, C., Davison, T. S., Delenstarr, G., Deng, X., Dorris, D., Eklund, A. C., Fan, X.-h., Fang, H., Fulmer-Smentek, S., Fuscoe, J. C., Gallagher, K., Ge, W., Guo, L., Guo, X., Hager, J., Haje, P. K., Han, J., Han, T., Harbottle, H. C., Harris, S. C., Hatchwell, E., Hauser, C. A., Hester, S., Hong, H., Hurban, P., Jackson, S. A., Ji, H., Knight, C. R., Kuo, W. P., LeClerc, J. E., Levy, S., Li, Q.-Z., Liu, C., Liu, Y., Lombardi, M. J., Ma, Y., Magnuson, S. R., Maqsodi, B., McDaniel, T., Mei, N., Myklebost, O., Ning, B., Novoradovskaya, N., Orr, M. S., Osborn, T. W., Papallo, A., Patterson, T. A., Perkins, R. G., Peters, E. H., Peterson, R., Philips, K. L., Pine, P. S., Pusztai, L., Qian, F., Ren, H., Rosen, M., Rosenzweig, B. A., Samaha, R. R., Schena, M., Schroth, G. P., Shchegrova, S., Smith, D. D., Staedtler, F., Su, Z., Sun, H., Szallasi, Z., Tezak, Z., Thierry-Mieg, D., Thompson, K. L., Tikhonova, I., Turpaz, Y., Vallanat, B., Van, C., Walker, S. J., Wang, S. J., Wang, Y., Wolfinger, R., Wong, A., Wu, J., Xiao, C., Xie, Q., Xu, J., Yang, W., Zhang, L., Zhong, S., Zong, Y., and Slikker, W. (2006). The microarray quality control (maqc) project shows inter- and intraplatform reproducibility of gene expression measurements. *Nature Biotechnology*, 24(9):1151–1161.

Sorgenfrei, S., Chiu, C.-y., Jr, R. L. G., Yu, Y.-J., Kim, P., Nuckolls, C., and Shepard, K. L. (2011). Label-free single-molecule detection of dna-hybridization kinetics with a carbon nanotube field-effect transistor. *Nature Nanotechnology*, 6(2):126–132.

Squires, T. M., Messinger, R. J., and Manalis, S. R. (2008). Making it stick: convection, reaction and diffusion in surface-based biosensors. *Nature Biotechnology*, 26(4):417–426.

Taton, T. A., Mirkin, C. A., and Letsinger, R. L. (2000). Scanometric dna array detection with nanoparticle probes. *Science*, 289(5485):1757–1760.

Tinland, B., Pluen, A., Sturm, J., and Weill, G. (1997). Persistence length of single-stranded dna. *Macromolecules*, 30(19):5763–5765.

Tong, S. Y. C., Davis, J. S., Eichenberger, E., Holland, T. L., and Fowler, V. G. (2015). Staphylococcus aureus infections: Epidemiology, pathophysiology, clinical manifestations, and management. *Clinical Microbiology Reviews*, 28(3):603–661.

Treutlein, B., Lee, Q. Y., Camp, J. G., Mall, M., Koh, W., Shariati, S. A. M., Sim, S., Neff, N. F., Skotheim, J. M., Wernig, M., and Quake, S. R. (2016). Dissecting direct reprogramming from fibroblast to neuron using single-cell rna-seq. *Nature*, 534(7607):391–395.

Trueb, J. T., Avci, O., Sevenler, D., Connor, J. H., and Ünlü, M. S. (2017). Robust visualization and discrimination of nanoparticles by interferometric imaging. *IEEE Journal of Selected Topics in Quantum Electronics*, 23(2):1–10.

Turner, N. C. and Reis-Filho, J. S. (2012). Genetic heterogeneity and cancer drug resistance. *The Lancet Oncology*, 13(4):e178–e185.

Untergasser, A., Nijveen, H., Rao, X., Bisseling, T., Geurts, R., and Leunissen, J. A. M. (2007). Primer3plus, an enhanced web interface to primer3. *Nucleic Acids Research*, 35(suppl_2):W71–W74.

Vainrub, A. and Montgomery Pettitt, B. (2003). Surface electrostatic effects in oligonucleotide microarrays: Control and optimization of binding thermodynamics. *Biopolymers*, 68(2):265–270.

van der Pol, E., Böing, A. N., Harrison, P., Sturk, A., and Nieuwland, R. (2012). Classification, functions, and clinical relevance of extracellular vesicles. *Pharmacological Reviews*, 64(3):676–705.

van der Pol, E., Coumans, F., Varga, Z., Krumrey, M., and Nieuwland, R. (2013). Innovation in detection of microparticles and exosomes. *Journal of Thrombosis and Haemostasis*, 11:36–45.

Van Der Pol, E., Van Gemert, M. J. C., Sturk, A., Nieuwland, R., and Van Leeuwen, T. G. (2012). Single vs. swarm detection of microparticles and exosomes by flow cytometry. *Journal of Thrombosis and Haemostasis*, 10(5):919–930.

van Dijk, M. A., Lippitz, M., and Orrit, M. (2005). Far-field optical microscopy of single metal nanoparticles. *Accounts of Chemical Research*, 38(7):594–601.

van Dijk, M. A., Lippitz, M., Stolwijk, D., and Orrit, M. (2007). A common-path interferometer for time-resolved and shot-noise-limited detection of single nanoparticles. *Optics Express*, 15(5):2273–2287.

Vogelstein, B. and Kinzler, K. W. (1999). Digital pcr. *Proceedings of the National Academy of Sciences*, 96(16):9236–9241.

Vollmer, F. and Arnold, S. (2008). Whispering-gallery-mode biosensing: label-free detection down to single molecules. *Nature Methods*, 5(7):591–596.

Wang, S., Shan, X., Patel, U., Huang, X., Lu, J., Li, J., and Tao, N. (2010). Label-free imaging, detection, and mass measurement of single viruses by surface plasmon resonance. *Proceedings of the National Academy of Sciences*, 107(37):16028–16032.

Wang, Z., Gerstein, M., and Snyder, M. (2009). Rna-seq: a revolutionary tool for transcriptomics. *Nature Reviews Genetics*, 10(1):57–63.

Waxenegger, J., Trügler, A., and Hohenester, U. (2015). Plasmonics simulations with the mnpbem toolbox: Consideration of substrates and layer structures. *Computer Physics Communications*, 193:138–150.

Wei Hou, H., P. Bhattacharyya, R., T. Hung, D., and Han, J. (2015). Direct detection and drug-resistance profiling of bacteremias using inertial microfluidics. *Lab on a Chip*, 15(10):2297–2307.

Wittwer, C. T., Reed, G. H., Gundry, C. N., Vandersteen, J. G., and Pryor, R. J. (2003). High-resolution genotyping by amplicon melting analysis using lcgreen. *Clinical Chemistry*, 49(6):853–860.

Wong, I. Y. and Melosh, N. A. (2010). An electrostatic model for dna surface hybridization. *Biophysical Journal*, 98(12):2954–2963.

Xu, J. and Craig, S. L. (2005). Thermodynamics of dna hybridization on gold nanoparticles. *Journal of the American Chemical Society*, 127(38):13227–13231.

Yakovchuk, P., Protozanova, E., and Frank-Kamenetskii, M. D. (2006). Base-stacking and base-pairing contributions into thermal stability of the dna double helix. *Nucleic Acids Research*, 34(2):564–574.

Yu, T., Stockmann, C., Balch, A. H., Spigarelli, M. G., and Sherwin, C. M. T. (2014). Evolution of interventional vancomycin trials in light of new antibiotic development in the usa, 1999-2012. *International Journal of Antimicrobial Agents*, 43(3):215–222.

6.5 Curriculum Vitae